UNIVERSITY OF CALIFORNIA,
IRVINE

Omnidirectional Optical Communicator for Cube-Satellite Crosslink: Design and Analysis

DISSERTATION

submitted in partial satisfaction of the requirements
for the degree of

DOCTOR OF PHILOSOPHY

in Electrical Engineering

by

Imam Uz Zaman

Dissertation Committee:
Professor Ozdal Boyraz, Chair
Professor Nader Bagherzadeh
Professor Ahmed Eltawil

2021

DEDICATION

To

my parents and siblings

for their endless love, support, prayer, and encouragement.

TABLE OF CONTENTS

LIST OF FIGURES

LIST OF TABLES

LIST OF ABBREVIATIONS

AOA	Angle of Arrival
AOI	Angle of Incidence
APD	Avalanche Photo Diode
AR	Anti-Reflection
BER	Bit Error Rate
BPSK	Binary Phase Shift Keying
ECBR	Effective Communication Beam Region
ECBW	Effective Communication Beam Width
FOR	Field of Regard
FOV	Field of View
HFP	Hexagonal Filling Pattern
ISOL	Inter Satellite Optical Link
LEO	Low Earth Orbit
MEMS	Micro-Electro-Mechanical Device
NEP	Noise Equivalent Power
OOK	On-Off Keying
OOT	Omnidirectional Optical Transceiver
PAA	Phased Array Antenna
PAT	Pointing, Acquisition, and Tracking
PD	Photo Detector
RMS	Root Mean Square
RX or Rx	Receiver
SFP	Square Filling Pattern
SM	Scanning Mirror
SNR	Signal to Noise Ratio
SSA	Smallest Step Angle

SWaP-C	Size, Weight, Power, and Cost
TIA	Transimpedance Amplifier
TX or Tx	Transmitter
VCSEL	Vertical-Cavity Surface-Emitting Laser
WSOT	Wavelength Selective Optical Transceiver

ACKNOWLEDGEMENTS

It is a genuine pleasure to express my deep sense of thanks and gratefulness to my supervisor, Professor Ozdal Boyraz. His expertise, guidance, feedback, and support made it possible to complete my research and dissertation. Without Professor Boyraz's guidance and persistent help, this dissertation would not have been possible. Furthermore, I would like to thank my dissertation committee members, Professor Nader Bagherzadeh and Professor Ahmed Eltawil for their invaluable opinion and suggestions for my research. I am extremely thankful to Dr. Jose Velazco, supervisor, Jet Propulsion Laboratory (JPL) for providing me necessary technical suggestions during my research pursuit.

My sincere thanks also go to my colleagues, Rasul Torun, Md Shafiqul Islam, Mustafa Mert Bayer, Parinaz Sadri-Moshkenani, Mohammad Wahiduzzaman Khan, and Qiancheng Zhao who helped me in many ways through my research and personal growth.

I am highly indebted and thoroughly grateful to my father, mother, brother, and sister for their endless support, unconditional love, and incessant encouragement throughout the research period. Also, I am thankful to all my relatives and friends for believing in me. I am grateful to the Optical Society of America (OSA) and IEEE for publishing my works in their conferences and journals. Lastly, I offer my regards to all of those who supported me indirectly in any respect during the completion of this dissertation.

VITA

Imam Uz Zaman

EDUCATION

Doctor of Philosophy in Electrical Engineering	February 2021
University of California, Irvine	Irvine, CA, USA
Master of Science in Electrical Engineering	December 2018
University of California, Irvine	Irvine, CA, USA
Bachelor of Science in Electrical and Electronic Engineering	June 2014
Bangladesh University of Engineering and Technology	Dhaka, Bangladesh

TEACHING EXPERIENCE

Teaching Assistant		Fall 2016, 17,18,19,20
University of California, Irvine	EECS 70 A, EECS 170 A	Irvine, CA

RESEARCH BACKGROUND

Design and optimization of analog optical link, free space miniature optical system development, CubeSat communication system, and laser remote sensing.

PUBLICATIONS

Journals

1. **I. U. Zaman**, J. E. Velazco, and O. Boyraz, "Omnidirectional Optical Crosslinks for CubeSats: Transmitter Optimization," *IEEE Transactions on Aerospace and Electronic Systems*, pp. 1–1, 2020, doi: 10.1109/TAES.2020.2995320.
2. **I. U. Zaman**, J. E. Velazco, and O. Boyraz, "Realization of Omnidirectional CubeSat Crosslink by Wavelength Selective Optical Transceiver," *IEEE Journal on Miniaturization for Air and Space Systems*, pp. 1–1, 2020, doi: 10.1109/JMASS.2020.2995316.
3. **I. U. Zaman** and Ozdal Boyraz, "Impact of receiver architecture on small satellite optical link in the presence of pointing jitter," Appl. Opt. 59, 10177-10184 (2020)
4. **I. U. Zaman**, A. B. Lopez, M. A. A. Faruque, and O. Boyraz, "Physical Layer Cryptographic Key Generation by Exploiting PMD of an Optical Fiber Link," *Journal of Lightwave Technology*, vol. 36, no. 24, pp. 5903–5911, Dec. 2018, doi: 10.1109/JLT.2018.2880957.
5. R. Torun, M. M. Bayer, **I. U. Zaman**, J. E. Velazco, and O. Boyraz, "Realization of Multitone Continuous Wave Lidar," *IEEE Photonics Journal*, vol. 11, no. 4, pp. 1–10, Aug. 2019, doi: 10.1109/JPHOT.2019.2922690.
6. **I. U. Zaman**, Ahmed Eltawil, and Ozdal Boyraz, "Wireless Communication Technologies in Omnidirectional CubeSat Crosslink: Feasibility Study and Performance Analysis", IEEE Journal on

Miniaturization for Air and Space Systems. (Under revision, submitted in Jan 2021)

Conferences

1. **I. U. Zaman**, A. W. Janzen, R. Torun, J. E. Velazco, O. Boyraz, and Ozdal Boyraz, "Design Tradeoffs and Challenges of Omnidirectional Optical Antenna for High Speed, Long Range Inter CubeSat Data Communication," SSC18-WKII-06, Aug. 2018.
2. **I. U. Zaman**, A. W. Janzen, R. Torun, M. Peng, J. E. Velazco, and O. Boyraz, "Omnidirectional optical transceiver design techniques for multi-frequency full duplex CubeSat data communication," 10769-42, Aug. 2018.
3. **I. U. Zaman**, Sergey Shaboyan, Alireza S. Behbahani, Ahmed M. Eltawil, and Ozdal Boyraz, "A Comparative Study of Inter CubeSat High-Speed Links: RF, mmWave, and Optical," in *Laser Communications for Small Satellites*, Oregon, Oct. 2019, p. S13.1.
4. **I. U. Zaman**, Jose E. Velazco, and Ozdal Boyraz, "Wavelength Selective Optical System for CubeSat Crosslink," in *Laser Communications for Small Satellites*, Oregon, Oct. 2019, p. S4.4.
5. **I. U. Zaman**, A. B. Lopez, M. A. A. Faruque, and O. Boyraz, "Polarization Mode Dispersion-Based Physical Layer Key Generation for Optical Fiber Link Security," in *Advanced Photonics 2017 (IPR, NOMA, Sensors, Networks, SPPCom, PS) (2017), paper JTu4A.20*, Jul. 2017, p. JTu4A.20, doi: 10.1364/IPRSN.2017.JTu4A.20.
6. **I. U. Zaman**, A. B. Lopez, M. A. A. Faruque, and O. Boyraz, "A Physical Layer Security Key Generation Technique for Inter-Vehicular Visible Light Communication," in *Advanced Photonics 2017 (IPR, NOMA, Sensors, Networks, SPPCom, PS) (2017), paper SpTu1F.3*, Jul. 2017, p. SpTu1F.3, doi: 10.1364/SPPCOM.2017.SpTu1F.3.
7. M. M. Bayer, R. Torun, **I. U. Zaman**, and O. Boyraz, "A Basic Approach for Speed Profiling of Alternating Targets with Photonic Doppler Velocimetry," in *Conference on Lasers and Electro-Optics (2019), paper AW4K.4*, May 2019, p. AW4K.4, doi: 10.1364/CLEO_AT.2019.AW4K.4.
8. J. E. Velazco *et al.*, "High Data Rate Inter-Satellite Omnidirectional Optical Communicator," in *32nd Annual AIAA/USU Conference on Small Satellites*, 2018, pp. SSC18-WKI-02.
9. J. E. Velazco *et al.*, "Inter-satellite omnidirectional optical communicator for remote sensing," in *CubeSats and NanoSats for Remote Sensing II*, 2018, vol. 10769, pp. 157 – 162, doi: 10.1117/12.2322367.
10. O. Boyraz, M. M. Bayer, R. Torun, and **I.-U. Zaman**, "TuD2.2 - Multi Tone Continuous Wave Lidar (Invited)," in *2019 IEEE Photonics Society Summer Topical Meeting Series (SUM)*, Jul. 2019, pp. 1–2, doi: 10.1109/PHOSST.2019.8794998.

Google scholar link: https://scholar.google.com/citations?user=1vpWyAwAAAAJ&hl=en

LinkedIn link: https://www.linkedin.com/in/imamuzzaman/

ABSTRACT OF THE DISSERTATION

Omnidirectional Optical Communicator for Cube-Satellite Crosslink: Design and Analysis

by

Imam Uz Zaman
Doctor of Philosophy in Electrical Engineering
University of California, Irvine, 2021
Professor Ozdal Boyraz, Chair

Advanced space missions embrace constellation or swarm-like CubeSats, small reconfigurable satellite platforms, to achieve unprecedented spatial and temporal resolutions at a significantly lower investment. The realization of a high-speed inter-satellite optical communication link is essential to ensure the success of such CubeSat missions. CubeSats are a class of research spacecraft called nanosatellites. CubeSats are built to standard dimensions (Units or "U") of 10 cm x 10 cm x 10 cm. Size, Weight, and Power-Cost (SWaP-C) have never become so crucial as it is in a typical CubeSat platform. The desired performance metrics are extremely challenging to achieve with the available resources defined by the satellite platform. Therefore, special design and optimization rules are indispensable to design a simple optical transceiver with full-duplex capability, fast-tracking speed, and a full field of regard. In this dissertation, I address the challenges pertinent to inter-satellite communication systems and present a potential omnidirectional communication method. In particular, I present transceiver design optimizations for omnidirectional optical communication, collaborative communication strategies between RF and optical for maximum reach, and CubeSat crosslink implementation based on the wavelength-selective-optical-transceiver design. I demonstrate the relations and dependencies among key transceiver design parameters such as scanning mirror's smallest step angle, laser beam divergence, optics dimensions, and scanning area filling efficiency, etc. Additionally, the optimization challenges of the transmit laser beam size considering the interplay among beam divergence, beam clipping, and scattering are studied in detail.

Besides, this dissertation presents the optical and mechanical design of the transceiver units that can fit inside a state-of-the-art CubeSat to achieve an omnidirectional high-speed (more than 400 Mb/s) optical crosslink. Furthermore, a mathematical model is derived to investigate the link performance in the presence of angular pointing jitters for different receiver architectures. Alongside the statistical pointing error model, the derived model incorporates major receiver design parameters such as detector radius, receiver aperture size, F-number of the lens system, beam compression ratio, etc. It is shown that an optimum receiver design based on the presented model can achieve more than five orders of magnitude Bit Error Rate improvement even at large pointing errors.

Chapter 1

Introduction

Over the years, CubeSats have evolved from a purely educational tool to a prevailing platform for technology demonstration and scientific instrumentation [1]–[3]. A CubeSat is a type of nanosatellite that is constructed in modules of multiples units (U), $1U \approx 10\ cm \times 10\ cm \times 10\ cm$. Due to the platform limitation, Size, Weight, and Power-Cost (SWaP-C) have never become so crucial as it is in the typical CubeSat platforms (smaller than 12U) where the performance metrics clash with the available volume (less than 0.02 m^3), weight (less than 36 lb.) and average power availability (below 150 W). Therefore, advanced CubeSat missions are expected to be designed in such a way that each one of the CubeSats in a constellation is assigned to a specific time-synchronous role, and collaboratively, they are assigned to accomplish a complex task [1], [4], [5]. Each satellite of the constellation is required to gather the expected information, share it with its peers, process partially, relay the information, and may downlink the result to a base station. An engineered 3D constellation of these satellites can play a vital role in achieving small, affordable, and transformative approaches to enable complex missions such as wind measurement, weather prediction, topography, etc. without sacrificing performance metrics that are achieved in conventional space technologies. One of the major required features of this constellation in space is the high-speed data communication with a 360^o Field of Regard (FOR). The full FOR facilitates simultaneous point-to-point data communications as well as data relaying among an arbitrary set of satellites. Depending on the type of application, the required data rates can go up to gigabits per second, while power consumption and physical size are limited by the platform. Therefore, the design of an omnidirectional communication network for the CubeSat platform requires special design and optimization rules.

An Omnidirectional Optical Antenna (OOA) is a promising choice to establish a multi-gigabit data transmission link among small satellites. An OOA is capable of establishing full-duplex, high-speed data communication to other optical antennas in any direction. The omnidirectional optical system in an extremely resource-limited CubeSat platform is a new and demanding concept that possesses its unique design and optimization challenges. The major design challenges include but not limited

to, a) high-speed 360° FOR scanning telescope design, b) telescope design with low beam divergence and high beam quality, c) wide Field of View (FOV) receiver design, d) telescope design considering scanning mirror's speed-size tradeoffs, e) crosstalk minimization caused by optical back reflections, f) tolerance to pointing jitter, g) low available total power, and h) light-weight, etc. To establish high-speed optical connectivity among different CubeSats in the constellation, the optical communicator must possess full FOR, high scanning rate, fast Angle of Arrival (AOA) detection system as well as the capability to maintain multiple communication links simultaneously. State-of-the-art optical communication links are usually focused on point-to-point links and the systems are designed for larger satellites. The majority of the designs use larger optics, consume very high power (in the order of hundreds of Watts) that does not satisfy CubeSat resource limits. Besides, the conventional optical links do not possess high speed (greater than or equal to 500 Mb/s) crosslink data transmission and data relaying capabilities. Hence, the CubeSat scale optical crosslink design requires unprecedented optical design techniques, optimization methodology, and implementation strategy. This dissertation presents a detailed analysis of design rules, techniques, and theories to effectively implement a high-speed omnidirectional optical crosslink for CubeSat swarms.

In this dissertation, an optical communicator design methodology is presented that is based on a CubeSat scale Wavelength Selective Optical Transceiver (WSOT) system architecture. WSOT system can achieve a 360^{o} Field of Regard (FOR), longer than 100 km of communication distance, and more than 400 Mb/s data rates. The analyses include the optical telescope design method, design optimization techniques, and experimental validation using FlatSat models. Besides, the achievable communication range and power consumption are also studied. In particular, this dissertation focuses on the system level optics integration and design rules to achieve omnidirectional communication in the CubeSat platform. An in-depth study of the optical design methodologies, housing techniques, component optimizations to address the optical system design challenges is presented.

Moreover, in this dissertation, the performance tradeoffs among potential wireless technologies and major Commercial-of-The-Shelf (COTS) components (e.g. scanning mirrors, collimators, phased array antenna, etc.) are investigated. The study of the power consumption, pointing requirement, and antenna requirement of each technology to implement an omnidirectional communicator is presented. The performance limit of the state-of-the-art wireless technologies considering the realizable link parameters is also investigated. The achievable data rate and communication distance are studied thoroughly for different communication systems. The analyses show that an optical communication link is capable of delivering more than two orders of magnitude higher data throughput than that of microwave links in an omnidirectional platform. However, the study shows that due to the size and power restriction, a performance crossover region exists where the performance of a microwave channel exceeds the performance of the optical channel. The crossover distance and crossover data rate are studied thoroughly with different system configurations and modulation formats to assess the maximum reach of wireless technologies in a CubeSat crosslink. Furthermore, by considering the deleterious effects such as beam divergence, satellite vibration, etc., I investigate the optimization rules for design parameters (aperture size, beam width, laser power, and scanning mirror specifications) to achieve a blind-spot free communication with maximum reach and maximum data rate. This dissertation also presents the concept of Effective Communication Beam Region (ECBR) and Effective Communication Beam Width (ECBW) to address pointing accuracy challenges due to host CubeSat vibrations and receiver position uncertainties. Analytical studies related to the scanning mirror-based beam steering system as well as the scanning mirror's smallest step angle requirement are also presented. Also, the relations and dependencies among scanning mirror's smallest step angle, laser beam divergence, optics dimensions, communication distance, and scanning area filling efficiency, etc. are demonstrated in detail.

Finally, in this dissertation, I present a mathematical model to investigate the link performance in the presence of angular pointing jitters for different receiver architectures. Alongside the statistical

pointing error model, the derived model incorporates key receiver design parameters such as detector radius, receiver aperture size, F-number of the lens system, beam compression ratio, etc. to demonstrate the impact of receiver architecture on the pointing jitter. The study shows that by careful selection of beam compression ratio and F-number, more than five orders of magnitude Bit Error Rate (BER) improvement is achievable even at large pointing error.

1.1 Background

Modern wireless inter-satellite communications are mostly based on microwave (Radio-frequency) technologies. Recent progress in the microwave-based CubeSat communication systems demonstrates a high data rate (up to 1.6 Gb/s) point to point communication with complex subcarrier modulation and high power consumption [6]–[9]. The versatile deployment of microwave technologies for simultaneous communication between multiple satellites in the CubeSat platform is limited by the bandwidth restriction, the available power, and the required antenna gain. Optical communication technologies have excellent directivity, and therefore, it has the potential to provide one to two orders of magnitude improvement in data transmission capacity over the microwave counterpart. Additionally, considering comparative data capacity to that of microwave technologies, optical communication systems usually consume less power and the transceivers can be fabricated in a significantly smaller form factor [10]–[12]. Nevertheless, the implementation of a PAT (Pointing, Acquisition, and Tracking) system in an optical communication system is a challenging task [13]–[15]. With the advancement of the high-resolution and fast-speed scanning mirrors and position sensors, the required pointing accuracy can be attained by the available technologies. The currently accessible cutting-edge sensors demonstrate an angular resolution better than 1 μ*rad.* [16]–[18].

Besides, the state-of-the-art ISOL usually operates in the presence of random angular pointing error (also known as pointing jitter). This pointing error arises primarily from the noise associated with the tracking sensors, the disturbance originated from the mechanical vibration, and the base

motion of the satellites [19]–[22]. As a result, ISOL suffers from performance degradation. Up to date, several analytical models have been presented to understand the impact of pointing jitter on the performance of the digital and analog optical links [23], [24]. Also, the authors studied the impact of random pointing and tracking error on coherent and incoherent optical satellite link in [15]. Several other works also investigated the performance degradation of the optical link due to the pointing jitters [19], [22], [25]. The main focus of the majority of these works was given towards the modeling of the nature of pointing jitters and therefore to estimate the overall link performance in terms of Bit Error Rate (BER) or Bit Error Probability (BEP). However, the effect of the receiver architecture on the communication performance in the presence of pointing jitter is yet to be studied. Since the receiver architecture plays a critical role in the ISOL's immunity to the random pointing error, it is desirable to have an analytical study that facilitates a quick estimation of the link performance by using realistic receiver architecture parameters.

Up to date, several optical communication methods have been explored for mini and microsatellites [26]–[29]. Among many of these methods, most of the efforts have been given on the long-range Low Earth Orbit (LEO) to Earth point-to-point data communications which usually utilize large ground telescopes (in the order of meters in dimension) as the receiver terminal. For instance, LEO to Earth optical communication with a data rate as high as 1 Gb/s is demonstrated in small satellite platforms (up to 6 kg payload incorporated in a 130 kg satellite that produces up to 1 W optical transmit power with about 37 W electrical power consumption [27], [28]). In [30] authors analyzed the feasibility of a coherent system that can fit in a small satellite platform to address the power and size constraints imposed by a small satellite platform. The analysis shows that up to 100 Mb/s point to point laser communication with a 20 cm aperture and 30 mW laser source. The optical communication between CubeSats with more stringent SWaP-C limits is a relatively new area of research and development. LED array-based LEO to Earth communication at 5 kHz with 200 W peak optical power is achieved in an experimental CubeSat (FITSAT-1) as one of the earliest developments

in this field [31]. Similarly, LEO to Earth communication with 100 Mb/s data rate and up to 20 W electrical power consumption has been demonstrated [32], [33]. A current NASA mission (CubeSat crosslink mission, "CLICK") sets a goal to achieve a 20 Mb/s at ranges from 25 km to 580 km by incorporating a 500 mW laser [34]. To the best of the authors' knowledge, all the research and development work on the satellite optical links (LEO-LEO, LEO-Earth) have been done either for satellites with significantly less SWaP-C constraints or for a single point to point (one to one) data communication link. Moreover, these satellites do not possess high speed (greater than or equal to 500 Mb/s) crosslink data transmission and data relaying capabilities. However, the constellation and formation fly of such satellites necessitates optical communicator with omnidirectionality and data relaying capabilities to minimize data storage and on-board electronic processing. Omnidirectional (one to many) high-speed data communication and data relaying capability among small satellites are still open for investigation in optical domain.

1.2 Dissertation Organization

This dissertation is organized into four chapters. In Chapter 2, a detailed performance comparison of the available wireless technologies is presented to access the feasibility of achieving omnidirectional data communication in a CubeSat platform. The crossover distance and crossover data rates are studied thoroughly with different system configurations and modulation formats to assess the maximum reach are also presented in this chapter. Chapter 3 presents the design and experimental validation of the wavelength-selective-optical-transceiver (WSOT) based omnidirectional CubeSat communication system. The discussion on how to scale the system performance in terms of power and maximum reach is also demonstrated in this chapter. In Chapter 4, the detailed optical transmitter design challenges and optimization rules to achieve a full field of regard optical antenna is demonstrated. The unprecedented size, weight, power, and cost constraints imposed by the CubeSat platform and the availability of the commercial-off-the-shelf components are

considered in the analyses. In Chapter 5, I present a mathematical model to investigate the link performance in the presence of angular pointing jitters for different receiver architectures. The analyses carried out here can be the basis for optimum optical receiver design to achieve the best inter-satellite optical link performance in the presence of pointing errors.

Chapter 2

Wireless Technologies for Small Satellite Crosslink Data Communication

The realization of omnidirectional inter-satellite links is important to ensure the success of missions using constellation of multiple satellites as shown in Figure 2.1. The successful implementation of omnidirectional communication necessitates a detailed analysis of the strengths and weaknesses of the wireless technologies considering the distinct physical and technological constraints imposed by CubeSat technology and dynamic nature of desired multi-satellite constellations. Recent progress in the Radio Frequency (RF) and millimeter-wave (mmWave) demonstrate a high data rate (up to 1.6 Gb/s) point-to-point communication with complex subcarrier modulations and high-power consumption [1], [2].

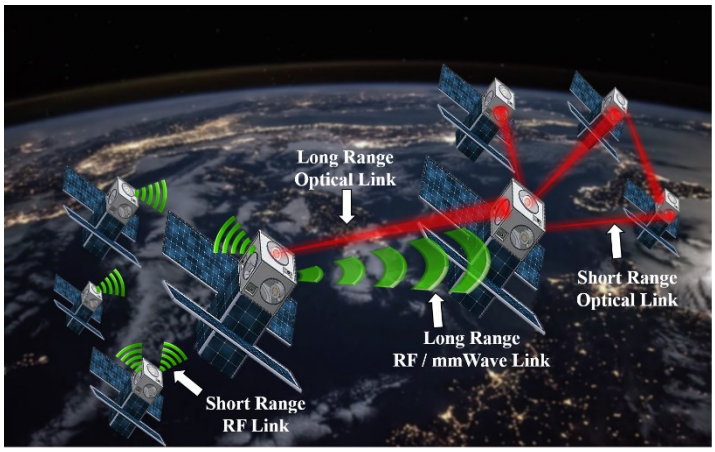

Figure 2.1. Wireless communication systems for CubeSat crosslink.

In this chapter, I present an in-depth feasibility study and performance crossover analysis of the available wireless technologies in the omnidirectional CubeSat platform. In particular, I study the performance of RF (2.4 GHz, 5 GHz, 26 GHz), mmWave (34 GHz, 60 GHz), and optical communication (from 180 THz to 400 THz) medium with self-imposed boundary conditions to satisfy the CubeSat SWaP-C constraints. I investigate the realizable data rate in different simple modulation formats with realistic physical constraints. It is shown that even though the optical communication shows significantly better performance up to a certain distance, there is a performance crossover region between microwave (RF and mmWave) and optical communication links. The crossover distance and

crossover data rate of different system combinations and modulation formats are also calculated to analyze the maximum reach and the maximum data rate of the communication systems. Furthermore, a feasibility study of wireless technologies in achieving omnidirectionality in terms of power consumption and antenna requirements is presented in this chapter.

2.1 Comparative Study of the Link Budget Parameters

The comparative performance study of wireless communication begins with the well-known link budget equation that estimates the received power P_{rcv} based on the transmitted power P_T, total antenna gain G, total loss Γ, and combined antenna efficiencies η in a simple formula that is expressed as [35]

$$P_{rcv} = P_T G \Gamma \eta \tag{2.1}$$

Total antenna gain G here is the combined gain of the transmitter antenna gain $G_T = f(D_T, \lambda)$ and receiver antenna gain $G_R = f(D_R, \lambda)$ i.e. $G = G_T G_R$, where D_T, D_R, and λ represent transmitter diameter, receiver diameter, and operating wavelength. Total loss Γ includes transmitter feeder loss L_T , receiver plumbing loss L_R, the path loss L, the pointing loss $L_P = f(G_T)$ and therefore, Γ can be expressed as $\Gamma = L_T L_R L L_P$. Assuming that we have transmitter and receiver antenna efficiencies of η_T and η_R, respectively, we define the combined antenna efficiency as $\eta = \eta_T \eta_R$. Almost all of these parameters depend on the size, available electrical power, and wavelength. Hence, constraints imposed by CubeSat dimensions differs significantly from the constraints imposed by relatively large satellite resources even though the performance expectations are quite similar. Hence, several boundary conditions pertinent to the CubeSats platform are imposed in this study. Some of these self-imposed conditions are, a) CubeSats are smaller than 12U (1U ≈ 10 cm × 10 cm × 10 cm), b) total power consumption of the communication payload is less than 50 W (12U limit), c) microwave antenna size (dish size) is less than 200 mm, d) maximum optics diameter is 50 mm, e) transmit power, P_T = 1 W, and f) only non-deployable antennas to accommodate multiple antennas to achieve

omnidirectionality.

The transmit antenna gain G_T represents the power transmitted by an antenna in a specific direction as compared to an isotropic antenna and can be estimated from the full-divergence angle (θ) [in rad] of the transmit beam [36], [37], $G_T \approx \frac{16}{\theta^2}$. Since $\theta = f(\lambda, D_T)$, the G_T can also be estimated as $G_T \approx \left(\frac{\pi D_T}{\lambda}\right)^2$. The receiver antenna gain G_R is defined as the ratio of the received power to the power received by an isotropic antenna and can be estimated as $G_R \approx \left(\frac{\pi D_R}{\lambda}\right)^2$. It can be realized that both G_T and G_R are proportional to the square of the diameter to the wavelength ratio (D_K/λ) where $k \in \{T, R\}$. Here, T, R represent the transmitter and the receiver, respectively. In other words, the larger the antenna diameter the higher the gain is, and in contrast, a smaller wavelength (or a higher carrier frequency) realizes a higher gain for a given antenna size. Consequently, optical frequencies possess much higher antenna gain compared to that of RF and mmWave systems for a given antenna size. The realizable antenna gains for different aperture sizes and frequency are shown in Figure 2.2.

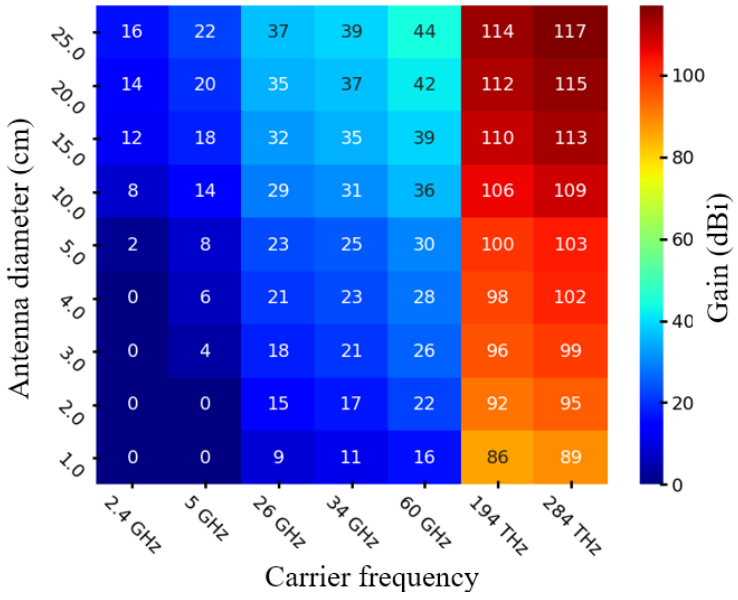

Figure 2.2. Achievable antenna gains for different carrier frequencies and antenna diameters.

Indeed, the upper limit of the antenna size is limited by the CubeSats platform such as available

volume, size, weight, etc. The RF and mmWave communication systems usually use the same physical antenna to send and receive the signals, therefore one can assume $G_T = G_R$. On the contrary, most of the optical transceivers incorporate transmitters with smaller optics (D_T) and the receiver with comparably larger optics (D_R). Therefore, the antenna gains (G_T and G_R) can be very different in optical communication. The achievable G_T and G_R for different antenna sizes and carrier frequencies are presented in Figure 2.2.

It can be seen from Figure 2.2 that microwave systems can achieve a maximum total gain ($G_T + G_R$) of about 84 dBi with 25 cm antenna diameters. In contrast, more than 100 dBi antenna gain is readily achievable in optical frequencies by using optics that are more than 5 times smaller in dimension than that of microwave antennas. For instance, a combined antenna gain ($G_T + G_R$) of about 182 dBi is realizable with a 10 mm transmitter beam and a 30 mm receiver aperture at 194 THz (1550 nm) optical communication system. An optical antenna can achieve a higher antenna gain due to very high antenna directivity (small beam divergence angle θ). The diffraction-limited full-divergence angle θ [in degrees] can be estimated as, $\theta \approx 1.26 \left(\frac{180\lambda}{\pi D_T}\right)$. The required antenna diameters (normalized to 1 μm) to achieve different divergence angle are shown in Figure 2.3. For instance, it can be seen that 60 m, 5.55 m, 2.4 m, and 0.74 mm antennas are required for 2.4 GHz, 26 GHz, 60 GHz, and 194 THz carrier frequencies, respectively to achieve a beam divergence of about 0.15^o. It is evident that a small divergence angle (less than 1^o) is not feasible in RF and mmWave communication systems due to the need for a very large antenna diameter that exceeds commonly used CubeSats (1U to 12U) dimensions. However, optical antennas can achieve a very small divergence angle (less than 0.01^o) with less than 1 mm antenna aperture (optical telescope). Although high directivity is desired for efficient power delivery to the Rx antenna, it comes with stringent pointing accuracy requirements. Therefore, a sophisticated pointing and acquisition system needs to be implemented in the optical communication system to maintain effective data communication. To achieve a throughput loss less than 3.0 dB, the required pointing accuracy ϵ (in

rad) of an inter-satellite communication link can be expressed as [37], $\epsilon \approx \frac{\lambda}{20D_T}$.

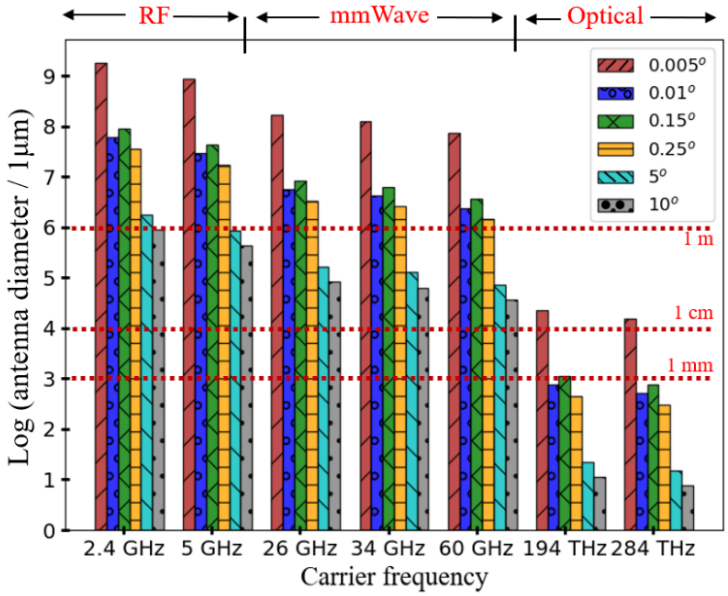

Figure 2.3. Required antenna diameters for different full divergence angle.

The required pointing accuracy for different antenna sizes and operating wavelengths are calculated and presented in Figure 2.4. It can be seen from Figure 2.4 that about 10 rad to 1 mrad pointing accuracy is needed for RF frequencies (up to 25 GHz) with the antenna diameter ranges from 1 cm to 50 cm. The mmWave link requires about 10 times higher pointing accuracy (0.1 rad to 0.1 mrad) compared to RF for the same antenna diameter range over the frequency range of 26 GHz to 300 GHz. Evidently, the optical regime has the most stringent pointing accuracy requirement of 10 μ*rad* to 0.1 μ*rad* for optical frequency greater than or equal to 180 THz. The path loss L between the feed points of two isotropic antennas in free space at a distance r can be given in term of the carrier frequency f and the speed of light c, $L = \left(\frac{c}{4\pi fr}\right)^2$. Due to higher carrier frequency, the optical communication experiences higher path loss (more than 50 dB) than that of RF and mmWave frequencies.

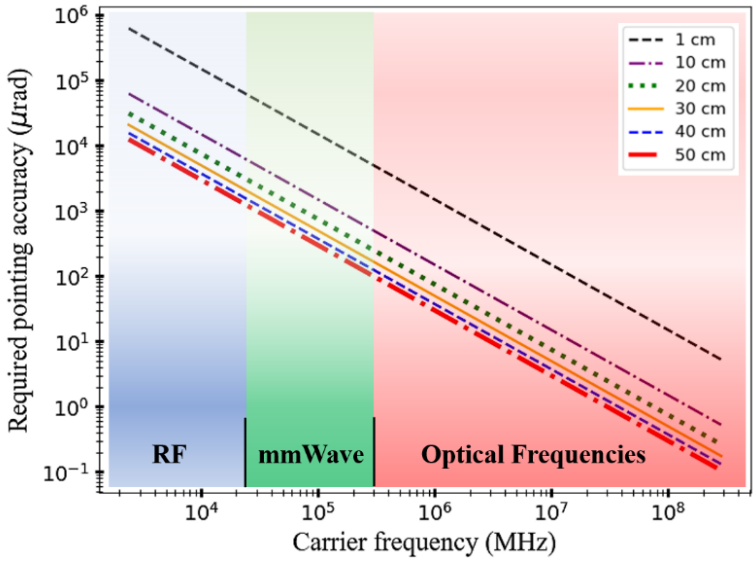

Figure 2.4. Required pointing accuracy for different wireless links.

There exist intertwined relationships among the above-mentioned link parameters. For example, a large transmit antenna gain G_T is achieved in mmWave and optical communication by transmitting a high directional beam (low θ). The high directional beam tends to cause a higher pointing loss L_P as the beam pointing and tracking between the transmitter and receiver becomes a challenging task [15], [38]. As described in the next section, the high directional beam also necessitates a larger number of transmitters to attain omnidirectionality (360^o FOR). Moreover, it is apparent from the path loss equation that optical communication experiences a higher loss compared to that of RF and mmWave due to higher f. However, the high L is mostly compensated by the very large antenna gain terms (G_T and G_R) in the link budget equation. The detailed communication link performance considering the interplay among all the link parameters is investigated in the later section of this chapter.

2.2 Transceiver Antenna Requirement for Omnidirectional Communication

To achieve omnidirectional communication, both the transmitter (TX) and the receiver (RX)

need to possess a full FOR (360^o). The required number of transceivers to achieve a FOR of α_{req} (in degrees) is given by,

$$n \approx ceiling\left(\left(\frac{\sin\left(\frac{\pi\alpha_{\mathrm{req}}}{720}\right)}{\sin\left(\frac{\pi\alpha}{720}\right)}\right)^2\right) \qquad (2.2)$$

Here, α is the FOR (in degrees) of the transceiver system. In the case of directional RF and mmWave antenna (patch antenna, dish antenna), α corresponds to the antenna beamwidth (or divergence angle). In a Phased Array Antenna (PAA) based system with a full scanning angle of α_{PAA}, $\alpha = \alpha_{PAA}$. In a scanning mirror-based optical communication system with a full mechanical scanning range of α_{mec}, $\alpha \approx 2\alpha_{mec}$. The required number of transceivers needed to achieve omnidirectional communication in a static (non-beam steering) RF and mmWave communication system is calculated and shown in Figure 2.5. It can be seen from Figure 2.5 that a 2.4 GHz RF system requires 7, 15, 27 antennas when the antenna diameters (size of the dish) are 100 mm, 150 mm, and 200 mm, respectively. The requirements of a large number of antennas is a direct consequence of transmitting a high directional beam to achieve a large antenna gain. Moreover, a higher operating frequency demands for larger n. Therefore, realizing a high-speed, long-distance communication in RF and mmWave is not feasible with dish antennas or patch antennas due to the trade-off among G_T , G_R, and n. The emerging PAA enables effective beam-switching and beam-scanning in RF and mmWave system and therefore, it possesses the potential to achieve a full FOR with a lesser number of transceiver units than the calculated n in Figure 2.5. Many PAA systems have been demonstrated in the past several years. For example, in [39], authors present a 28 GHz PAA system (8 × 6 elements, 56 mm × 42 mm) that can achieve a gain of 21 dBi with 10^o beam width and $\pm 110^o$ beam scanning. A metamaterial thin lens-based antenna (26 GHz to 30 GHz, greater than 55^o beam width, about 24.5% antenna efficiency) is presented in [40] that shows a 24.2 dBi antenna gain and $\pm 27^o$ scanning range. In [41], authors present a 28 GHz bulk-CMOS phased- array transceiver (4 × 6 elements) which

can attain 44/34 dBi antenna gain with $\pm 45^o$ beam scanning range. Furthermore, A 28 GHz 32-element phased-array transceiver IC that is capable of $\pm 50^o$ scanning with 1.4 degrees beam-steering resolution (greater than 10^o beam width) is presented in [42].

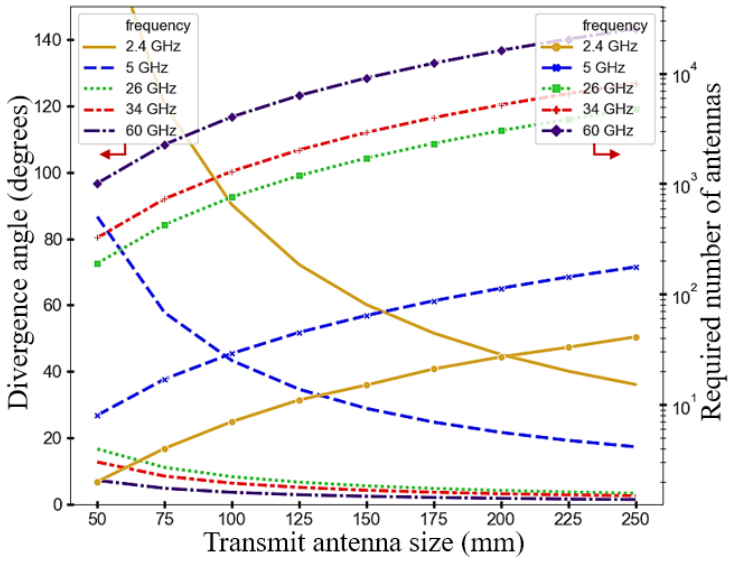

Figure 2.5. The required number of transceivers to achieve a full FOR.

The state-of-the-art RF and mmWave PAAs still create a large beam divergence (usually greater than 5^o) and therefore demonstrate low antenna gains compared to the optical antennas. Based on the PAA mentioned above, it can be calculated that 2, 19, 7, and 6 PAA antenna systems are required to achieve an omnidirectional communication for the antenna systems mentioned in [39], [40], [41], and [42], respectively. Since the state-of-the-art PAA systems are very power-hungry systems, the implementation of the required number of antennas is limited by the available power in the SWaP-C limited CubeSat platform. COTS high-speed (about 1 KHz) scanning mirror technologies are compact (diameter less than 15 mm) and they can achieve a wide optical scanning angle (as high as 100^o) [43]. Because of the advancement of the scanning mirror technologies, it is possible to to obtain a full FOR in a less than 6U CubeSat platform by incorporating 9 and 6 independent transceivers by incorporating scanning mirrors with full mechanical scanning ranges of 40^o and 50^o, respectively

[3], [44].

2.3 Sample Power Consumption Estimation of Wireless Transceivers

SWaP-C restrained CubeSat platform is extremely power limited. For example, state of the art solar panel such as eHawk can generate about 75 W and 140 W average electrical power in a 6U and 12U platforms, respectively [4], [45]. Assuming that only 40% of the total power is allocated for the communication payload, the available powers are about 30 W and 56 W in 6U and 12U CubeSats, respectively. Sample block diagrams of a microwave transceiver (RF and mmWave) and an optical transceiver are presented in Figure 2.6.

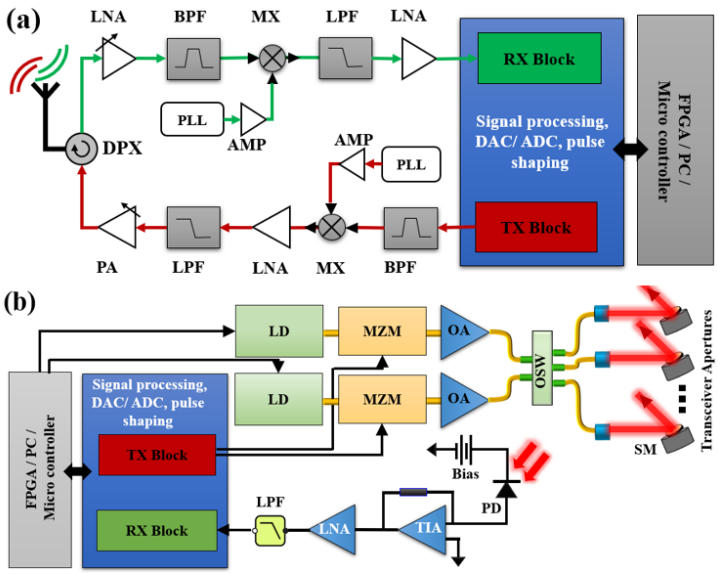

Figure 2.6. Sample block diagrams of the transceiver architectures (a) RF and mmWave, (b) optical.

The short description, the gain or loss, and the approximate power consumption of the major link components are summarized in Table 2.1. The power consumption of the Passive Components (PC) is set to zero. The Splicing and Pump Combiner (SPC) losses of the optical transceiver are lumped together in the table and not shown in Figure 2.6(b). The power consumption approximation of the sample microwave communication link (RF and mmWave) is based on the manufacturer's

specification of the COTS components. The calculated power consumption of a microwave TX to produce a 1 W output power is about 6 W (using Table 2.1). Similarly, the estimated RX power consumption is about 3.45 W. Hence, to establish a point-to-point link with a 1 W transmit power, the microwave communication system requires about 9.45 W electrical power.

Table 2.1 Parameters of the major transceiver components.

Item	Description	Gain/Loss (dB)	P(w)
LNA	Low noise amplifier	$\approx +25$	≈ 0.3
BPF	Band pass filter	≈ -0.2	0.0 (PC)
LPF	Low pass filter	≈ -1.8	0.0 (PC)
MX	Mixer	≈ -9.0	0.0 (PC)
PA	Power amplifier	$\approx +24.5$	≈ 2.4
PLL	Phase locked loop	N/A	≈ 0.1
AMP	Amplifier	$\approx +13$	≈ 0.25
DPX	Duplexer	≈ -1.5	≈ 0.0 (PC)
LD	Laser diode (100 mW)	N/A	≈ 0.5
MZM	Mach-Zehnder modulator	≈ -5.0	≈ 0.25
OSW	Optical switch	≈ -0.8	≈ 0.2
TIA	Transimpedance amplifier	$\approx +32.5$ $(K\Omega)$	≈ 0.3
OA	Optical amplifier	$\approx +15$	≈ 3.5
SM	Scanning mirror	≈ -0.15	≈ 0.5
SPC	Splicing and pump	≈ -0.1	≈ 0.0 (PC)
TX Block	Transmit signal processor	N/A	≈ 3.0
RX Block	Receive signal processor	N/A	≈ 2.5

The power consumption of the optical transceivers is dictated by the realizable efficiencies of the lasers and the optical amplifiers that can vary quite a bit from one system to another. To estimate the power consumption, a 1550 nm (194 THz) optical communication system is considered. Besides, the wall-plug efficiency of the Laser Diode (LD) and Optical Amplifier (OA) are assumed

approximately as 20% and 15%, respectively. At a 50% duty cycle about 500 mW average output optical power is required to generate a 1 W peak optical power. As shown in Figure 2.6(b), about 16 dB optical gain is needed from OA to achieve a 1 W peak power that incorporates a 100 mW LD. Therefore, considering the data provided in Table 2.1, the optical transmitter power consumption, $P_{TXOPT} \approx 8.0\,W$, and the receiver power consumption, $P_{RXOPT} \approx 3.0\,W$. Therefore, the sample optical transceiver consumes about 11.0 W electrical power.

The high-power consumption and the required number of transceivers n to achieve a 360^o FOR transceiver with non-beam steering RF and mmWave communication system is hardly feasible in the current CubeSat platform. Furthermore, incorporating multiple active PAA to facilitate the beam steering based omnidirectional communication is challenging in the existing CubeSat due to the high-power consumption of the PAA (e.g. greater than 500 W for a single 64 element system [46]). In contrast, the advancement in miniature high scanning speed mirror technologies (power consumption less than 0.5 W) such as micro-electro-mechanical systems (MEMS), dual-axis vector mirror-based optical transceiver can achieve a full FOR with a predefined number of transceivers and reasonable power consumption as described above. For instance, in the example design shown in Figure 2.6(b), it can be estimated that about 16.5 W electrical power is required to operate two simultaneous optical communication links (one point to point and one data relaying). The detailed design challenges and trade-offs of the omnidirectional optical transceivers are presented in Chapter 4, and Chapter 5.

2.4 Comparative Performance Analysis

The achievable data rate and the achievable communication distances of the wireless point to point communication system with different modulation formats and design parameters are studied in this section. The RF, mmWave, and optical links are quite different from each other when considering the realistic link parameters. In this analysis, the considered values for each parameter

are chosen based on a literature survey and manufacturer specifications that are typically used in the state-of-the-art systems [11], [44], [48], [49]. Considering the CubeSat SWaP-C constraints and the size of optics (volume, weight), I choose optical transmitter aperture, $D_{T(opt)} = 10\ mm$ and receiver aperture, $D_{R(opt)} = 50\ mm$. Since RF and mmWave antennas are relatively lightweight and compact, the considered antenna sizes $D_{k(rf,mmWave)} = \{100\ mm, 150\ mm, 200\ mm\}$. Here the subscript $k \in \{T, R\}$ where T, R represent the transmitter and the receiver, respectively. The link constants considered in our analyses are summarized in Table 2.2.

Table 2.2 Link budget parameters.

Item	Wireless technologies	Value
Transmit power (P_T)	RF, mmWave, Optical	1 W
Tx diameter (D_T)	RF, mmWave	5 to 20 cm
	optical	10 mm
RX diameter (D_R)	RF, mmWave	5 to 20 cm
	optical	50 mm
Pointing loss (L_P)	RF	- 0.3 dB
	mmWave	- 1.0 dB
	optical	-3.0 dB
Tx-Rx feeder loss	RF	-5.1 dB
	mmWave	-4.1 dB
	optical	-3.5 dB
Receiver sensitivity	RF, mmWave	-108 dBW
	optical	$\approx -90\ dBW$
Receiver noise figure	RF, mmWave	6 dB
Noise bandwidth (B)	RF, mmWave, optical	1 GHz
Photodiode gain	optical	100
Noise equivalent power	optical	$30\frac{pW}{\sqrt{Hz}}$
Link margin (M)	RF, mmWave, optical	- 3 dB

2.4.1 Achievable Data Rate in Different Modulation Formats

Assuming antenna efficiencies, $\eta_T = \eta_R = 1$, the link budget equation stated in Eq. (2.1) of section 2.1 can be simplified to approximate the received power P_{rcv} (in dB),

$$P_{rcv} = P_T + 20\log(R_T) + 20\log(R_R) - 20\log(r) - 20\log(\lambda) + 10\log\left(L_p L_R L_T\right) + 9.943 \qquad (2.3)$$

Digital communication systems require a certain ratio of energy per bit E_b to noise density N_o ($N_o = N/B$), E_b/N_o. Here, N is the total noise power and B is the communication bandwidth. The required received power P_{req} to realize a target data rate R_b can be expressed as $\frac{P_{req}}{N} \approx \frac{E_b}{N_o} \times \frac{R_b}{B} \times M$. Here, N is the total noise power, B is the bandwidth, E_b is the energy per bit, and No is the noise density ($N_o = \frac{N}{B}$). The R_b can be approximated as $Rb\,[dB] \approx \frac{P_{rcv}}{N} - \frac{E_b}{N_o} + B - M$. If the available received power is more than the required power i.e. $P_{rcv} > P_{req}$, the communication link is over-powered and may waste energy. The R_b in this case is limited by the bandwidth of the receiver system. On the other hand, if $P_{rcv} < P_{req}$, the communication link can not support error-free data communication at the target R_b. To establish an error-free data communication, the state-of-the-art Forward Error Correction (FEC) schemes such as RS(255,239), RS (255, 191) require pre-FEC Bit Error Ratio (BER) less than 4×10^{-3} to attain a post-FEC BER less than 5×10^{-15} [50], [51]. The relations to estimate the required BER in different modulation schemes such as Quadrature Phase Shift Keying (QPSK), Binary Phase Shift Keying (BPSK), Quadrature Amplitude Modulation (M-QAM), On-Off Keying (OOK), Pulse Position Modulation (L-PPM) and Pulse Amplitude Modulation (PAM-M) are summarized in Eq. (2.4) [52], [53].

$$
\begin{aligned}
BER_{QPSK,BPSK} &\approx \frac{1}{2} erfc\left(\sqrt{\frac{E_b}{N_o}}\right) \\
BER_{M-QAM} &\approx \frac{\sqrt{M}-1}{\sqrt{M}\log_2 M} erfc\left(\sqrt{\frac{3\log_2 M}{2(M-1)} \cdot \frac{E_b}{N_o}}\right) \\
BER_{OOK} &\approx \frac{1}{2} erc\left(\frac{1}{\sqrt{2}} \cdot \sqrt{\frac{E_b}{N_o}}\right) \\
BER_{L-PPM} &\approx \frac{1}{2} erfc\left(\frac{1}{4}\log_2 L \cdot \sqrt{\frac{E_b}{N_o}}\right) \\
BER_{PAM-M} &\approx \frac{1}{2} erc\left(\frac{1}{2\sqrt{2}} \frac{\log_2 M}{M-1} \cdot \sqrt{\frac{E_b}{N_o}}\right)
\end{aligned}
\tag{2.4}
$$

Here M represents the level of QAM and PAM modulations. L represents the level of PPM modulation. Equation (2.4) assumes the symbol energy is divided equally among all the bits and the Gray encoding is used so that at acceptable SNR, one symbol error is correlated to exactly one bit error. The theoretically obtainable BER in different modulation formats at different Eb/No (in dB) is calculated and presented in Figure 2.7. For instance, one can see that BPSK, QPSK, and 4QAM modulations require a minimum E_b/N_o of around 12.5 dB and 8.5 dB to possess $BER \leq 10^{-9}$ and $BER \leq 10^{-4}$, respectively. In contrast, the PAM-4 and the PAM-8 modulations require very high E_b/N_o (more than 25 dB) to maintain $BER \leq 10^{-9}$. The R_b (that maintains a $BER \leq 10^{-9}$) for different carrier frequencies, modulation schemes, and microwave antenna sizes are calculated.

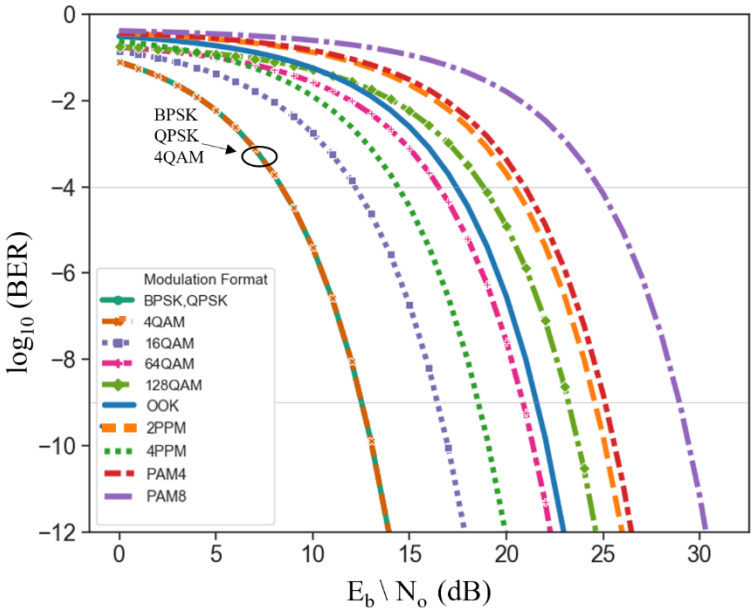

Figure 2.7. BER versus E_b/N_o for different modulation formats.

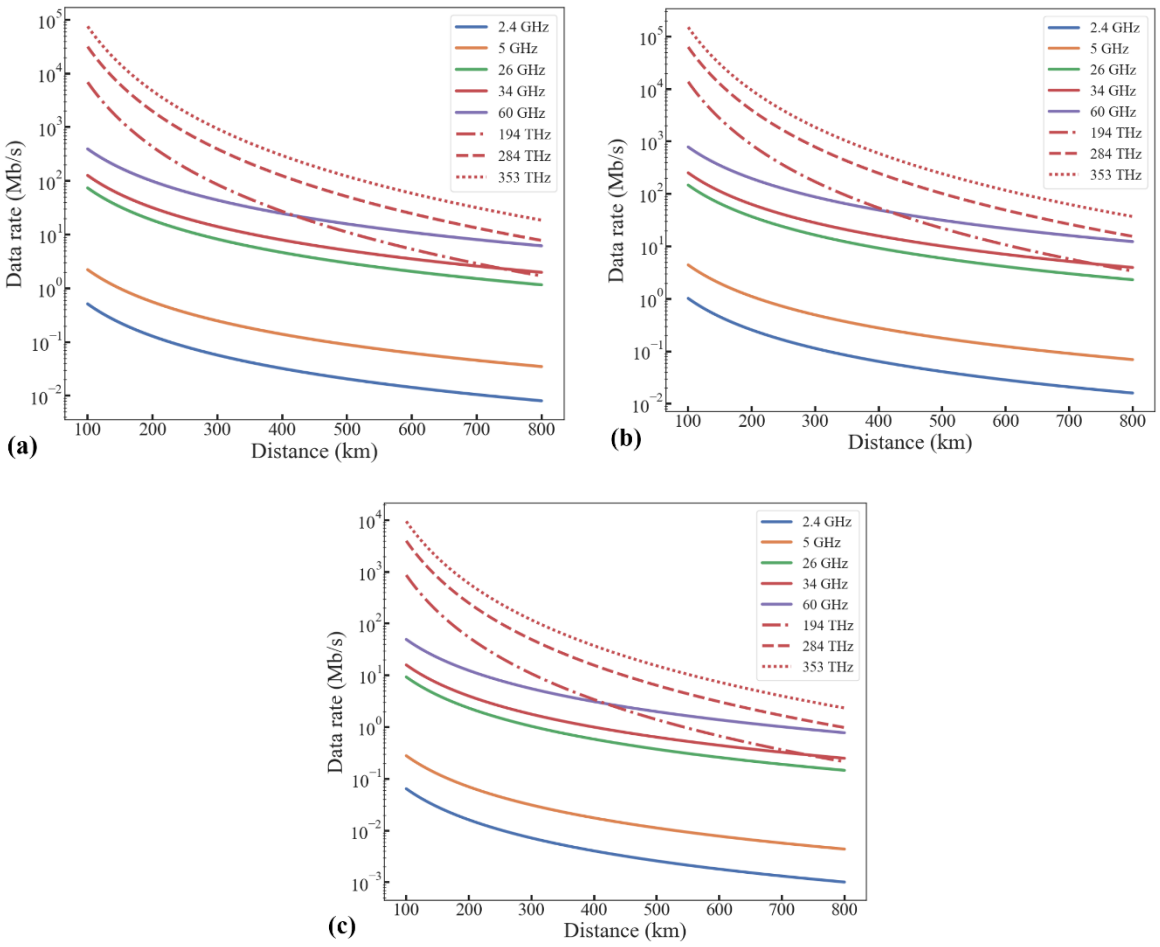

Figure 2.8. Example of achievable data rates for different carrier frequencies and modulation formats. (a)OOK, (b) 4-QAM, (c) 2-PPM.

The sample achievable data rates for OOK, 4-QAM, and 2-PPM modulation schemes are presented in Figure 2.8. In this example, a 150 mm antenna size is considered for RF and mmWave systems, whereas the optical transceiver incorporates a 10 mm transmitter aperture and a 50 mm receiver aperture. It can be seen that optical communication achieves Rb ≥ 1 Gb/s up to around 200 km communication distance that is about 1 to 2 orders of magnitude higher than that of mmWave communication. Low-frequency RF channels (2.4 GHz, 5 GHz) achieve $R_b \leq 10\,Mb/s$ when communication distance, $r \geq 100\,km$. One can notice that in shorter distances (less than about 100 km) the optical communication system is over-powered for the given modulation formats. In other

words, the theoretical achievable data rate (calculated from P_{rcv}) is much higher than the practical realizable data rate that is limited by the receiver bandwidth (in our sample analysis, that is about 1 GHz). Therefore, in shorter distances, the optical communication systems can provide 10s of Gigabits data rate if the receiver system is designed accordingly. At a very long distance ($r \geq 400\ km$), the achievable data rate of mmWave channels, as well as high-frequency RF communications (e.g. 26 GHz) exceed the data rate of the optical communication. Therefore, there exists a performance crossover region between the optical system and microwave system for given system parameters e.g. antenna sizes, optics, transmit power, receiver design, etc. The inherent low receiver noise of the microwave communication system is one of the major advantages that facilitates longer communication distance at low data rates, which is the main reason for the performance crossover. To see the performance crossover more clearly, refer to Figure. 2.9 which shows the achievable R_b at $r = 500\ km$.

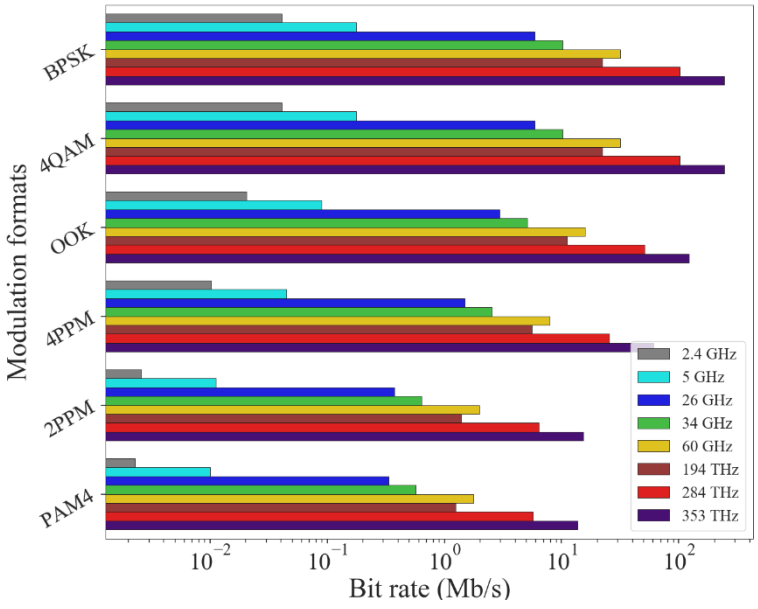

Figure 2.9. Example of achievable data rates at 500 km in different modulation formats.

The system parameters used in Figure. 2.9 are the same as those used in Figure 2.8. It can be

seen from Figure. 2.9 that a 60 GHz communication system with a 200 mm antenna can theoretically achieve a R_b of about 100 Mb/s in a BPSK modulation that is almost four times higher than that of a 194 THz optical communication (25 Mb/s).

2.4.2 The Crossover Distance and Data Rate

The crossover distance r_{cross} is defined as the communication distance above which a microwave communication system demonstrates an equal or better performance than that of a given optical communication system. The crossover data rate R_{Bcross} is defined as the data rate at $r = r_{cross}$. To compare the performance crossover, the system combinations S_c are selected from the following parameter sets: microwave frequency= {2.4 *GHz*, 5.0 *GHz*, 26 *GHz*, 34 *GHz*, 60 *GHz*}, optical frequency= {194 *THz*, 284 *THz*, 353 *THz*}, microwave antenna size= {50 *mm*, 100 *mm*, 150 *mm*, 200 *mm*}, optical transmitter aperture= {10 *mm*}, and optical receiver aperture= {50 *mm*}. Moreover, a 1.0 W transmit power for all communication links and up to 800 km communication distance (r_{lim} = 800 km) are considered for the analysis. The systems under consideration for the crossover analysis are represented as, $S_c = \begin{pmatrix} Microwave\ frequency(Microwave\ antenna\ size) \\ Optical\ frequency \end{pmatrix}$. With the design parameters given in Table 2.2, the sample crossover distances among RF, mmWave, and optical channels with different microwave antenna sizes and modulation schemes are calculated (numerically) and presented in Figure 2.10. Interestingly, the crossover distance $r_{cross}(i-j)$ between a microwave system i and optical system j is independent of the modulation scheme for a given S_c. The crossover distance for a given design parameters defined as the distance at which both microwave and optical wireless links have equal channel capacities, $C_i(r_{cross}) = C_j(r_{cross})$, where C_i and C_j denote the channel capacities of microwave system and optical systems. The following is the pseudocode for the r_{cross} estimation,

$define\ all\ S_c \begin{pmatrix} i \\ j \end{pmatrix}; i \leftarrow microwave\ system, j \leftarrow optical\ system$

$n \leftarrow total\ number\ of\ system\ combinations$

$for\ each\ S_x \in S_c \binom{i}{j}, x \in [1, n]$:

$if\ \min\ (C_{x,i}) \geq \min(C_{x,j})\ |r < r_{lim}$

$then\ \exists r_{cross,x}(i-j)|\ \left|C_{x,i}(r_{cross}) - C_{x,j}(r_{cross})\right| = 0$

$else\ r_{cross}\ does\ not\ exist\ within\ the\ considered\ range$

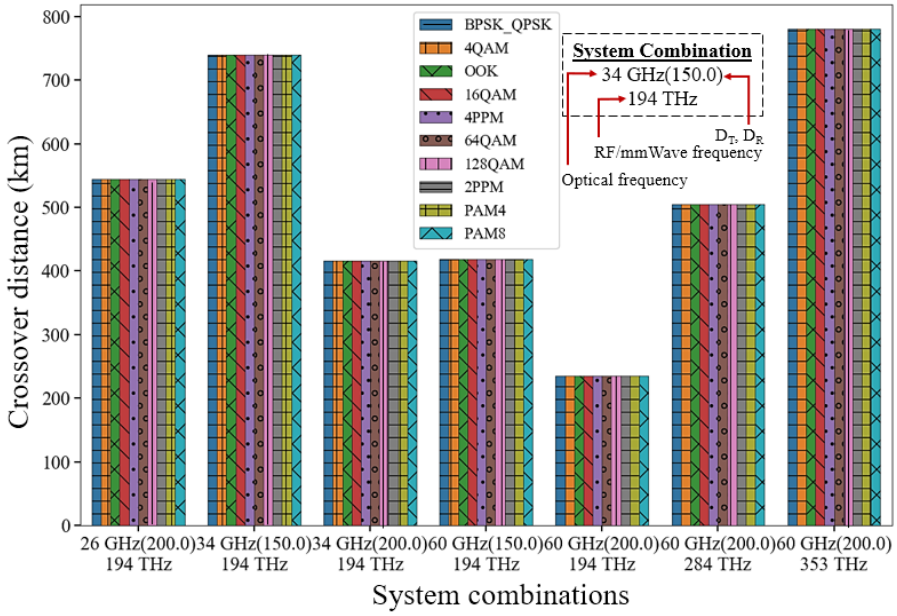

Figure 2.10. Crossover distances between microwave and optical communication systems.

It can be seen from Figure 2.10 that between the given 26 GHz (with 200 mm antenna) microwave system and the given 194 THz optical communication system, the performance crossover distance is about 540 km regardless of the modulation formats. The crossover distance changes with the system design parameters. For instance, it can be seen from Figure 2.10 that the capacity crossover distance between 34 GHz (with 200 mm antenna) mmWave system and 194 THz optical is around about 416 km i.e. 125 km smaller than that of 26 GHz and 194 THz system. Therefore, the given 26 GHz and 34 GHz microwave systems tend to perform better compared to the considered optical system at distances r > 540 km and r > 416 km, respectively. Any S_c other than the presented ones in Figure 2.10 do not have r_{cross} within the considered distance (r_{lim}). That is to say, for any other system combinations, the sample optical communications show a higher data rate than that of

RF and mmWave systems for $r \leq r_{lim}$. The R_{Bcross} of different modulation formats are quite different from each other as it depends on the required SNR per bit E_b/N_o. E_b/N_o depends on the modulation formats. Therefore $R_{Bcross} = f(E_b/N_o(modulation\ formats))$.

As an illustration, the calculated R_{Bcross} for different S_c and modulation formats are presented in Figure 2.11. One can see that the crossover data rates between 60 GHz (150 mm antenna) and 194 THz channels are 22.5 Mb/s, 44.8 Mb/s, and 2.8 Mb/s for OOK, 4QAM, and 2PPM modulation schemes, respectively.

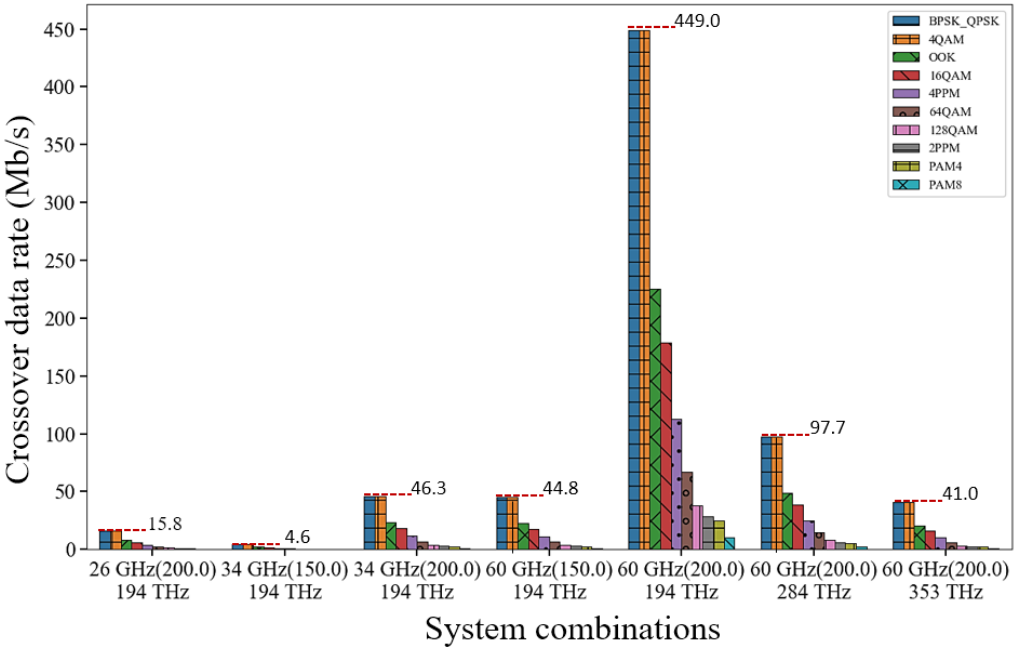

Figure 2.11. The data rate at the crossover distance for different communication systems.

The crossover data rate scales with the antenna size and the operating frequencies. It can be seen from Figure 2.11 that more than 8 times higher crossover data rate is possible between a 60 GHz and a 194 THz communication system by increasing the microwave antenna size to 200 mm. The performance crossover distance and performance crossover data rate between microwave and optical systems are dictated by the system design parameters e.g. antenna sizes, transmit power, etc. In the above-mentioned study, we provide sample calculations of the possible performance

crossovers based on the selected parameters. The analysis can be done with any design parameters set to study and understand the performance reach of the communication technologies.

Chapter 3

Omnidirectional CubeSat Crosslink by wavelength-selective transceivers

Size, weight, and power are key challenging parameters for all kind of satellite missions starting from design to launching, and day to day operations. Most of the research and development works on the satellite optical links for Low Earth Orbit (LEO) to LEO or LEO to Earth have been done either for satellites with significantly less SWaP-C constraints (when it is compared to Cubesats) or for a single point to point (one to one) data communication link. Constellation and formation fly of small satellites as shown in Figure 3.1 necessitates optical communicator with omnidirectionality and data relaying capabilities [4], [44], [47] to minimize data storage and on-board electronic processing. Omnidirectional (one to many) high-speed data communication and data relaying capability among small satellites are still open for investigation in the optical domain.

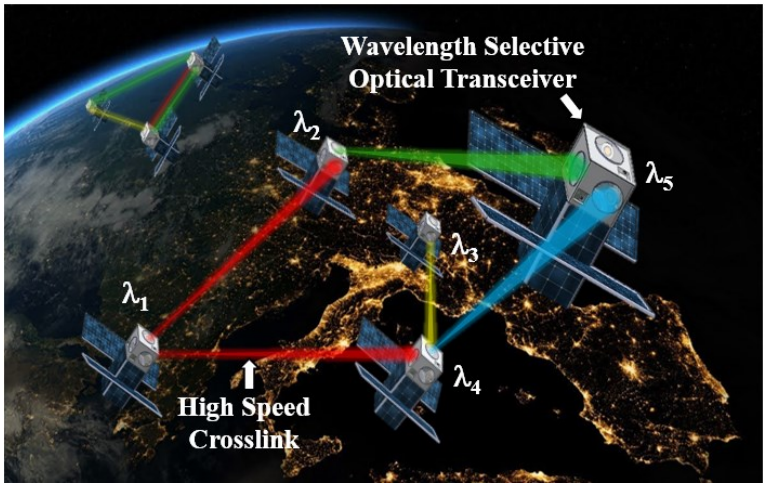

Figure 3.1. Inter CubeSat data communication using WSOT [54].

In this chapter, I present an omnidirectional optical communication design based on a CubeSat scale Wavelength Selective Optical Transceiver (WSOT) system architecture that can achieve a 360^{o} Field of Regard (FOR), longer than 100 km of communication distance, and more than 400 Mb/s data rates. This analysis utilizes Zemax based optical telescope design, experimental studies on the FlatSat model followed by numerical validation of the achievable communication range and power consumption. A conservative Bit Error Rate (BER) estimation based on the Gaussian statistical

analysis [55] is also performed on the received signal. Experimentally, it is shown that in the worst-case scenario (in the absence of advanced transimpedance amplifier, error correction coding, etc.), the achievable receiver sensitivities are -33 dBm and -29.5 dBm at 200 MHz and 400 MHz, respectively to generate BER of less than or equal to 10^{-4}. Considering the receiver sensitivity, it is estimated that with a 1 W peak transmit power (500 mW average power with 50% duty cycle) and 15 mm transceiver (TX and RX) aperture, the WSOT system can achieve communication distances up to 125 km and 80 km for 400 Mb/s and 800 Mb/s NRZ signals, respectively. The scalability of the system performance in terms of power and maximum reach is also studied in this chapter.

3.1 CubeSat Omnidirectional Antenna Design Challenges and The Transceiver Design Approaches

A wide FOR optical transmitter is a must to implement a long-range omnidirectional data communicator. The gain G_T of the optical transmitter can be increased by increasing the ratio of transmitter beam size D_T to the operating wavelength λ and can be expressed as, $G_T = \left(\frac{\pi D_T}{\lambda}\right)^2$. The wide FOR can be realized in the transmitter architecture by incorporating a fast beam scanning mechanism e.g. scanning mirrors, phased array antenna, etc. The required number of transmitters n_T can be estimated from the steering range α_s of the scanning mechanism and the required field of regard (full angle) α_{rec} and can be expressed as, $n_T = ceiling\left(\left[\frac{sin(\pi\alpha_{rec}/720)}{sin(\pi\alpha_s/360)}\right]^2\right)$. If a scanning mirror is used for the scanning purpose, the mechanical scanning angle α_{mec} of the mirror can be defined as $\alpha_{mec} \approx \frac{1}{2}\alpha_s$. Using the equation, one can find that 15, 9, and 6 independent transmitter branches are required to achieve a full field of view (360^o) by incorporating a scanning mirror with 30^o, 40^o, and 50^o full mechanical scanning ranges, respectively. Two of the most promising Commercial-Off-The-Shelf (COTS) scanning mirror technologies that can achieve wide FOR and high-speed scanning are MEMS mirror [56] and Dual Axis Vector (DAV) scanning mirror [43]. These scanning mirrors possess

tradeoffs among size, scanning speed, and scanning angle. MEMS mirrors have smaller diameter (less than 5 mm), small scanning angle (less than $\pm 7^o$) but high scanning frequency (greater than 1 kHz). In contrast, DAV mirrors are generally large in diameter (greater than 10 mm). They have a high scanning angle (greater than 25^o) but low scanning speed (smaller than 400 Hz). Based on these two different mirror mechanisms, two simple design approaches can be adopted to achieve an omnidirectional optical antenna: type A and type B (as shown in Figure 3.2). The type A approach incorporates MEMS mirrors. This type A design approach requires independent transmitter and receiver apertures due to the small transmit aperture (mirror) size. On the contrary, the type B design incorporates relatively larger DAV mirrors and therefore, it allows using the same aperture to transmit and receive signals as shown in Figure 3.2(b).

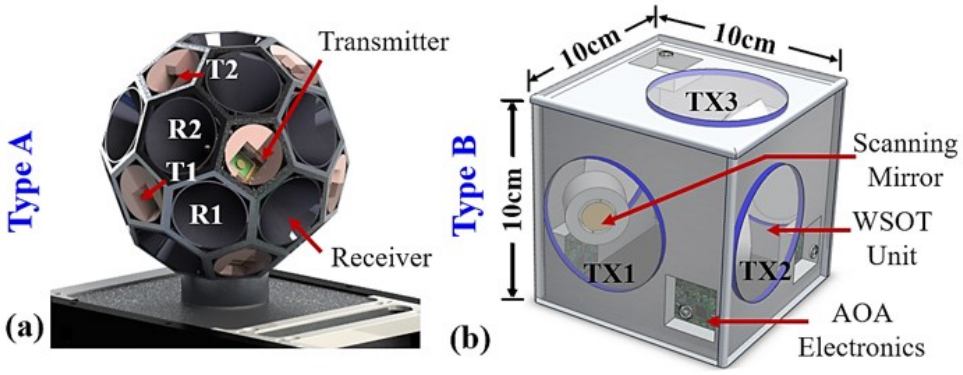

Figure 3.2. CubeSat omnidirectional optical transceiver designs.

In addition to a wide FOR transmitter, the receiver of the omnidirectional communicator must have high bandwidth, large aperture, and wide FOR simultaneously. The required average optical power P_{req} is calculated from the required Signal to Noise ratio (SNR) SNR_{req}, total noise power of the receiver σ^2, APD gain M, photodiode responsivity R_p, and can be given as, $P_{req} \geq \sqrt{(SNR_{req} \cdot \sigma^2)/(R_P^2 M^2)}$. Designing a wide FOV receiver is one of the major design challenges in designing omnidirectional optical communication. The imaging-optics-based detection system, non-

imaging beam concentrator, focal plane detector array, and fish-eye lens, etc. are the potential candidates for the wide FOV optical receiver implementation.

3.1.1 Design Challenges and Tradeoffs of Imaging and Non-imaging Optics based Receiver

The receiver design should consider the tradeoffs among the Field of View (FOV), detector bandwidth, and power collection capability of the receiver optics. Omnidirectional receiver designs can be in Imaging Optics based Receiver (IOR) architecture or Non-imaging Optics based Receiver (NOR) architecture. NORs are highly used in solar cells that possess a trade-off among optical power collection efficiency, aperture size, volume, and achievable FOV. Also, NOR architecture requires a large optical path to accommodate a wide FOV that is not feasible in CubeSat scale receiver design [57]–[59]. The FOV Ω_{FOV} of simplest IOR design (as shown in Figure 3.3) incorporating an aspheric lens along with an Avalanche Photodiode (APD) depends on the diameter of the detector H and the focal length of the focusing lens f: $\Omega_{FOV} = 2\tan^{-1}\left({}^{H}/_{2f}\right)$. It is desirable to use a large H to design a wide FOV receiver system. However, H is inversely proportional to bandwidth B and hence, wide FOV IOR receiver design has tradeoffs between detector size and bandwidth. In fact, the diameter of the available COTS high bandwidth APD (greater than 600 MHz) is less than 1.0 mm.

One effective way to increase the FOV of the detector is to incorporate a ball lens at the focal plane of the receiver lens as shown in Figure 3.3(inset). For example, a detector system incorporating a 0.5 mm photo detector and a receiver lens of 15 mm diameter with 30 mm focal length can achieve $\Omega_{FOV} = \pm 0.45^{o}$ (efficiency ≥50%) if no ball lens is used. However, it is estimated that the FOV can be doubled ($\Omega_{FOV} \approx \pm 0.9^{o}$) by using a half-ball lens of 4 mm diameter. Further FOV improvement can be achieved by using larger detectors. For instance, incorporating a 1 mm detector along with a 2 mm half ball lens can increase the FOV to $\pm 1.4^{o}$ as shown in Figure 3.3. Given a geometry and a predefined number of transmitters and receivers, the required FOV of the individual receiver in the type A architecture is in the range of 20^{o} to 65^{o} to achieve omnidirectional optical signal collection. Hence,

it is extremely challenging to satisfy both the FOV requirement and the large aperture requirement by conventional NOR and IOR design.

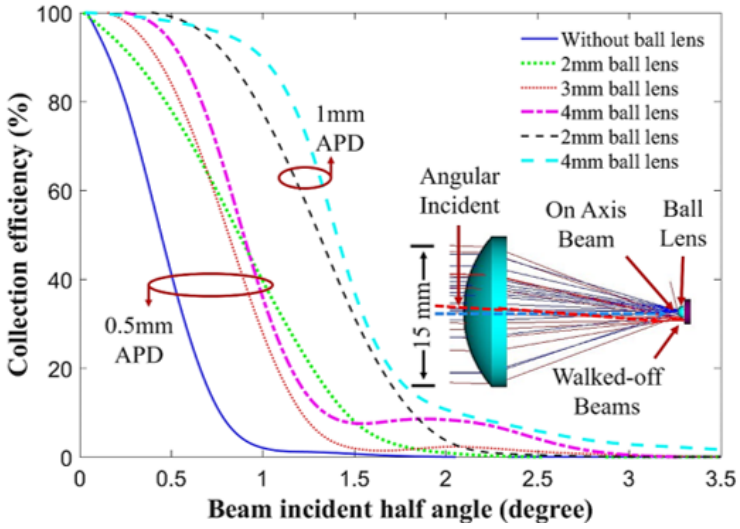

Figure 3.3. Detectors' field of view comparison.

3.1.2 Design challenges and tradeoffs in Detector Array-Based Receiver

Another seemingly possible way is to use a focal plane Detector Array (DA). A sample DA is designed and analyzed as shown in Figure 3.4 [44]. The sample DA in Figure 3.4(b) consists of 27 Detector Units (DUs). The design requires compact, bezel-less, high speed (more than 1 Gbps) detectors to attain uniform light collection. For example, DU, as in Figure 3.4(a) is designed based on the specifications of a commercial APD die (about 0.5 mm), a 1.5 mm ball lens, and a custom-designed miniature APD Chip. These DUs can be arranged to achieve a scalable Detector Array (DA) of any size and shape. An example of the compact array for the CubeSat application is shown in Figure 3.4(b). An aspheric lens aperture is used to increase the detected power and hence, to improve SNR as depicted in Figure 3.4(d).

As might be expected, the development of scalable DA possesses some design challenges and

performance limitations. First, DA's collection efficiency (P_c/P_i), where P_i and P_c are the optical power incident at the aperture and optical power collected by the detector array, varies with the incident beam angle due to the form factor of the detector size and other optics. Second, the electric circuit design complexity increases with the scaling of the array as shown in Figure 3.4(c). Third, collection efficiency uniformity over a FOV depends on the number of detectors to integrate. Fourth, summing up the signals from selected detectors for a particular angle requires an advanced algorithm and owns the possibility to accumulate noise. Last, multiple DAs with a mechanical rotation system is required to achieve omnidirectional data communication and relaying, which brings significant mechanical design complication.

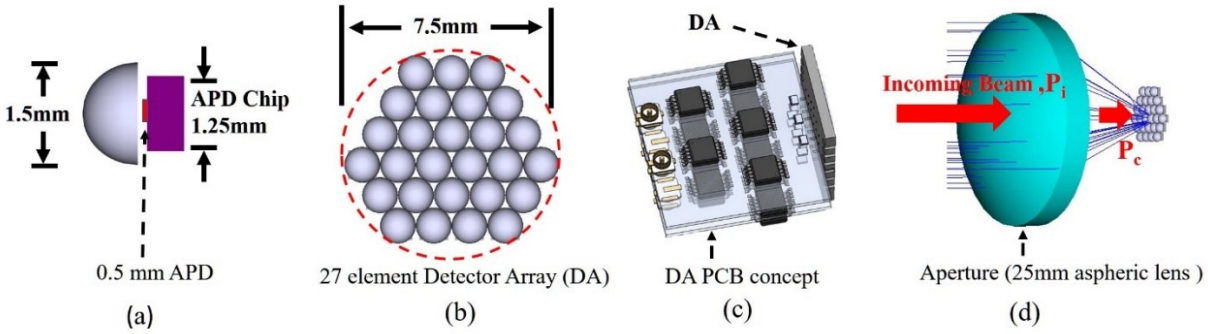

Figure 3.4. (a) DU made up of a small ball lens, an APD die, and an APD circuit, (b) Detector array consists of 27 DU in an about 7.5 mm diameter circle, (c) DA printed circuit board concept, (d) A 25 mm aspheric lens aperture to increase collection power [44].

Figure 3.5 shows the collection efficiency for different DA placement relative to aperture lens focal plane for both the X-axis incident angle (θ_X) variation (left) and the Y-axis incident angle (θ_Y) variation (right). It is evident from Figure 3.5 that the ball lens increases individual detectors' FOV (the solid green line is wider than the dashed blue line). The mean collection efficiency with the ball lens system is 57%, which is around 24% higher than the system without a ball lens when that the DA is positioned at 0.0 mm relative distance from Focal Plane (FP) (Table 3.1). As a result, the collection efficiency is significantly higher in the presence of the ball lens. For example, assuming that

the DA is placed 3.0 mm further from FP, the collection efficiency is 37% with the presence of the ball lens and 10% without the ball lens. It can be seen that the placement of the DA is important to achieve the desired performance. Placement of the DA at the FP of the aperture lens decreases collection efficiency uniformity due to the form factor of DA. It can be seen from Figure 3.5 that despite attaining about 98% maximum collection efficiency at some discrete angle, the collection efficiency curve consists of periodic dips if the DA is placed right at the FP of the aperture lens. Indeed, this system shows a very high standard deviation (σ) of around 41%. Consequently, this DA placement is not suitable for dynamic communication system, where two communication nodes are continuously changing positions as in inter-satellite communications.

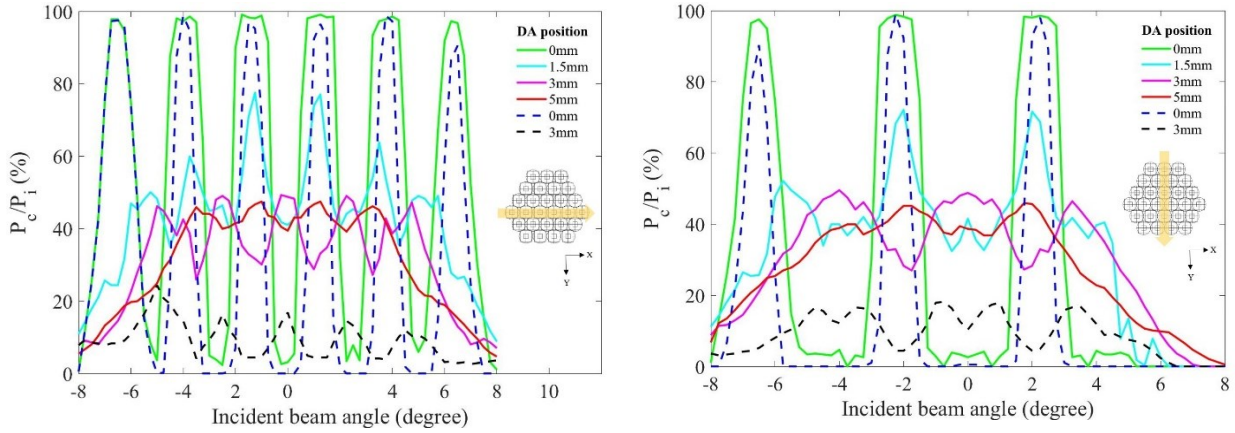

Figure 3.5. The collection efficiency of DA with incident angle variation along X-axis (left) and along Y-axis (right). The solid lines and dashed lines represent the DA system with mounted ball lens and without ball lens respectively [44].

Table 3.1 The collection efficiency of the detector array.

Incident angle	$-6^o \leq \theta_X \leq 6^o$						$-7^o \leq \theta_Y \leq 5^o$					
Mounted ball lens	✓	✓	✓	✓	x	x	✓	✓	✓	✓	x	x
DA position w.r.t FP (mm)	0	1.5	3	5	0	3	0	1.5	3	5	0	3
μ (rounded) in %	57	49	37	36	33	10	30	40	37	34	15	11
σ (rounded) in %	41	10	8	9	40	5	41	14	11	10	34	5

It is evident from the above-mentioned discussion that by the optimum design of detector array

a very wide full field of view (greater than 12^{o}) is achievable. This DA can achieve the required SNR to achieve high-speed data communication. Deciding the number of detectors to integrate into achieving uniform collection efficiency over a particular collection angle is crucial in designing a detector array. In the above-mentioned system, integration block (# of detectors that signals are added to improve performance) is assumed to be composed of closely located 1, 3, 5, 6 detectors for DA position of 0.0 mm, 1.5 mm, 3.0 mm, and 5.0 mm from the aperture lens's focal plane accordingly. Admittedly, the electronics design and signal analysis complexity increase with the number of detectors in the integration block and limit the design flexibility. Therefore, in the simulation, the number of detectors in the integration block are chosen considering the design feasibility. Nevertheless, with the optimum design of DA decision circuits and sophisticated post signal processing, this scalable detector array has the potential to attain a fast data rate and a very wide FOV in numerous free-space communication systems. The intricate optical system designs such as focal plane detector array and fish-eye lens can achieve a wide FOV. Indeed, these designs mandate larger volume, complex electronics, and less effective aperture size that may not be feasible in a CubeSat platform.

An alternative approach to circumvent the wide FOV receiver design complexities is to employ the type B transceiver design approach as shown in Figure 3.2(b). The main advantage of type B transceiver design is that it can use the same aperture to both send and receive signals. As a result, due to the reciprocity of the optical beam propagation, once the communication link is set up, the type B design approach ensures a direct line of sight communication among communication nodes. For this reason, the type B transceiver design approach is a solution to evade the design difficulties pertinent to omnidirectional communication systems described above.

3.2 Wavelength Selective Optical Transceiver Model

Considering the design complexity of multi-aperture transceiver system design and the detector

FOV requirement, here, I introduce the Wavelength Selective Optical Transceiver (WSOT) based constellation scheme that utilizes type B transceiver architecture as illustrated in Figure 3.2. In the WSOT based CubeSat crosslink scheme, each CubeSat (C_i) in a constellation of n CubeSats is assigned to a unique wavelength (λ_i) where $i \in [1, n]$ as shown in Figure 3.6. Each WSOT transceiver of the CubeSat C_i incorporates an unique dicroic filter with center wavelength λ_i and transmission bandwidth $\Delta\lambda$ so that the center wavelength $\lambda_c = \lambda_i$ and $\Delta\lambda < |\lambda_i - \lambda_{j\neq i}| \; \forall \; i, j = 1,2,3, \dots, n$. As a result, the C_i transmits signals with λ_i to other CubeSats $C_{j\neq i}$ but it can detect all other wavelengths, $\lambda \neq \lambda_i$. For instance, in Figure 3.6, CubeSat C_1 transmits λ_1 to both C_4 and C_3. However, the C_1 can detect signals of both wavelengths λ_2 and λ_4 from C_2 and C_4, respectively. The major implemetation challenges in the WSOT system based constellations arise are data packet collisions, unique wavelength allocation to each CubeSat, and fabrication of narrow bandwidth dichroic filters. The possibility of packet collision occurs in the WSOT system when two or more transmitters are in receivers FOV and at comparable distances from the receiver. In other words, a packet collision occurs if the angular separation between two transmitters (Ω_{TX}) with respect to receiver is less than or equal to full FOV of the receiver, $\Omega_{TX} \leq \Omega_{FOV}$. A collision detection protocol needs to be implemented in the media access control (MAC) layer of the netwok to overcome such problems as done in the conventional ethernet networks. The state-of-the-art ITU grids are being set at 100 GHz ($about$ 0.8 nm) channel spacing at C and L bands, and hence more than 100 wavelength channels (i.e. more than 100 satellites) can be supported. The main implementation bottleneck is the lack of available COTS narrow bandwidth dichroic notch filters. Even though only a few discrete wavelength dichroic bandpass filters are commercially available during the time of writing this dissertation, custom fabricated filters for specific wavelengths can be attained from different vendors.

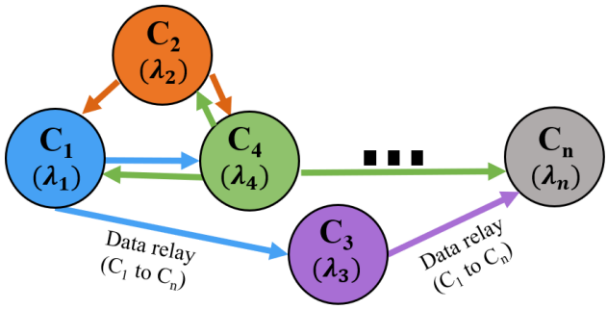

Figure 3.6. WSOT based CubeSat constellation concept [54].

The transmitter (TX) of the WSOT system design as given in Figure 3.7 incorporates a Laser diode (L) an Aspheric Lens (AL) based collimation system. A Fixed Mirror (FM) is used to make the TX channel compact to fit inside the CubeSat platform. A Dichroic Filter (DF) is integrated to enable wavelength-selective communication and to minimize the crosstalk. The receiver chain (RX) consists of a wideband filter (F), Focusing Lens (FL), and an APD as shown in Figure 3.7. A Steering Mirror (SM) of diameter $2a$ based Transceiver Aperture (TA) ensures a line of sight communication that facilitates the pointing and tracking mechanism.

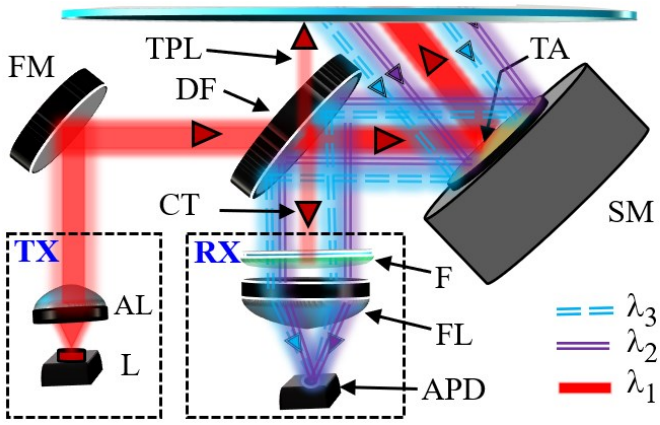

Figure 3.7. WSOT system.

The received optical power $P_{rcv}(\lambda_i)$ can be estimated from the transmit power $P(\lambda_i)$, transmitter feeder loss $\alpha_{Ti}(\lambda_i)$, receiver chain loss $\alpha_j(\lambda_i)$, geometric loss $G(\lambda_i)$, pointing loss α_p, and

atmospheric attenuation $\gamma(R)$ as, $P_{rcv}(\lambda_i) = P(\lambda_i)\alpha_{Ti}(\lambda_i)\alpha_{Rj}(\lambda_i)G(\lambda_i)\gamma(R)$.

The total power of the optical beam with wavelength λ at the collimator output can be calculated from the complex transverse electric field of the optical beam $\boldsymbol{E_c}(\boldsymbol{r},\boldsymbol{z})$ as $P(\lambda_i) = \iint |\boldsymbol{E_c}(\boldsymbol{r},\boldsymbol{z},\boldsymbol{\lambda_i})|^2 dA$. Therefore, the transverse intensity profile of the beam at a distance z is represented by $I(r,z) = \frac{2P(\lambda)}{\pi\cdot\omega(z)^2} exp\,(\frac{-2r^2}{\omega(z)^2})$. Here, r is the radial distance away from the optical axis, ω_o is the transmit beam waist (radius), $\omega(z)$ is beam radius ($1/e^2$) at a distance z. Assuming the optical length (l_{opt}) inside the WSOT transceiver is much smaller than the Rayleigh range, the intensity of the transmitted beam with a wavelength λ_i at the WSOT transceiver output of CubeSat C_i can be approximated as $I_T\big(r, z = l_{opt}\big) \approx \frac{2\,\alpha_{Ti}(\lambda_i)\,P(\lambda_i)}{\pi\omega_o^2} ex\,p\left(\frac{-2r^2}{\omega_o^2}\right)$. Here, $\alpha_{Ti}(\lambda_i)$ is the transmitter feeder loss that is a function of wavelength λ_i, the number of fixed mirrors n_{FM}, the reflectance of the mirrors $R_{FM}(\lambda_i)$, the transmission of the dichroic filter $T_{DF}(\lambda_i)$, the scanning mirror aperture radius a, and the reflectance of the scanning mirror $R_{SM}(\lambda_i)$, as described in the following equation: $\alpha_{Ti}(\lambda_i) = n_{FM}\,R_{FM}(\lambda_i)\,R_{SM}(\lambda_i)\,T_{DF}(\lambda_i)\,(1 - exp\,(-\frac{2a^2}{\omega_o^2}))$. Until the beam reaches the detector of the receiver satellite, it experiences pointing loss α_p, attenuation $\gamma(R) = \exp(-\beta R)$, the geometric loss $G(\lambda_i) = \left(1 - exp\left(-\frac{2a^2}{\omega(R)^2}\right)\right)$, receiver feeder loss $\alpha_{Rj}(\lambda_i) = R_{SM}(\lambda_i)\,R_{DF}(\lambda_i)\,T_F(\lambda_i)\,T_{FL}(\lambda_i)$, which leads to the received power, $P_{rcv}(\lambda_i) = A_{rcv}\,I_T(0,R)\,\alpha_p\,\alpha_{Rj}(\lambda_i)\,G(\lambda_i)\,\gamma(R)$. Here we define A_{rcv}, $R_{DF}(\lambda_i)$, $T_F(\lambda_i)$, $T_{FL}(\lambda_i)$, β as the area of receiver aperture, the reflectance of the DF at λ_i, the transmission of F, the transmission of the FL, and the atmospheric attenuation factor, respectively. Assuming shot noise σ_s and thermal noise σ_T are the two dominant noise sources, the SNR of the detected signal can be estimated as $SNR \approx \frac{I_{sig}^2}{\sigma_s^2+\sigma_T^2}$. Given that the photodiode responsivity at λ_i is $R_p(\lambda_i)$, in the absence of crosstalk and negligible attenuation in space ($\beta \approx 0$), the signal photocurrent can be given as [54]

$$I_{sig} \approx 2M\, R_P(\lambda_i)\, P(\lambda_i)\, \alpha_{Ti}(\lambda_i)\, \alpha_p\, R_{SM}(\lambda_i)\, R_{DF}(\lambda_i)\, T_F(\lambda_i) T_{FL}(\lambda_i) \left(1 - exp\left(-\frac{2a^2}{\omega(R)^2}\right)\right) \quad (3.1)$$

The above-mentioned relations assume negligible crosstalk generated by optical duplexer. As a matter of fact, at the duplexer, an incident beam splits into three major beams: reflected beam, transmitted beam, and crosstalk component (C_T, the fraction of transmit power that goes to the receiver). In our experiment, we measure the crosstalk power by using a COTS beam splitter and a dichroic filter with an 808 nm laser source. An AR-coated non-polarizing beam splitter (700-1000 nm) has a split ratio of 50:50. With the incident optical power, $P_i = 10.4\ mW$, the measured crosstalk power of the beam splitter is 12.4 $\mu\ W$, that is C_T> 0.1%. In such a system, a 500 mW transmit power generates $C_T > 0.5\ mW$ which is deleterious for long-range, extremely power limited CubeSat communication system. On the contrary, the measured C_T of an example dichroic filter is about 4 nW for $P_i = 10.4\ mW$. Therefore, the C_T of a DF based duplexer is about -65 dB, whereas the C_T of a BS based duplexer is around -30 dB. Therefore, DF-based WSOT design as described above can increase the receiver sensitivity by suppressing the crosstalk components. Additionally, the careful optical design as shown in Figure 3.8 eliminates back reflection from the optics surfaces.

The mechanical feasibility of the WSOT system in the CubeSat platform is also studied through Zemax optical simulation. The example optical design (using Zemax) is given in Figure 3.8. Figure 3.8 shows the dimensions of the optics and the required spacings. The scanning mirror dimension is taken from manufacturers' specs. It is discernible from Figure 3.8 that up to 5 WSOT units can be incorporated in less than 2 U (1 U=10 cm x 10 cm x 10 cm) to achieve about 360^o FOR and to maintain multiple high speed (greater than 400 Mb/s) laser communication link.

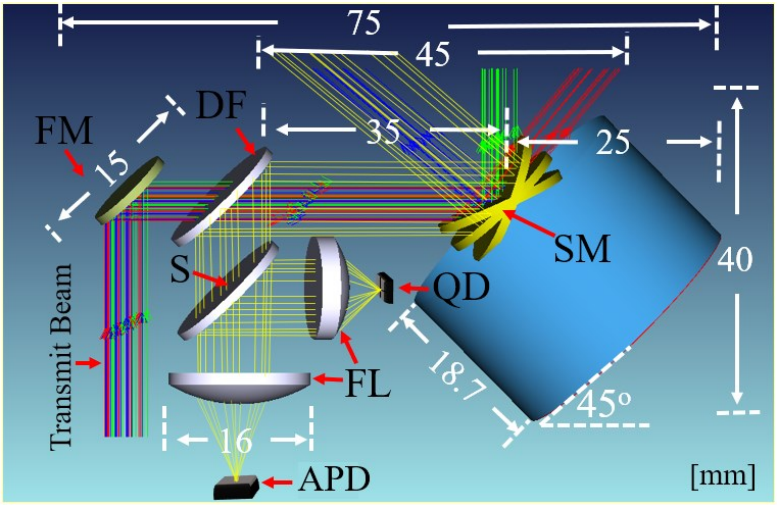

Figure 3.8. WSOT transceiver dimensions in millimeters.

3.3 System Performance of WSOT System

3.3.1 Test Bench for WSOT System and Performance Evaluation

To evaluate the performance of the WSOT system, two FlatSat models (TRX1 and TRX2) on an optical table are assembled as shown in Figure 3.9 to establish a full-duplex communication. As proof of concept, we use two lasers at 808 nm and 880 nm to mimic two satellites. An 850 nm long-pass DF and an 850 nm short-pass DF are also incorporated due to their availability and low cost. The lasers are then collimated using COTS aspheric lens to achieve a 10 mm transmit beam diameter. Two dichroic filters DF1 and DF2 are integrated into the systems as duplexers. DF1 and DF2 are selected such that, DF1, DF2 allow to pass λ_1 and λ_2, respectively and reflect λ_2 and λ_1 to the respective receiver. Moreover, 15 mm beam steering mirrors (SM) are also incorporated in the FlatSat model of the WSOT system. The power loss is measured at 880 nm that is transmitted by the TRX1. The receiver is fabricated using commercially available 1.00 mm Silicon Avalanche Photodiode (APD) with responsivity $R_p = 0.5$ (M=1), dark current $I_D = 2\,nA\,(max)$, excess noise figure $F_A = 0.3$ $(at\ \lambda = 800\,nm)$, and cutoff frequency, $f_c = 600\,MHz$. The APD is biased at 130 V to achieve a gain (M) of about 100.

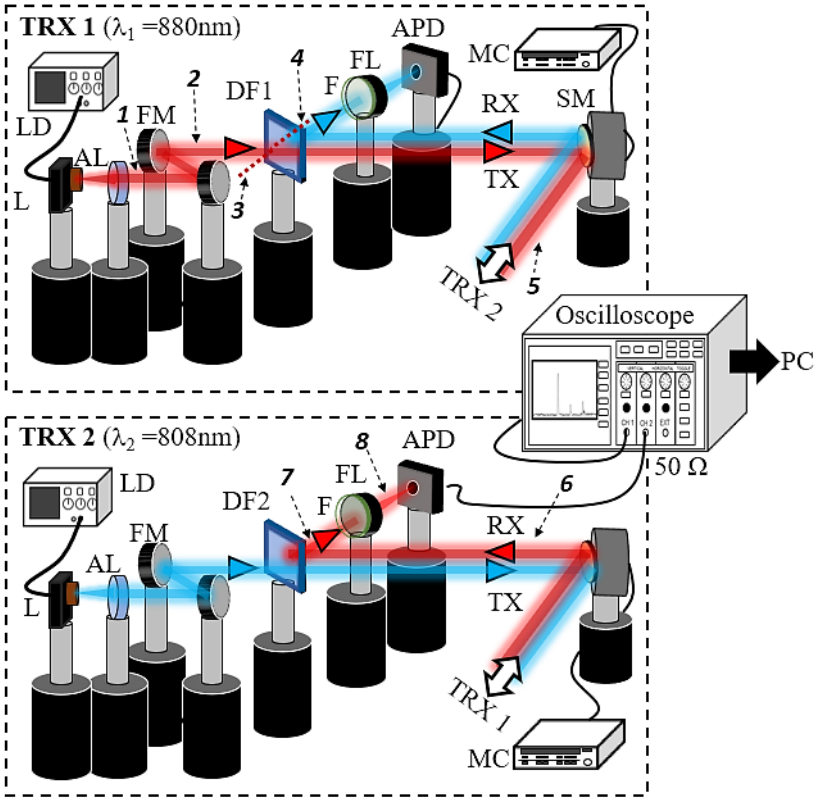

Figure 3.9. Experimental setup of the WSOT system [54].

A narrow bandpass filter, F is incorporated with the focusing lens FL in each receiver to reduce ambient noise. The APD is terminated at a 2.0 GHz digital oscilloscope with a 50 Ω termination resistor. The average optical power is measured at each measurement point i= [1, 8] as shown in Figure 3.9 to analyze the system power loss and performance.

We measure the optical losses in the Transmitter Chain (TC) and Receiver Chain (RC) of the wavelength selective transceiver. The TC is comprised of a laser collimation system, FM, DF, and TA (scanning mirror). The RC includes TA, DF, F, FL, and APD as given in Figure 3.7. Therefore, optical power loss in the TC, $L_{TCL} = L_{AL} + L_{FM} + L_{DF} + L_{CT} + L_{TA}$ and the receiver chain loss, $L_{RCL} = L_{TA} + L_{DF} + L_F + L_{FL}$. Here, x, the subscript of L_x denotes the respective optical component i.e. $x \in \{AL, FM, DF, CT, TA, DF, F, FL, M\}$ as in Figure 3.9. As a result, total optical power loss L_{OL} depends

on the communication distance R, static loss $L_{SL} = L_{TCL} + L_{RCL}$, pointing loss L_{PL}, divergence angle of the transmit beam δ, and limited receiver aperture radius a and in dB scale can be expressed as

$$L_{OL}\big(R, a, \delta(\omega_o, \lambda)\big) = L_{TCL} + L_{RCL} + 10 \cdot log\left(\frac{a^2}{R^2 + tan^2(\delta(\omega_o, \lambda))}\right) + L_{PL} \qquad (3.2)$$

In this analysis, the total attenuation coefficient is assumed to be zero, $\beta = 0$. The static optical power loss of the WSOT is statistically measured. The measured optical power loss at different measurement points (i= [1, 8]) of the WSOT transceiver are summarized in Table 3.2. The total static power loss of the WSOT system L_{SL} is about 1.6 dB as shown in Table 3.2. The measured crosstalk factor of the DF, C_T is about $-65\ dB$. The required pointing accuracy ε to keep the optical throughput loss less than 3 dB of the inter satellite optical communication can be approximated as, $\varepsilon \approx \frac{\lambda}{40\omega_o}$. The state-of-the-art onboard sensors have an angular resolution in the order of about 1 μrad and therefore, the required pointing accuracy can be obtained using currently accessible technologies[48], [60], [61]. As considered in many literature (e.g. [60], [62]), a 3 dB pointing loss i.e. $L_{PL} = 3\ dB$ is considered in the link loss calculation. The total optical power loss of the WSOT system with a 15 mm receiver aperture is presented in the Figure 3.10. For instance, it can be seen from Figure 3.10 that 13 mm and 7 mm initial transmit beams experience about 60 dB optical power loss at a distance of 100 km and 40 km, respectively.

Table 3.2 Optical power loss of WSOT transceiver.

Test Point	Symbol	Description	Power Loss (dB)
1	L_{AL}	Collimation loss	-0.2
2	L_M	Mirror loss	-0.15
3	L_{DF}	Dichroic filter loss	-0.12
4	C_T	Crosstalk factor of DF1	≈-65
5	L_{TA}	Scanning mirror loss	-0.18
6	L_{TA}	Scanning mirror loss	-0.18
7	L_{DF}	Dichroic filter loss	-0.07
8	L_F+L_{FL}	Filter and lens loss	-0.7
	Total static loss, L_{SL}		-1.6

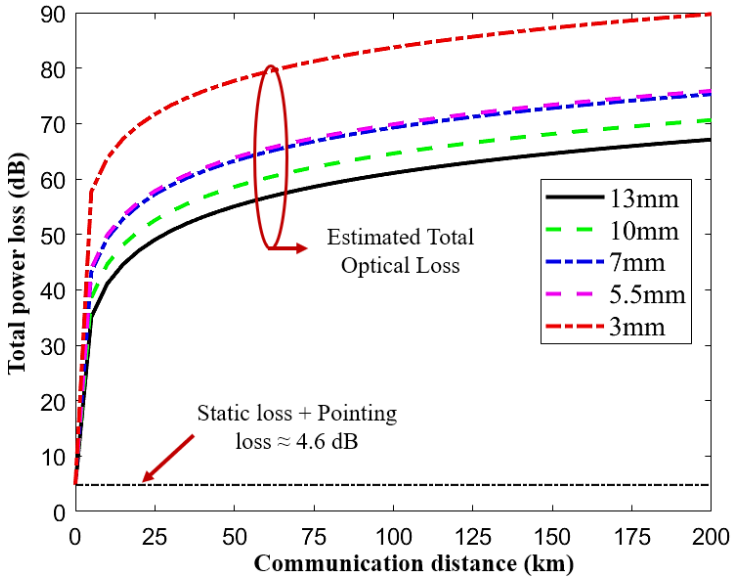

Figure 3.10. Total optical loss of a WSOT system.

It is obvious from Figure 3.10 that a larger transmit beam size (ω_o) experiences smaller optical loss as predicted from Eq. (3.2). Therefore, longer communication is achievable with a larger initial beam size. Five commercially available collimators (3 mm, 5.5 mm, 7 mm, 10 mm, and 13 mm) are considered for the power loss calculation. In this study, transmitter beam size and corresponding divergence data are incorporated from commercially available optical collimators[63]–[65]. Therefore, the non-ideal effects of the optics inside the collimators are considered in the Zemax simulation. The relevant transmitter beam size and half divergence angle data for these collimators are summarized in Table 3.3.

Table 3.3 Beam size and divergence angle of cots collimators.

Beam Diameter(mm)	Divergence Angle (Deg)	Beam Diameter(mm)	Divergence Angle (Deg)
2.1	0.053	7.0	0.0072
3.0	0.038	10.0	0.0042
3.6	0.016	13.0	0.0028
4.5	0.0086	15.8	0.0025
5.5	0.0077	16.5	0.0023

The total power loss-distance relation as in Eq. (3.2) is nonlinear. However, from link designers'

perspective, it is often convenient to quantify power loss in linear scale e.g. dB/km. It is observed that in long-distance communication (R ≥ 100 km) the total power loss w.r.t. distance can be approximated with a linear model. That is, total optical loss at a distance R (in km) can be approximated as $L_{OL} = L_o + m \times (R - 100)\ and\ R \geq 100\ km$. Here, L_o and m are the total power loss at 100 km and slope of the linear fitted curve, respectively. Sample Linear Least Square Fit (LLSF) on the estimated total power loss curve is shown in Figure 3.11. Interestingly, the slopes of the linear fits are equal and independent of the initial beam size and divergence angle. This is evident from the parallel fitted lines as shown in Figure 3.11. For instance, it can be noted that the linear fits of the optical power loss of all initial beam sizes e.g. 13 mm, 10 mm, 7 mm, etc. have the same slope. The approximated distance-dependent incremental power loss (slope of the fitted curve, m) is 0.032 dB/km.

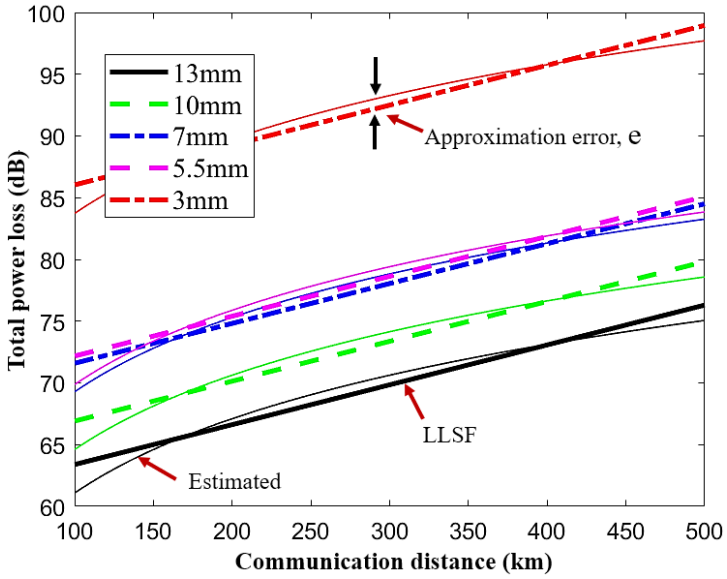

Figure 3.11. Linear approximation of the total optical power loss.

It is also found that due to the small receiver aperture ($a << R$) the slope of the linear fit is also found to be independent of the receiver aperture. The linear fitted lines of the power loss considering four different receiver apertures (10 mm, 15 mm, 20 mm, 30 mm) are shown in Figure 3.12.

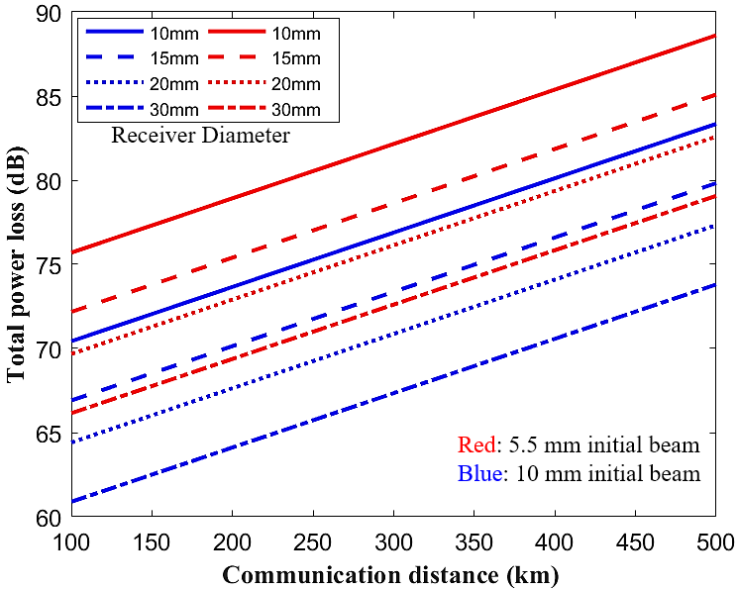

Figure 3.12. Linear approximation of the power loss for different receiver sizes.

Two initial beam sizes (5.5 mm and 10 mm) are considered in this analysis for the comparison purpose. Evidently, all fitted lines in Figure 3.12 have the same slope *m* regardless of the initial beam size and receiver dimension. The constant term, L_o of the LLSF fits for different initial beam size and different receiver diameter are summarized in Table 3.4. The parameters, L_o and *m* can produce close estimation of the total power loss of WSOT system with different initial beam sizes and receiver aperture size. For example, given that a WSOT system is designed with a 10 mm initial beam size and a 15 mm receiver aperture, the estimated total optical power loss of a 200 km free-space link can be estimated as $L_{OL(est.)} = 66.9 + 0.032 \times (200 - 100) = 70\ dB$. That is close to 70.6 dB, the value estimated from Eq. (3.2) and shown in Figure 3.10. Furthermore, the RMS error between actual estimation and linear approximation is calculated as $e_{rms} = 0.78\ dB$. The maximum error and standard deviation are calculated as 2.3 dB and 0.78 dB respectively for all initial beam width and receiver size combinations. This error calculation based on the curve fitting is applicable for 100 km ≤ R ≤ 500 km.

Table 3.4 Parameters of the linear fit model, L_o (dB).

Beam size, ω_o (mm)	Receiver lens diameter (mm)			
	10.0	**15.0**	**20.0**	**30.0**
3.0	89.6	86.1	83.5	80.1
5.5	75.7	72.2	69.7	66.2
7.0	75.1	71.6	69.0	65.6
10.0	70.4	66.9	64.4	60.8
13.0	66.9	63.38	60.9	57.4
	The slope of the linear fit, $m = 0.032\ dB/km$			

3.3.2 Power Consumption Estimation

The power consumption of the major active components of the given WSOT system is estimated in this section. Figure 3.13 shows an example of a link design that includes major electrical and optical components to establish a WSOT system. Here, it is assumed that the wall-plug efficiency of the laser and optical amplifier (OA) as 16.0% and 12.5%, respectively. Also, the average optical output is assumed as 500 mW to generate 1.0 W peak power considering a 50% duty cycle. Based on different manufacturer specs, it is also assumed that the COTS transimpedance amplifier (TIA) and electrical amplifier (EA) consume 0.5 W and 0.25 W, respectively. Moreover, the Electrical Control Unit (ECU), basic Digital Signal Processing (DSP), and Data Storage (DS) can be achieved with conventional FPGAs or ASICs that consume less than 2.0 W average power. Hence, one TC-RC has a wall-plug efficiency of about 8%. Therefore, with this example system, two links (one point-to-point and one relaying) can be operated simultaneously with less than 15 W power consumption. The wall-plug efficiency of the WSOT system can be further improved by using highly efficient OA and laser diodes etc. Given that, the state-of-the-art solar panels such as eHawk can generate 72 W optical power [14], a WSOT payload will consume less than 20% of the total generated power. Since lasers are the most power-hungry components, these results are expected.

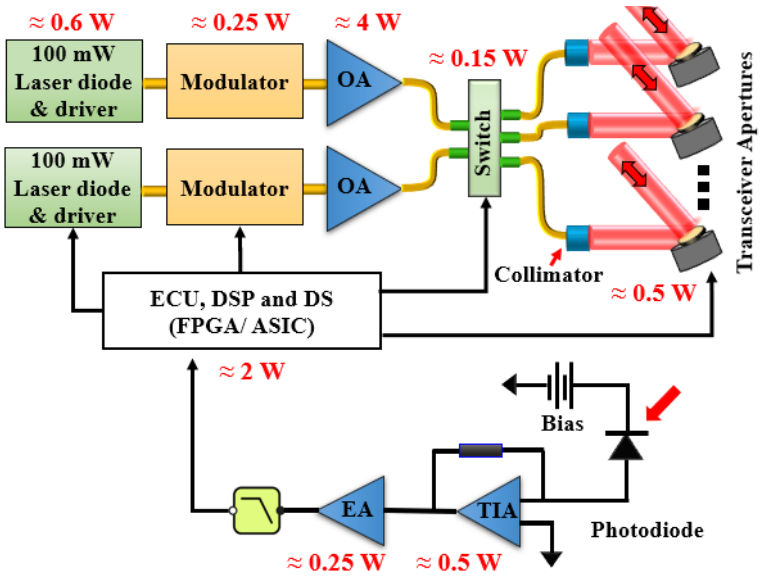

Figure 3.13. An example of the transceiver system and power consumption of the major active components of the link.

3.3.3 Data Communication Performance Test

The two FlatSat models of WSOT architectures shown in Figure 3.9 are also used to test the data communication and to characterize the communication range and Bit Error Rate (BER). Due to the immobility of the preliminary FlatSat model transceivers, a variable free space attenuator is placed in the optical path between two FlatSat to mimic the power loss due to different distances as estimated in Figure 3.10. In order to estimate the BER performance, 200 MHz and 400 MHz square wave signals with a 50% duty cycle are considered. It is known that for a given data rate, the Non-Return-to-Zero (NRZ) On-Off Keying (OOK) modulation requires only half of the baseband bandwidth. Therefore, 200 MHz and 400 MHz signals resemble approximately 400 Mb/s and 800 Mb/s data rates, respectively. A conservative BER estimation approach based on Gaussian statistical analysis is performed on the received signal that is defined as, $BER = \frac{1}{2} erfc\left(\frac{Q}{\sqrt{2}}\right)$and Quality factor, $Q = \frac{I_1 - I_0}{\sigma_1 + \sigma_0}$ [55]. I_1, I_0 are the average received signal and σ_1, σ_0 are the standard deviations corresponds to '1' and '0' bits, respectively. To characterize the system, the received signal (voltage) from the APD is captured by a 2.0 GHz oscilloscope. The captured data is then analyzed in Matlab and

Python. A histogram of a large number of signal segments (around 15,000 segments) is considered for credible statistical BER analysis. The BER vs received average optical power profile for 200 MHz and 400 MHz signals are given in Figure 3.14 and Figure 3.15, respectively. The eye diagrams at different received power levels are also given as insets.

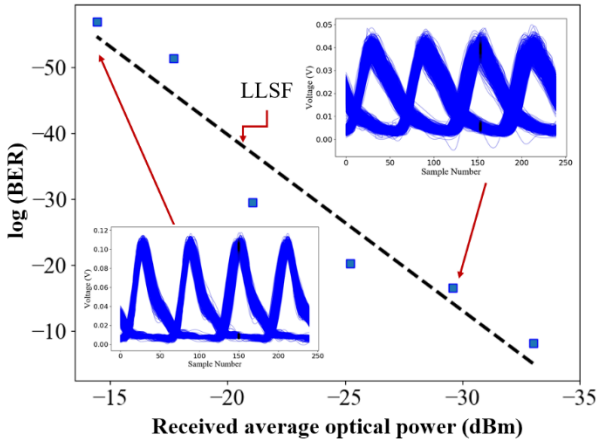

Figure 3.14. BER vs received average optical power for a 200 MHz signal (sampled at 2 GS/s).

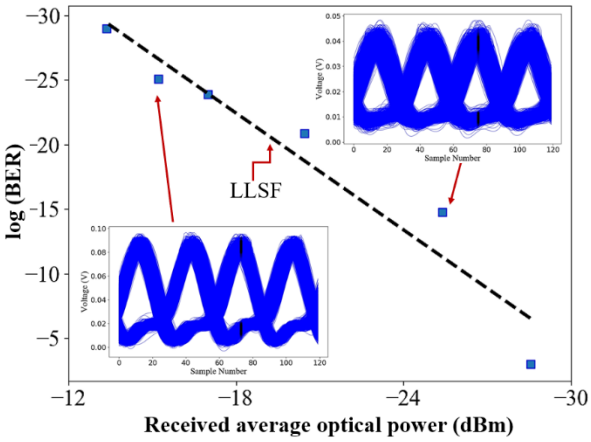

Figure 3.15. BER vs received average optical power for a 400 MHz signal (sampled at 2 GS/s).

The received signals are sampled at 2.0 GS/s. It can be seen from the figures that the minimum received power to maintain a BER ≤ 10^{-4} for 200 MHz and 400 MHz signals are measured to be $S_{200}(BER) = -33\ dBm$ and $S_{400}(BER) = -29.5\ dBm$, respectively. Note that, in this analysis, the system is characterized without incorporating any transimpedance amplifier and RF amplifier. The BER estimations are shown in Figure 3.14 and Figure 3.15 are the conservative (worst case) performance of the WSOT system.

The receiver sensitivity and estimate maximum achievable communication distance can be estimated from the above-mentioned BER analysis. Given the above-mentioned WSOT transceiver sensitivity, for a given transmit power $P(\lambda)$ and BER requirement, the maximum achievable communication distance R_{max} can be estimated by, $P(\lambda) = S_k(BER) - L_{OL}\big(R_{max}, a, \delta(\omega_o, \lambda)\big)$. Here, L_{OL} is a -ve quantity and the subscript $k\epsilon\{200, 400\}$ denotes the sensitivity of the APD receiver for 200 MHz and 400 MHz signals, respectively. The receiver sensitivity is set to achieve $BER \geq$

1×10^{-4}. To provide readers with a better understanding of the WSOT system's scalability and to compare the performances, the achievable distance is estimated for four different receiver diameters i.e. $D_R = 2a = \{10\ mm, 15\ mm, 20\ mm, 30\ mm\}$ and two signal peak powers, $P_{peak} = \{500\ mW, 1\ W\}$. For a given average power (P_{AVG}), infinite extinction ratio, and duty cycle (D_C), the theoretical attainable peak power (P_{peak}) of a laser can be estimated as, $P_{peak} > P_{AVG}/D_C$. For instance, a laser operating at a 5% duty cycle and a 0.5 W average power can generate pulses with more than 10 W peak power. Up to date, several laser technologies have been demonstrated that can provide several Watts to kilo Watts of peak power [66]–[68]. Moreover, the received power is intertwined with the transmit beam width ω_o and therefore, in the simulation, five selected COTS collimators of beam diameters $D_T = 2\omega_o = \{13mm, 10mm, 7mm, 5.5mm, 3mm\}$ are incorporated from *Table 3.3*. The achievable communication distance with BER ≤ 10^{-4} are shown in Figure 3.16 and Figure 3.17 for 200 MHz and 400 MHz signals, respectively for different D_R and P_{peak}. It can be seen from Figure 3.16(a) that a 400 Mb/s data rate is achievable up to 88 km with $D_T = 13\ mm$, $P_{peak} = 500\ mW$, and $D_R = 15mm$. For the same D_R and D_T, R_{max} exceeds 125 km when $P_{peak} = 1\ W$ as can be seen from Figure 3.16(b). Furthermore, with the same system i.e. $D_R = 15\ mm, D_T = 13\ mm$, a 800 Mb/s (400 MHz signal) data rate can be achievable up to a distance of 53 km and 80 km with 500 mW and 1.0 W peak power, respectively as shown in Figure 3.17. A larger transceiver aperture can achieve a longer communication distance with the above mentioned transmit power levels. For instance, it can be seen from Figure 3.17(b) that an 800 Mb/s data rate is achievable up to 150 km communication distance with $P_T = 1W, D_R = 30\ mm, and\ D_T = 13\ mm$. In this experiment, the output of the APD is terminated with a 50 Ohm resistor. The proof-of-concept receiver under test does not include transimpedance amplifier and baseband amplifiers. Besides, a Gaussian statistical computation of the BER is adopted in the above-mentioned analysis. Therefore, the estimated link parameters (e.g. receiver sensitivity, communication distances, etc.) are the worst-case scenario estimation of the WSOT link. The performance of the system can be improved further by advanced

receiver circuit design, error correction coding, and optics optimization.

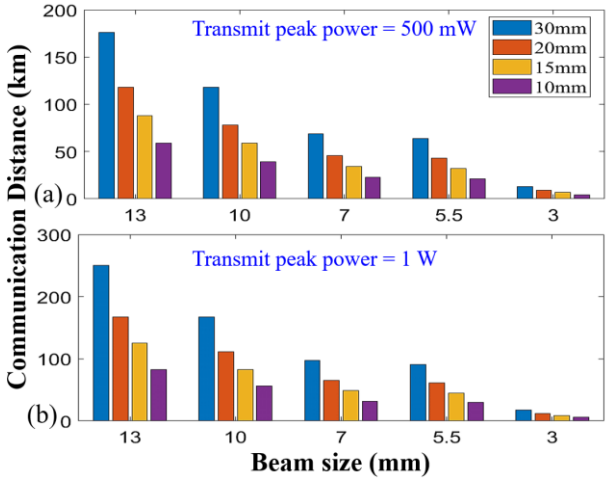

Figure 3.16. Communication range estimation for 400 Mb/s WSOT system.

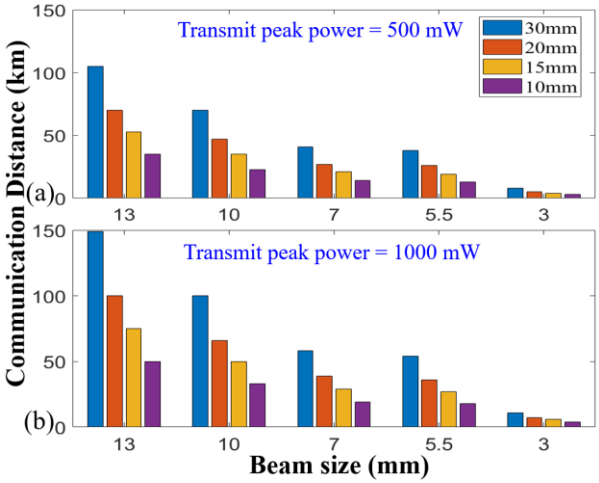

Figure 3.17. Communication range estimation for 800 Mb/s WSOT system.

Chapter 4

Transmitter Optics Optimization for Omnidirectional CubeSat Optical Crosslink

Omnidirectional Optical Transceivers (OOT) are necessary to provide connectivity among multiple small spacecrafts to enable full-sky coverage without expensive intermediate ground relay stations as illustrated in Figure 4.1. In this chapter, the emphasis is on the system level optics integration and design rules to achieve omnidirectional optical communication in the CubeSat platform. In particular, this study focuses on the omnidirectional transmitter design and optimization techniques. The main challenge arises from the fact that a CubeSat platform is extremely Size, Weight, Power, and Cost (SWaP-C) limited and therefore, optical system design using COTS components in such a platform requires special design and optimization rules. Additionally, the omnidirectional optical system in CubeSat is a new and demanding concept that possesses its unique design challenges.

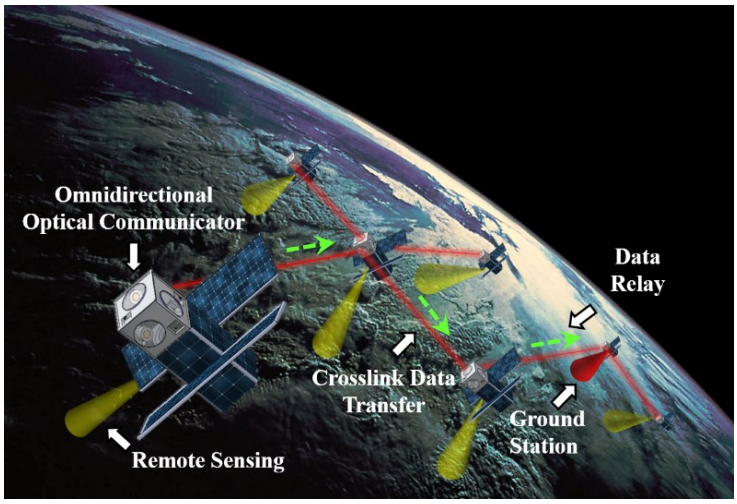

Figure 4.1. Remote sensing operation by CubeSat swarm interconnected by high-speed laser link.

A detailed study on the relations and dependencies among scanning mirror's smallest step angle, laser beam divergence, optics dimensions, communication distance, and scanning area filling efficiency, etc is presented in this chapter. Additionally, the optimization challenges of the transmit laser beam size considering the interplay among beam divergence, beam clipping, and scattering are studied in detail. This study investigates optical design methodologies, housing techniques,

component optimizations as well as performance tradeoffs among major COTS optical components (e.g. scanning mirrors, collimators, etc.) to address the challenges pertinent to OOT design. The OOT design goal is to achieve a blind spot free 360^o Field of Regard (FOR) using small scanning mirrors (less than 20 mm). In addition, the optical communication system needs to possess a communication distance greater than 100 km with data rates of more than 500 Mb/s, and high tolerance to mechanical vibrations of the host satellites. In this chapter, I demonstrate the optimization rules for aperture size, beam width, laser power, and scanning mirror specifications to achieve these goals. It is shown that the scanning mirror's small step angle should be between 0.04^o and 0.005^o to achieve a blind-spot free 360^o FOR by using 2.1 mm to 15.8 mm beam sizes. Besides, the results demonstrate that the initial beam size should be optimized to about 80% of the scanning mirror's size to achieve peak irradiance to maximize the SNR at the receiver. Furthermore, the concept of Effective Communication Beam Region (ECBR) and Effective Communication Beam Width (ECBW) to address pointing accuracy challenges due to host CubeSat vibrations and receiver position uncertainties is also presented. It is shown that the receiving CubeSat can maintain a Signal to Noise Ratio (SNR) greater than 10 dB as long as the satellite falls inside the ECBR with ECBW of 13.9 m to 41.25 m depending on the transmitted beam size, laser peak power, and communication distance. This chapter also presents the effect of laser peak power, initial beam size, and communication distance on effective communication beam width to maintain a long-distance (more than 100 km) communication with SNR ≥ 10 dB at a data rate greater than 500 Mb/s.

4.1 Transmitter Design Tradeoffs and Sample Link Budget

A small, cost-effective omnidirectional optical communicator can be fabricated using multiple transceiver apertures as in Figure 4.2(a). Each face of the CubeSat is equipped with one scanning mirror-based transceiver that possesses an optical scanning up to $\pm 50^o$. Therefore, a total of six transceiver units need to be integrated to achieve about 360^o FOR as illustrated in Figure 4.2(b). The

coverage in the Z-axis is not shown for the sake of picture clarity. A technological concept of a Low Earth Orbit (LEO) formation flying (Q4) incorporating such an omnidirectional optical cross-link had been presented before [3], [4].

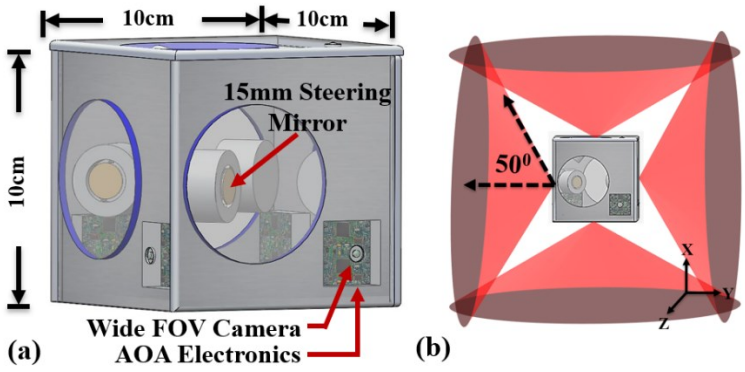

Figure 4.2. (a) A CubeSat omnidirectional optical communicator with a wide field of view camera-based Angle of Arrival (AOA) detection system (b) The concept of 360o field of regard.

To establish a free space optical link effectively, an advanced spatial acquisition and pointing system must be incorporated in the Omnidirectional Optical Transceiver (OOT). A Scanning Mirror (SM) is the foremost component in the optical pointing system. A high-speed, wide-angle scanning mirror is desirable for a fast scanning and pointing mechanism. However, the scanning capability of the SM is intertwined with its size, form factor, and driving mechanism. In a non-mechanical beam steering system (e.g. a MEMS-based, a dual-axis vector mirror-based), the scanning frequency decreases drastically with the increase of mirror size. For example, the current state-of-the-art 0.8 mm diameter MEMS mirror from a reputed vendor has a resonant frequency approximately at 4 kHz, whereas a 2.00 mm diameter MEMS mirror shows a resonance at 1.3 kHz [56]. A relatively large scanning mirror (e.g. 15 mm) offers a scanning speed of up to 350 Hz [43]. Additionally, the mirror dimension and driving mechanism determine the maximum achievable scanning angle. For instance, commercially available high-speed MEMS mirrors have a diameter of 0.8 mm to 7.5 mm with a mechanical scanning angle of less than $\pm 7^{o}$. On the contrary, relatively slow dual-axis vector scanning mirrors (5 mm to 16.5 mm) have mechanical scanning of about $\pm 25^{o}$ as shown in Figure

4.2. Therefore, the scanning mirror needs to be selected considering the interplay between mirror size, mirror speed, scanning angle, and form factor.

In the far-field ($R \gg Rayleigh\ range$), the full divergence angle, 2δ ($1/e^2$ diffraction angle) of a Gaussian beam is assumed to be constant. The divergence angle is inversely proportional to the initial beam waist (ω_o) and also proportional to the wavelength (λ), and beam quality factor M^2 as described in [69], [70], $2\delta \approx M^2 \frac{2\lambda}{\pi\omega_o}$. Since deviations from Gaussian beam requires a detailed discussion of specific beam profiles and possible laser modes, a Gaussian beam with $M^2 \approx 1.0$ is assumed in all analyses presented in this paper. In many applications, the scanning mirror's diameter (D_m) limits the allowable transmit beamwidth (D_T), $D_T < D_m$. Obviously, incorporating a beam expander after the scanning mirror might seem to be a functional way to achieve a larger transmit beam waist than the scanning mirror size as presented in Figure 4.3. Figure 4.3(a) and (b) show the scanning mechanisms incorporating a Galilean beam expander and a Keplerian beam expander, respectively. The collimated beam is first steered by the scanning mirror that creates an angle, θ_{in} at the input of the beam expander as can be seen from Figure 4.3. The beam-is expanded by a beam expander and finally makes an angle of θ_{out} at the output aperture. The Galilean beam expander is comprised of a concave lens (CC) and a convex lens (CV) with focal lengths of FL_1 (-ve) and FL_2 (+ve), respectively as shown in Figure 4.3(a). The Keplerian beam expander incorporates two convex lenses with focal lengths of FL_1 (+ve) and FL_2 (+ve) as presented in Figure 4.3(b). Both beam expander systems can be represented by the renowned ABCD ray matrix:$[r_{out}\ ; \theta_{out}] = [A \quad B; C \quad D][r_{in}\ ; \theta_{in}]$. Here, r and θ correspond to the ray position and the ray angle. A= $\delta r_{out}/\delta r_{in}$, $B = \delta r_{out}/\delta\theta_{in}$, $C = \delta\theta_{out}/\delta r_{in}$, and $D = \delta\theta_{out}/\delta\theta_{in}$ represent spatial magnification, angle to position mapping, position to angle mapping, and angular magnification, respectively.

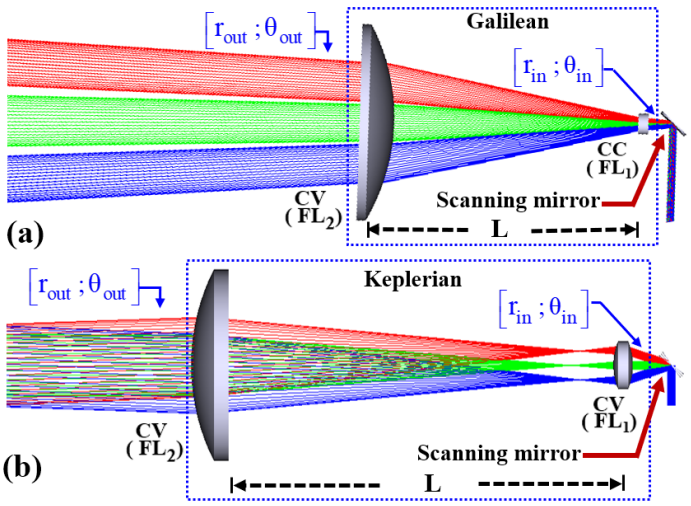

Figure 4.3. Free space optical transmitter, (a) Galilean beam expander-based system and (b) Keplerian beam expander-based system.

The ABCD matrix for both Keplerian and Galilean telescopes can be represented as follows,

$$\begin{bmatrix} A & B \\ C & D \end{bmatrix} = \begin{bmatrix} 1 - \frac{L}{FL_1} & L \\ \frac{L - FL_1 - FL_2}{FL_1 \cdot FL_2} & 1 - \frac{L}{FL_2} \end{bmatrix}$$

The beam expanders are afocal systems, therefore $L = FL_1 + FL_2$. It is evident from the ABCD matrix that the spatial magnification for both telescopes is $\left|-FL_2/FL_1\right|$, whereas the angular magnification is $\left|-FL_1/FL_2\right|$. Hence, a beam expander-based transmitter reduces the scanning angle by the same factor as it expands the beam size. For example, if a scanning mirror is capable of optical scanning, $\theta = \pm 30^o$, incorporating a 3X beam expander (as shown in Figure 4.3) decreases the scanning range to about $\pm 10^o$. Since the reduction in beam scanning angle, as presented in ABCD matrix calculation, is not suitable for OOT design, there is no need for detailed beam analysis and discussion of the nonlinear distortions that are missing in the ABCD matrix analysis. Additionally, the scanning range at the output aperture of the transceiver determines the number (n) of the required transmitter branches (defined as the required set of optical components to transmit data) to achieve

an omnidirectional coverage, and it is described as, $n = ceiling\left(\left(\frac{\sin(\pi\alpha_{rec}/720)}{\sin(\pi\alpha_{mec}/360)}\right)^2\right)$. In this equation, α_{rec} is the required field of view (full angle) and α_{mec} is the steering mirror's mechanical full scanning range. Optical scanning angle, $\theta \approx 2\alpha_{mec}$. Using the equation, it can be estimated that 15, 9, and 6 independent transmitter branches are required to achieve a full field of view (360^o) by incorporating a scanning mirror with 30^o, 40^o, and 50^o full mechanical scanning ranges, respectively.

Considering the tradeoffs of the scanning mirror parameters, a simple and compact transmitter design concept utilizing a single collimating aspheric lens and a small MEMS mirror is shown in Figure 4.4(a). The Fixed Mirror (FM) is mounted at angle γ (degree) so that the horizontal collimated beam makes an Angle of Incidence (AOI) of β on the SM as shown in Figure 4.4(a). Given that the SM is mounted at 45^o w.r.t. the vertical axis in the example type A design, the AOI can be expressed as, $\beta = 135 - 2\gamma$. The allowable AOI (less than or equal to 22.5^o) is enforced by the projected shape of the SM from the collimated beam's perspective, and the anti-reflection coating at the aperture window. Figure 4.4(b) presents the required distance between two mirrors ρ for different scanning angles and AOI. The required transmitter diameter (TD) increases with the increase of the scanning angle of the SM for a given AOI which is also shown in Figure 4.4(b). To illustrate, for a given system design with transmitting beam diameter =3.8 mm, fixed mirror diameter = 5.0 mm, scanning mirror diameter = 6.0 mm, and TD ≤ 20 mm, it can be seen that the maximum scanning angles are 8^o , 7.2^o , and 5.8^o for AOI (β) of 22.5^o, 20^o , and 17.5^o, respectively. It can also be realized that for a given AOI, a large scanning angle requires a large TD and a larger ρ which make the omnidirectional transmitter design challenging due to CubeSat volume constraint. Additionally, due to a small transmit aperture, type A transmitter design requires an independent transmitter aperture and receiver aperture.

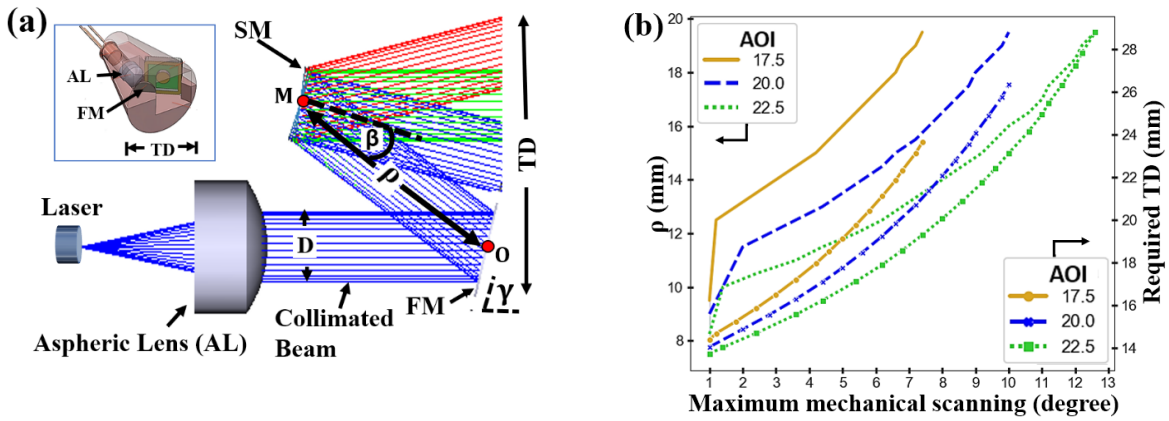

Figure 4.4. (a) Type A transmitter design, (b) required ρ and TD for different scanning angles of a type A transmitter.

A second design approach (Type B) can manifest a smaller form factor when the mirrors have a large diameter (e.g. 10 mm) and wide mechanical beam scanning angle (e.g. ±25°) as shown in Figure 4.5.

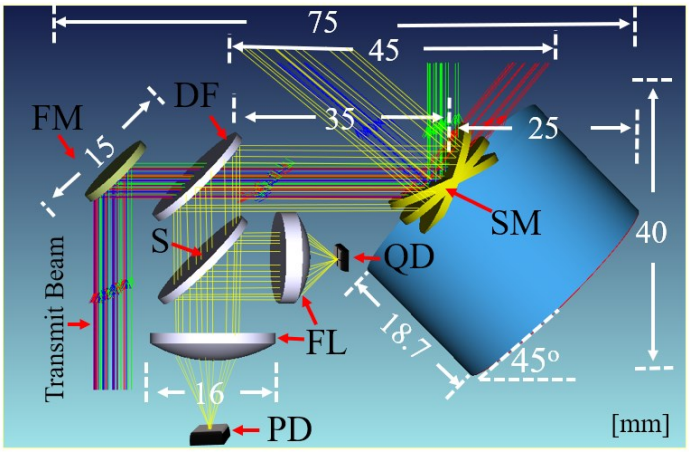

Figure 4.5. Type B transmitter design in Zemax. All dimensions are in millimeters.

Type B transmitter can be transformed into a complete wavelength selective optical transceiver with very low crosstalk (close to 0%) and low optical power loss (about 3 dB) [44]. Due to a larger mirror size compared to type A design, this design approach allows the same aperture to be used as a transmitter and as a receiver aperture. Therefore, once the communication link is established, this

transceiver design approach ensures a direct line of sight communication among multiple nodes. Type B design also evades the design difficulties related to ultra-wide FOV receiver design. The transmitter branch of type B transceiver consists of a fixed mirror (FM), a dichroic filer (DF), and a scanning mirror (SM) as shown in Figure 4.5. A Focusing Lens (FL) focuses the received optical signal on a Photo Detector (PD) e.g. Avalanche Photo Diode (APD). A small fraction (about 5%) of the received signal is sampled by a beam sampler (S) and focused on the Quadrant Detector (QD) to generate a feedback signal for SM. This compact design approach also allows us to install up to six transmitter branches that are required to achieve omnidirectional data communication as shown in Figure 4.2.

Table 4.1 Parameters of the major transceiver components

Wavelength	850 nm	
Modulation format	OOK	
Transmit power (1 W)	30 dBm	
Transmitter aperture gain (10 mm)	91.4 dB	
Receiver aperture gain (15 mm)	94.8 dB	
Path loss (100 Km)	-243.4 dB	
Transmitter and Receiver loss	- 3.0 dB	
Spatial pointing loss, Lp	3 dB	
	8.6 dB (pointing error=δ)	
Received power	-33.16 dBm	(Lp = 3.0 dB)
	-38.76 dBm	(Lp = 8.6 dB)
Receiver sensitivity (1 GHz APD)	-50 dBm	
Receiver noise figure	-4.0 dB	
Link margin	3 dB	
Estimated data rate	615 Mb/s	(Lp = 3.0 dB)
	170 Mb/s	(Lp = 8.6 dB)

An example link budget that can achieve more than 600 Mb/s data rate up to 100 km communication distance by incorporating a high-speed 15 mm transceiver aperture is presented in Table 4.1. The data rate is calculated using the formulas given in section 2.4.1. The required E_B/N_o ratio to achieve the FEC limit is about 11.2 dB, 8.5 dB, and 20.5 dB for On-Off Keying (OOK), Binary Phase Shift Keying (BPSK), and Pulse Position Modulation-2 (PPM-2), respectively.

4.2 Mirror Small Step Size Requirement

The scanning mirror's maximum scan range determines the attainable FOR and the required number of transmitter branches. However, the mirror's Smallest Step Angle (SSA) determines the transmitter's ability to point in a certain direction inside the scanning area to establish communication links and to maintain seamless communication in a constellation. Hence, the required scanning mirror's smallest step angle needs to be determined carefully. Quasi-static scanning mode (point by point scanning) is considered in our analysis to derive the mirror's required SSA. In quasi-static mode, two filling patterns can be used to scan a scanning area efficiently: Hexagonal Filling Pattern (HFP) and Square Filling Pattern (SFP) as shown in Figure 4.6 where S_X and S_Y are horizontal and vertical scanning range of the scanning mirror. Also, D represents the transmit beam diameter at the scanning area and each dot (.) represents a single pointing point (transmit beam center) on the scanning area.

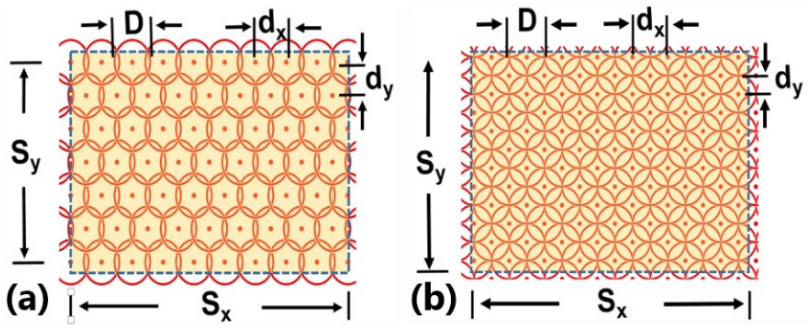

Figure 4.6. Scanning area filling pattern (a) HFP, (b) SFP.

The number of the required minimum scanning points (N) in quasi-static mode to fill an area A can be approximated by,

$$N \approx \left(8/3\sqrt{3}\right)\left({}^{S_x S_y}/_{D^2}\right) \quad for\ HFP \tag{4.1}$$

$$N \approx 2\left({}^{S_x S_y}/_{D^2}\right) \quad for\ SFP \tag{4.2}$$

It can be seen that HFP requires a smaller number of scanning points to fill the scanning area and therefore requires less time to scan in the quasi-static scanning mode. In the SSA analysis, a rectangular scanning area at a distance R from the optical transmitter is assumed as presented in Figure 4.7.

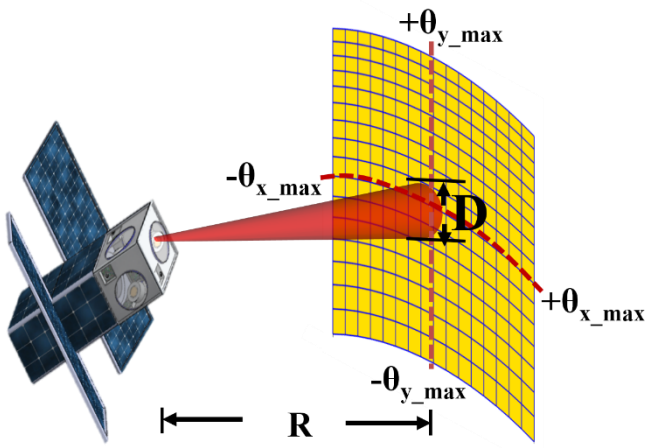

Figure 4.7. CubeSat scanning area.

Considering, R>>Rayleigh range the beam diameter at distance R can be expressed in terms of the initial beam diameter D_o and half-divergence angle δ as

$$D \approx D_o + 2R\tan(\delta) \tag{4.3}$$

Considering the above-mentioned parameters, scanning mirrors the smallest step mechanical angle (α) is calculated. The calculated scanning mirror's SSA requirements for HFP and SFP scanning pattern can be approximated as follow,

$$HFP: \alpha_x \leq \frac{1}{2}\tan^{-1}\left(\frac{\sqrt{3}D}{2R}\right) \; and \; \alpha_y \leq \frac{1}{2}\tan^{-1}\left(\frac{3D}{4R}\right) \tag{4.4}$$

$$SFP: \alpha_x \leq \frac{1}{2}\tan^{-1}\left(\frac{D}{R}\right) \; and \; \alpha_y \leq \frac{1}{2}\tan^{-1}\left(\frac{D}{2R}\right) \tag{4.5}$$

Here α_x and α_y are the required SSA for X and Y axes scanning, respectively. For most inter-satellite data communication, $R >> D$. As a result, Eq. (4.3) can be approximated as $D \approx 2R\tan\delta$.

Considering long-distance communication, the SSA for HFP and SFP can be expressed as follows,

$$HFP: \alpha_x \leq \frac{1}{2}\tan^{-1}\left(\sqrt{3}\tan\delta\right), \alpha_y \leq \frac{1}{2}\tan^{-1}\left(\frac{3}{2}\tan\delta\right) \quad (4.6)$$

$$SFP: \alpha_x \leq \frac{1}{2}\tan^{-1}(2\tan\delta), \alpha_y \leq \frac{1}{2}\tan^{-1}(\tan\delta) \quad (4.7)$$

It is obvious from Eqs. (4.6) and(4.7) that the smallest step angle requirement to achieve blind-spot free scanning is independent of the communication distance (R) and depends solely on the divergence angle (δ) in a long-range data communication. Note that, in this chapter, the blind spot is defined as the area where the transmitter is unable to point the transmitted beam inside its scanning area. Most of the commercially available scanning mirrors possess the same step angle for both axes. As a result, a scanning mirror must be selected such as the smallest step mechanical angle, $\alpha \leq min\ (\alpha_{x\_u}, \alpha_{y\_u})$ to ensure full scanning area coverage. Here α_{x_u} and α_{y_u} are the upper bound of the required mechanical SSA for X and Y axes, respectively. Otherwise, the optical transmitter contains a blind spot inside the scanning range. In our analysis, the transmitter beam size and the corresponding divergence data are incorporated from commercially available optical collimators [63]–[65]. The transmitter beam size and half divergence angle data are summarized in Table 4.2.

Using the transmit beam data provided in Table 4.2, we find the minimum step angle requirement of the scanning mirror for both Hexagonal and Square filling patterns using Eqs. (4.6) and (4.7), respectively. The upper bound of the required SSA is shown in Figure 4.8. Required mechanical small step angle of the scanning mirror. The solid lines are the nonlinear least-square fit on simulated data points.

. The required small step angle can be approximated by the fitted models shown in Figure 4.8. Required mechanical small step angle of the scanning mirror. The solid lines are the nonlinear least-square fit on simulated data points.

. The fitted models of the smallest step angle for HFP and SFP are $\alpha = 0.1245exp(-0.5748D_o) + 0.001456exp(0.02754D_o)$ and $\alpha = 0.08303exp(-0.5748D_o) + 0.0009708exp(0.02754D_o)$, respectively.

Table 4.2 Beam divergence of COTS collimators

Beam Diameter(mm)	Divergence Angle (deg)	Beam Diameter(mm)	Divergence Angle (deg)
2.1	0.053	7.0	0.0072
3.0	0.038	10.0	0.0042
3.6	0.016	13.0	0.0028
4.5	0.0086	15.8	0.0025
5.5	0.0077	16.5	0.0023

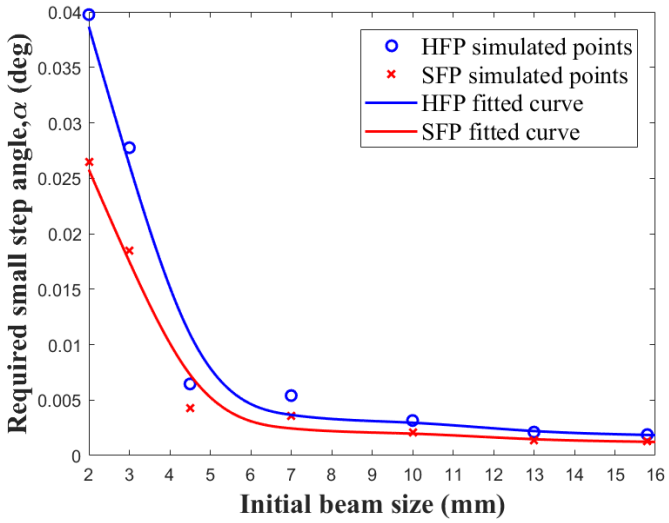

Figure 4.8. Required mechanical small step angle of the scanning mirror. The solid lines are the nonlinear least-square fit on simulated data points.

It is evident that HFP relaxes the SSA requirement more than SFP. The difference in the required α is noticeable at a smaller transmit beam. For instance, a 2 mm initial beam requires $\alpha \leq 0.0398^{o}$ and $\alpha \leq 0.0265^{o}$ for HFP and SFP, respectively. For a large initial beam such as a 13 mm transmit beam the required $\alpha \leq 0.00021^{o}$ and $\alpha \leq 0.0014^{o}$ for HFP and SFP, respectively. If the scanning mirror fails to possess the required SSA, it is useful to determine the approximate scanning area filling efficiency of the selected scanning mirror. It is evident from Eq. (4.1), Eq. (4.2), and Figure 4.8. Required mechanical small step angle of the scanning mirror. The solid lines are the nonlinear least-square fit on simulated data points.

that HFP is a more effective scanning pattern than SFP in terms of scanning time (number of required scanning points) and SSA requirement. Hence, HFP scanning is considered for the filling efficiency calculation to demonstrate the concept. Moreover, to simplify mathematical formulation and to provide an overview of the created blind spot inside the scanning area, the following assumptions are made in this analysis, i) a square scanning area ($S_X = S_Y$), ii) $\alpha_x = \alpha_y$, iii) circular laser beam, and iv) equal optical scanning range in both axes. The filling efficiency of the HFP can be expressed as Filling Efficiency (FE)=$\frac{\text{Area filled in quasi-static scan mode}}{\text{Total scanning area}}$ and is given by

$$FE \approx \frac{\pi \times tan^2(\delta)}{4 \times tan^2(\Omega/2)} \qquad (4.8)$$

Here Ω and δ are the mechanical SSA of the scanning mirror and the beam divergence angle, respectively. In our algorithm, the FE is set to 100% for $\Omega \leq \alpha_u$ where α_u is the upper limit of the required scanning mirror's smallest step mechanical angle(α). For example, in HFP the actual area filled by the 2 mm scanning beam at $\Omega = \alpha_u$ is about 140% due to the overlapped regions as in Figure 4.9, which is set to 100%. Using Eq. (4.8), the filling efficiency as a function of the upper bound of the mirror's required smallest step angle (α_u) for different initial beam size is calculated and shown in Figure 4.9. It can be seen that the filling efficiency drops to about 35% for all transmit beam size if the mirrors SSA is twice the upper bound of the required small step angle (α_u).

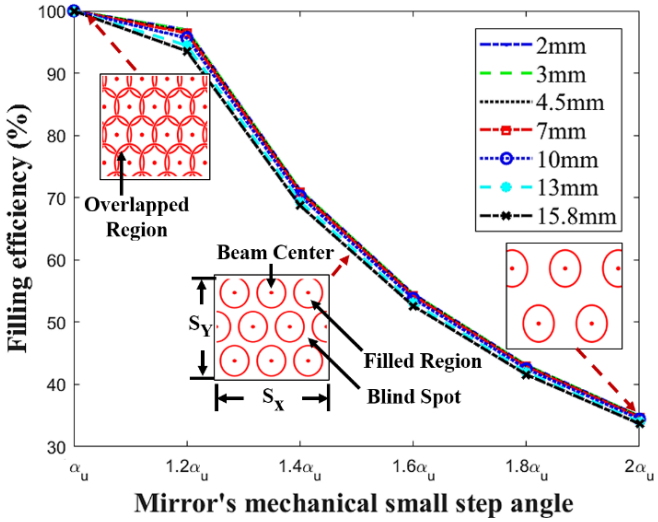

Figure 4.9. Scanning area filling efficiency for different initial beam sizes and small step angles [18].

4.3 Transmit Beam Size Optimization

4.3.1 Initial Beam Diameter to Mirror Diameter Ratio

Initial beam size needs to be optimized considering the available scanning mirror parameters (size, scanning speed, frequency) and far-field beam characteristics such as peak irradiance, beam size, etc. The peak irradiance at the far-field can be defined as, $I_{peak} = \frac{2P_o}{\pi\omega^2}$ where P_o, ω represent the total power and the beam waist, respectively at a certain distance [69]. The received power at the receiver, $P_{rcv} = Intensity \times A_{rec}$ where A_{rec} is the area of the receiver aperture. It is quite common to utilize the scanning mirror as the transmitter and receiver aperture to ensure a wide scanning angle as well as a wide field of view receiving capability. As a result, the relative size between the transmit beam diameter (D_T) and the scanning mirror diameter (D_S) plays an important role in optimizing the far-field beam profile, beam size, scanning resolution, and peak intensity. Furthermore, the ratio, $M_R = D_T / D_S$ needs to be optimized considering the tradeoffs among divergence, scattering, and beam clipping at the mirror aperture.

The collimated laser beam can be optimized to under-fill (M_R <100%) or over-fill (M_R ≥100%)

the scanning mirror. It is seen from Figure 4.10 that an overfilled Gaussian beam can exhibit less divergence and therefore, smaller beam size at the target. We estimate that the far-field beam radius decreases from 110 m to 20 m approximately for a 5.5 mm beam as M_R increases from 20% to 90%. Beam size in Figure 4.10 is measured as $1/e^2$ radius at a 100 km distance. However, when the beam size is comparable to mirror size it experiences higher beam profile distortion due to the scattering and diffraction phenomena. Additionally, it can be seen that the peak irradiance also increases up to a certain M_R and reaches a maximum when $80\% \leq M_R \leq 90\%$ as shown in the figure. Figure 4.10 is created considering a 0^o scanning angle of the SM. The dependence of the peak irradiance on the mirror's instantaneous scanning angle is discussed in the following section. Three commercially available compact scanning mirrors (15 mm, 10 mm, and 5.5 mm[43], [56]) are placed in the place of SM as shown in Figure 4.5 in the beam radius and irradiance simulation as shown in Figure 4.10. Moreover, the beam divergence data is incorporated from Table 4.2.

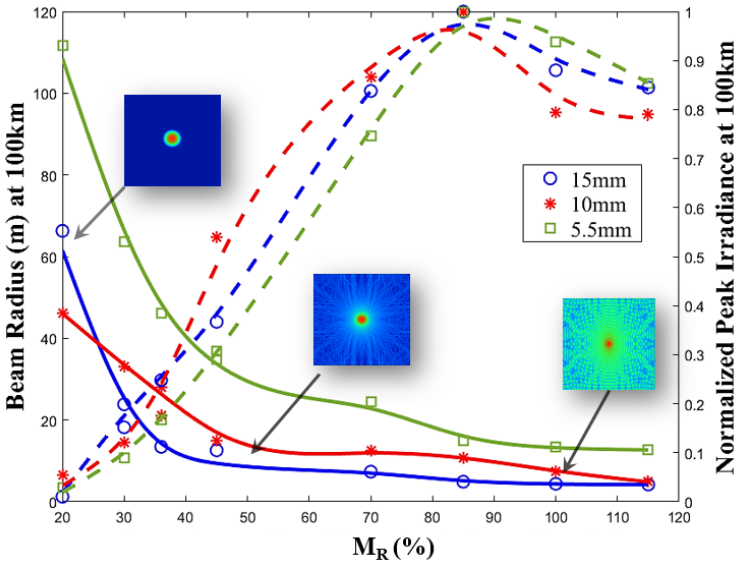

Figure 4.10. Effect of M_R on the beam size (solid curves) and peak irradiance (dashed curves) at 100 km. Three fast mirrors (15 mm, 10 mm, and 5.5 mm) are used in the Zemax simulation [18].

4.3.2 Beam Optimization Considering Scanning Angle

To enable omnidirectional CubeSat optical crosslink, a large scanning angle (greater than 10^o)

is desirable in a small form factor as shown in Figure 4.2 and Figure 4.5. However, when the beam size and the mirror size are comparable, the mirror scanning angle affects the intensity profile at the far-field and therefore causes scanning angle-dependent received power variation. The effect of the mirror's instantaneous angle on the far-field beam profile must be analyzed in detail to optimize the transmitter design for the transmitter of a CubeSat. As a proof of concept, peak irradiance variation due to different scanning angles at a 100 km distance for different initial beam sizes is presented in Figure 4.11. Here, we assume that the initial laser peak power is 1 W and the scanning mirror is mounted at 45^o w.r.t the optical path as shown in Figure 4.11 (inset).

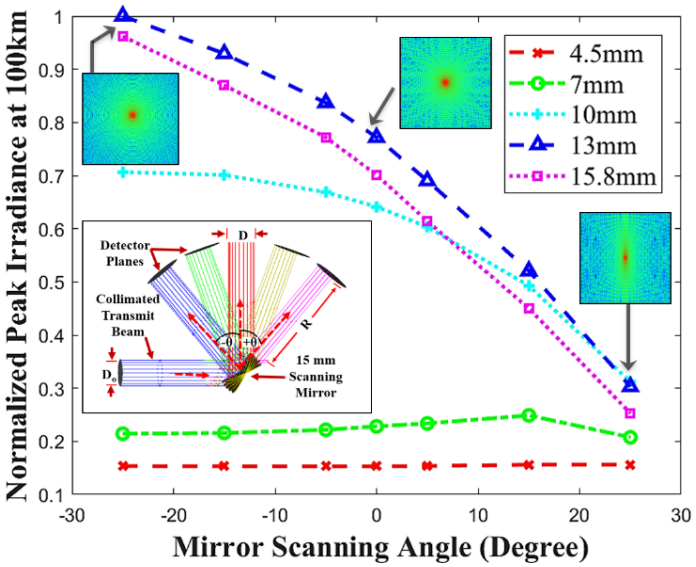

Figure 4.11. Effect of the mirror's instantaneous angle on the peak irradiance [18].

A 15 mm mirror with a large scanning range ($\pm 25^o$ mechanical scanning) is considered for this analysis. The vertical axis is the peak irradiance normalized with respect to the peak irradiance of a 13 mm transmitter beam as it shows the maximum peak irradiance at the far-field. It can be observed from Figure 4.11 that the peak intensity varies noticeably if the laser beam diameter ($1/e^2$) is greater than 30% of the diameter of the scanning mirror. For example, at a large scanning angle, the peak-irradiance can drop to about 10% and about 70% for a 7 mm and 13 mm laser beam, respectively as

shown in Figure 4.11.

Moreover, it can be seen from Figure 4.10 (insets) that the intensity profile gets distorted from the ideal profile (Gaussian profile) based on ratio, M_R. A relatively large beam (w.r.t. mirror diameter) manifests high peak intensity due to low divergence, nevertheless, the beam shape distortion is higher for a larger beam. Moreover, the far-field beam intensity profile also varies with the scanning mirror's instantaneous scanning angle due to the beam clipping and the scattering phenomena. For example, the beam profile variation in the far-field (100 km away from the transmitter) for a 13 mm initial beam size and different scanning angles is shown in Figure 4.11(insets). As a result, the transmit beam size for CubeSat for a given scanning mirror should be optimized considering the interplay between the divergence and the diffraction of the transmitter beam.

4.3.3 Beam Optimization Considering Pointing Challenges

The uncertainty of the satellite position leads to the challenges in the pointing accuracy that must be considered in the designing of a CubeSat optical transmitter. The transmitted laser beam width needs to be optimized considering the position uncertainty and the imperfect knowledge of the CubeSat orientation[71], [72]. At a fixed scanning angle, due to the Gaussian beam profile of the transmitted beam, error-free data communication is possible only if the receiver falls into a small region of the beam where the beam intensity is high enough to maintain desired SNR. Two figures of merit, Effective Communication Beam Region (ECBR) and Effective Communication Beam Width (ECBW) are introduced to quantify the initial beam size optimization technique considering pointing and tracking challenges inherited by optical communication. The Effective Communication Beam Region (ECBR) can be defined as the approximate circular area in the 2D space of the transmitted beam at a target within which a receiving CubeSat can maintain a desired SNR e.g. greater than 10 dB. The ECBW is the diameter of this ECBR. Once the pointing and acquisition are completed with the state-of-the-art methods (as suggested in [14], [66], [72]), ECBR and ECBW can be used to quantify

the immunity of the communication link from the random angular disturbance. The pointing of the transmitted beam needs to be just accurate so that the receiving CubeSat lies inside the ECBR. A system designed to have a large ECBR relaxes the pointing and tracking challenges compared to the system that possesses a small ECBR. Therefore, a larger ECBR manifests higher robustness to random CubeSat vibrations and position uncertainties. Considering Gaussian beam profile, the received optical power at the receiver varies as $P_{rcv}(d,R) = I(d,R) \times A_{rec}$ where $I(d,R) = \frac{2P_R}{\pi[r(R)]^2}\exp\left(\frac{-2d^2}{[r(R)]^2}\right)$, d, R, $r(R)$, P_R are the intensity distribution in the 2D plane, receiver position from the transmit beam center, communication distance, beam radius ($1/e^2$) at distance R (as in Section 4.3.1), and total optical power at the receiver plane, respectively [69]. $A_{rec} \approx \pi R_a^2$ is the area of the circular aperture lens and R_a is the radius of the aperture. Under the assumption of negligible power loss in the space one can assume that $P_R \approx P_T$,. The data communication link is effective if the received power is greater than or equal to the required power, $P_{rcv}(d,R) \geq P_{req}$. The required average optical power, $P_{req} \geq \sqrt{(SNR_{req} \cdot \sigma^2)/(R_p^2 \cdot M^2)}$, here, SNR_{req}, σ^2, M, R_p refer to the required SNR, total noise power, the APD gain, and the photodiode responsivity, respectively. ECBW is defined as, $P_{rcv}\left(\frac{ECBW}{2}, R\right) = P_{req}$. Given the above-mentioned conditions, the ECBW can be expressed as follows [18]

$$ECBW = \sqrt{2\, r(R)^2 \cdot ln\left(\frac{2\, P_T\, R_a^2}{P_{req}\, r(R)^2}\right)} \qquad (4.9)$$

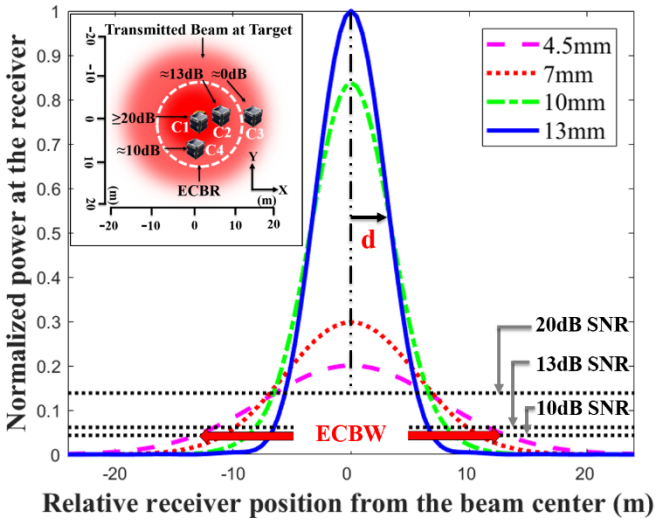

Figure 4.12. Effect of the relative receiver position from the transmit beam center on normalized received power.

In the free-space optical communication link, the ECBW is very effective as it is directly related to SNR and therefore, the data rate of the communication link. CubeSats C1, C2, and C4 in Figure 4.12(inset) can achieve SNR≥10 dB because they fall inside the ECBR. However, data communication cannot be established with C3 due to the low SNR. The Zemax beam propagation simulation of the received power by a 15 mm receiver lens for different positions (relative to the transmit beam center) of the receiving CubeSats at a 100 km distance is shown in Figure 4.12. Four different initial beam sizes (4.5 mm, 7 mm, 10 mm, and 13 mm) and three normalized SNR levels are considered for the illustration. All powers in Figure 4.12 are normalized to the received power of a 13 mm transmit beam. It can be observed that the ECBW for 13 mm, 10 mm, 7 mm, and 4.5 mm are about 14 m, 17.3 m, 22 m, and 26.29 m, respectively. Due to the small receiving aperture (15 mm) and high divergence, a high peak transmit power (about 10 W) is required to achieve an acceptable SNR at a long distance (e.g. 100 km) for a relatively smaller transmit beam size e.g. 4.5 mm and 7 mm. Therefore, for the sake of comparative analysis and visualization, we assume a 10 W peak transmit power in Figure 4.12. Given a laser with average power P_{AVG}, infinite extinction ratio, and duty cycle D, the theoretical

attainable peak power (P_{peak}) of a laser can be estimated as, $P_{peak} > P_{AVG}/D$. For instance, a laser operating at a 5% duty cycle and a 0.5 W average power can generate pulses with more than 10 W peak power. Up to date, several laser technologies have been demonstrated and they can provide several Watts to kilo Watts of peak power [66]–[68], [73]. Therefore, a 10 W peak power is indeed achievable by optimizing the laser modalities and the extinction ratio of the incorporated COTS lasers and amplifiers. Figure 4.13 summarizes the simulation results of the free space optical link to estimate ECBW for different initial beam sizes and powers over various distances. In short distance communication (less than 10 km), the ECBW for all transmit beam sizes are close to each other (in the range of 2 m to 6 m) for any transmitted beam size due to the negligible effect of the divergence. However, the effect of the initial beam size is notable in long-distance communication (beyond 50 km). For example, given that the initial peak power 10 W, at a 50 km communication distance the ECBW is measured as 18 m, 11.5 m, and 7.6 m for 4.5 mm, 10 mm, and 13 mm transmitted beam, respectively. It can be observed the ECBW of 4.5 mm beam gradually goes to zero as communication distance increases due to the lack of power to maintain a 10 dB SNR link.

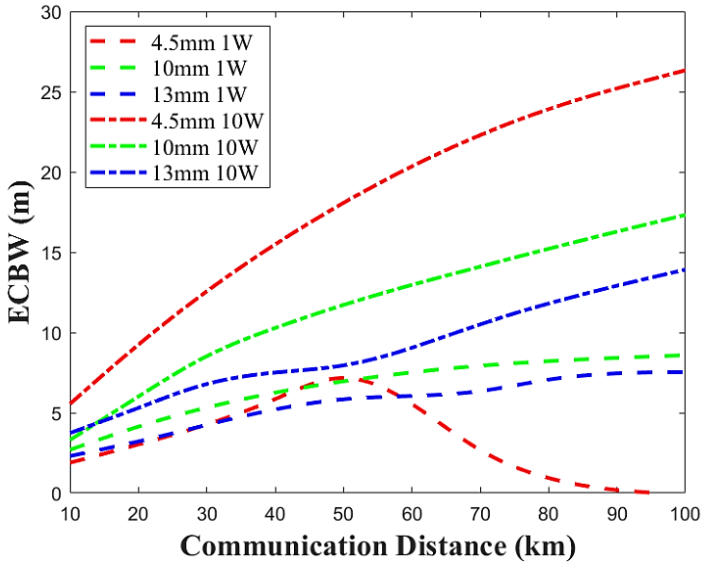

Figure 4.13. Effect of transmitter peak power on ECBW at different communication distances.

Furthermore, it can also be seen from Figure 4.13 that the effect of transmitter beam size on

ECBW is more prominent if the laser peak power is increased (a commonly adopted technique[33]) to achieve long-distance communication. For instance, at a 100 km communication distance, a 10 mm transmit beam manifests ECBW of 8.58 m and 17.3 m for 1 W and 10 W peak power respectively. Although the results presented here are the Zemax simulation results for higher accuracy, the presented (4.9) can be used to get a closer estimation of ECBW.

4.3.4 Feasibility Study of the Pointing Accuracy

From the sample ECBW calculation described in the previous section, the estimated required pointing accuracies at 100 km communication distance are less than 0.004^o, 0.005^o, 0.006^o, and 0.0075^o for 13 mm, 10 mm, 7 mm, and 4.5 mm transmit beam diameters, respectively. Recent advances in star tracking technologies, as well as scanning mirror technologies, demonstrate a higher pointing accuracy than the required pointing accuracy. For instance, an advanced star tracker demonstrates a pointing accuracy of $\pm 0.003^o$ [16]. Recent advances in MEMS scanning mirrors (e.g. Mirrorcle [56]) reveal mirror actuators of greater than 14 bits (16384 positions) on each axis. Therefore, the MEMS mirrors with a mechanical tilt range of -7° to +7° on each axis present a tilt resolution less than 0.0008^o (or smaller than 14 μrad) on both axes. The dual axis vector mirror (e.g. Optotune [43]) with $\pm 25^o$ mechanical scanning capability claims to possess a closed loop resolution less than $5\ \mu rad$. In the type B transceiver design, alongside the star tracker of the host satellite, each transceiver is equipped with a high-speed camera based coarse Angle of Arrival (AOA) detection system as shown in Figure 4.2. In addition, the Quad Detector (QD) as shown in Figure 4.5 facilitate the fine pointing and tracking mechanism for the Scanning Mirror. We believe that the pointing accuracy requirement can be addressed by a closed loop Pointing, Acquisition, and Tracking (PAT) system incorporating the advanced attitude control system, host Attitude Determination, and Control System (ADCS), scanning mirror technologies, transmitter beam broadening, and position detectors (e.g. quadrant detectors) [14], [17], [66]. Fitting all the components of the omnidirectional

transceiver in 1U is convenient but not mandatory for every application. Detail implementation techniques are subjective and can be accomplished in many ways based on the applications.

In the design analysis, we opt for 850 nm as the operating wavelength to achieve less divergence, as well as the availability of low-cost Si APDs, high power lasers (e.g. VCSELs, semiconductor lasers), and COTS optics. All analyses are scalable to other wavelengths, such as conventional telecom wavelengths near 1550 nm with compatible component parameters. Most components are already available in space-grade. With increasing demand, new components such as high-speed MEMS mirrors are being tested for space applications. Transmitter beam size optimization techniques possess the tradeoff among maximum achievable received power, host satellite vibration, and pointing precision requirement, the space-power limitations, component availability as well as the interplay between the beam divergence and scattering for a given distance.

This chapter presents a systematic TX optical design optimization rule considering all the design variables mentioned above to pave the way to omnidirectional CubeSat crosslink based advanced applications.

Chapter 5

Receiver Architecture Design in the Presence of Pointing Jitter

One of the major challenges of an Inter Satellite Optical Link (ISOL) is the necessity of the complex pointing, acquisition, and tracking (PAT) system. A well-engineered PAT mechanism is crucial in achieving maximum connectivity in a constellation where every satellite expects to sustain multiple data communication links simultaneously as shown in Figure 5.1 [4], [54].

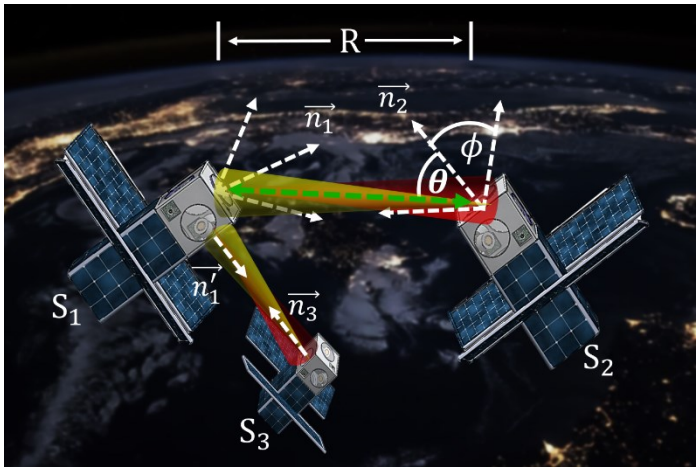

Figure 5.1. Free space optical communication in a satellite constellation [13].

In this chapter, I present a complete analytical model that incorporates both the receiver architecture parameters and the statistical distribution of the pointing errors. In particular, a mathematical performance model of a direct detection optical receiver is derived to analyze the effect of receiver design parameters on the link immunity to the pointing jitters. The presented analytical model includes key receiver design parameters, such as detector radius, receiver aperture size, F-number of the focusing lens system, the beam compression ratio of the telescope, the aberration parameter, etc. Both instantaneous and average link performances are analyzed and presented using the derived model. As a case study, a CubeSat direct detection optical receiver is being studied. It is shown that by optimizing the beam compression ratio and minimizing the optical aberrations of the telescope more than three orders of magnitude BER improvement can be realized in a given ISOL. Moreover, this study indicates that six orders of magnitude BER improvement are realizable for a

given ISOL by designing a receiver system with optimal selection of telescope beam compression ratio, F-number of the focusing system, and aberration parameter. Hence, the presented study facilitates the selection of the optimum design parameters for the best performance in the presence of random pointing errors.

5.1 Statistical Model of Pointing Jitters and the Effect of Receiver Architecture on Performance

5.1.1 Model of Pointing Jitters and Receiver Architecture

The pointing errors depend on the electrical noises in the PAT sensors and the mechanical vibrations that couple to optical subsystems. The fundamental expression of the tracking sensor noise $\sigma_{\theta S}$ (standard deviation) has been studied before, and it has been expressed in terms of slope factor of the transfer function ζ which is a function of the signal to noise ratio $\frac{S}{N}$ of the system, $\sigma_{\theta S} = \frac{1}{\sqrt{\zeta(S/N)}}$ [74]. Mechanical vibrations cause to pointing error $\sigma_{\theta M}$ that can be modeled as $\sigma_{\theta M}^2 = \frac{1}{2\pi}\int S_\theta(\omega)|1 - H_T(\omega)|^2\, d\omega$ where $S_\theta(\omega)$ is the power spectral density of the mechanical noise and $H_T(\omega)$ is the closed loop transfer function of the spatial tracking loop [75]. The combined effect of the electrical noise in PAT sensors and mechanical vibrations creates elevation and azimuth pointing angle errors. The Probability Density Function (PDF) of both the elevation pointing error θ_{ET} and azimuth pointing error θ_{AT} has been modeled as normal distribution as $p(\theta_{ET}) = \frac{1}{\sqrt{2\pi\sigma_E^2}}\exp\left(-\frac{\theta_{ET}^2}{2\sigma_E^2}\right)$ and $p(\theta_{AT}) = \frac{1}{\sqrt{2\pi\sigma_A^2}}\exp\left(-\frac{\theta_{AT}^2}{2\sigma_A^2}\right)$, respectively [15], [24]. Here, σ_E^2 and σ_A^2 represent the variance of the elevation and the azimuth pointing error, respectively. Assuming the distribution of θ_{ET} and θ_{AT} are independent, but alike, the PDF of the radial pointing error θ_T ($\theta_T^2 = \theta_{ET}^2 + \theta_{AT}^2$) is a Rayleigh distribution that can be expressed in terms of the variance of the radial pointing error σ_T^2, $p(\theta_T) = \frac{\theta_T}{\sigma_T^2}\exp(-\frac{\theta_T^2}{2\sigma_T^2})$. Due to the radial symmetry, one can assume $\sigma_T = \sigma_A = \sigma_E$ [22]. The pointing jitters can affect the communication performance, especially at a large Angle of Incidence (AOI) θ as shown

in Figure 5.1. The initial communication link between the transmitter and the receiver is usually established with the help of Ephemerides data and the advanced PAT system [76]. The transmitter and receiver usually achieve a mutual line of sight tracking of each other by body pointing, coarse pointing, and fine pointing mechanisms [17], [77]. However, due to the uncertainty of the satellite positions and the limited resolution of the PAT systems, θ can be significantly large between certain satellites in a constellation. For instance, in Figure 5.1, a large AOI θ exists between S_1 and S_2 as the transmit beam of S_1 creates a large angle with respect to the receiver normal $\overrightarrow{n_2}$. In contrast, a smaller θ exists between S_1 and S_3 since the transmit beam of S_1 aligns well with the receiver normal of S_3 ($\overrightarrow{n_3}$). For effective long-distance data communication, the AOI needs to be smaller than the receiver's Field of View (FOV) ϕ i.e. $\theta < \phi$. The instantaneous AOI at the receiver optical aperture can be written as, $\theta_i = \theta + \theta_T$. For a given θ, the instantaneous received optical power by the receiver aperture $P_{rcv}(\theta_T)$ can be estimated from Friis transmission equation [35],

$$P_{rcv}(\theta_T) = P_T G_T G_R \alpha_T \alpha_R L_p \left(\frac{\lambda}{4\pi R}\right)^2 L_{PJ}(\theta_T) \qquad (5.1)$$

Here, $P_T, G_T, G_R, L_P, \lambda, R, \alpha_T, and\ \alpha_R$ represent average transmit power, transmit antenna gain, receiver antenna gain, pointing loss, operating wavelength, communication range, transmitter feeder loss, and receiver plumbing loss, respectively. The loss due to random pointing jitter $L_{PJ}(\theta_T)$ can be given by [11], $L_{PJ}(\theta_T) = \exp(-G_T\theta_T^2)$. Assuming θ varies much slower than the pointing jitter θ_T, the loss related to θ is lumped into the pointing loss L_p in the above-mentioned Eq. (5.1). Hence, the instantaneous signal photocurrent $i_{PD}(\theta, \theta_T, \mathbb{S})$ depends on the receiver architecture that can be expressed in terms of the responsivity of the detector R_λ, the intrinsic gain of the photodetector G, and the performance degradation factor $K(\theta, \theta_T, \mathbb{S})$. Here, the performance degradation factor is determined by a set of receiver design parameters $\mathbb{S}$ ={aperture size, detector size, lens focal length, etc.}.

$$i_{PD}(\theta, \theta_T, \mathbb{S}) = R_\lambda G P_{rcv}(\theta_T) \cdot K(\theta, \theta_T, \mathbb{S}) \tag{5.2}$$

The major causes of the performance degradation factor are random beam walk-off at the detector plane $\eta_{BO}(\theta, \theta_T, \mathbb{S})$, angle-dependent detector responsivity $\eta_\lambda(\theta, \theta_T)$, reflection due to Anti-Reflection (AR) coating $\eta_{AR}(\theta, \theta_T)$, and free space to Focusing Lens (FL) coupling efficiency $\eta_C(\mathbb{A})(A \subset \mathbb{S})$. Hence, the performance degradation factor can be expressed as

$$K(\theta, \theta_T, \mathbb{S}) = \eta_{BO}(\theta, \theta_T, \mathbb{S})\eta_{AR}(\theta, \theta_T)\, \eta_\lambda(\theta, \theta_T)\eta_C(\mathbb{A}) \tag{5.3}$$

In a high-speed free-space communication system, due to the wave-front error of the received beam and the aberrations in the optical system, the focal spot size of the received beam is usually comparable to the active area of the high-speed detectors. Hence, in the presence of pointing jitter, the random beam walk-off at the detector plane becomes a dominant degradation factor. The performance degradation factor in the free space direct detection system can therefore be simplified and written as $K(\theta, \theta_T, \mathbb{S}) \approx \eta_{BO}(\theta, \theta_T, \mathbb{S})\eta_C(\mathbb{A})$. Assuming the photodetector's radius r_d is close to but larger than the focal spot radius r_f i.e. $r_d > r_f(d_B, f, \xi)$, the radial displacement of the focal spot center from the detector center $\rho(\kappa\theta, \kappa\theta_T)$, angle magnification factor of the receiver telescope κ, and $\theta < \phi$, the $K(\theta, \theta_T, \mathbb{S})$ can be approximated as [13]

$$\begin{aligned} K(\theta, \theta_T, \mathbb{S}) \approx \frac{0.318\eta_C(\mathbb{A})}{r_f(d_B, f, \xi)^2}\Bigg(& r_f(d_B, f, \xi)^2 \cos^{-1}\frac{\gamma_2}{r_f} + r_d^2 \cos^{-1}\frac{\gamma_1}{r_d} - \gamma_1\sqrt{r_d^2 - \gamma_1^2} \\ & - \gamma_2\sqrt{r_f(d_B, f, \xi)^2 - \gamma_2^2}\Bigg) \end{aligned} \tag{5.4}$$

$$\approx \eta_C(\mathbb{A})\ if\ \rho(\kappa\theta, \kappa\theta_T) < r_d - r_f$$

$$\approx 0\ if\ \rho(\kappa\theta, \kappa\theta_T) > r_d + r_f$$

$$\gamma_1 = \frac{r_d^2 - r_f(d_B, f, \xi)^2 + \rho(\kappa\theta, \kappa\theta_T)^2}{2\rho(\kappa\theta, \kappa\theta_T)}$$

$$\gamma_2 = \frac{r_f(d_B, f, \xi)^2 - r_d^2 + \rho(\kappa\theta, \kappa\theta_T)^2}{2\rho(\kappa\theta, \kappa\theta_T)}$$

The focal spot radius $r_f(d_B, f, \xi)$ can be approximated from the beam diameter d_B, the beam mode quality M, and the focal length of the focusing lens (FL) f and is given by $r_f(d_B, f, \xi) \approx 0.64M^2\lambda\frac{f}{d_B} + \xi\left(\frac{d_B^3}{2f^2}\right)$. The aberration factor b of the lens system depends on the materials of optical lenses, the curvature of the lens surfaces, and the receiver lens system design. A detailed Gaussian beam propagation simulation or experimental validation is required to approximate ξ for a given optical system. For instance, ξ of a singlet plano-convex lens made from N-BK7 glass can be estimated by detail optical simulations (in Zemax) as, $\xi = 0.1943 + 0.00202d_B - 0.000798f$. In this model, the numerical values of d_B (in mm) and f (in mm) need to be used to estimate the unit-less parameter ξ. Assuming θ is well controlled by the PAT system over the considered time duration to analyze the impact of the pointing jitter, the average Signal to Noise Ratio (SNR) SNR_{avg} can be estimated from the instantaneous received power, the instantaneous noise power $\sigma_N^2(\theta, \theta_T)$, and σ_T as

$$SNR_{avg} = R_\lambda^2 G^2 \int_0^\infty \frac{p_{rcv}(\theta_T)^2 K(\theta, \theta_T, \mathbb{S})^2}{\sigma_N^2(\theta, \theta_T)} \cdot \frac{\theta_T}{\sigma_T^2} \exp\left(-\frac{\theta_T^2}{2\sigma_T^2}\right) d\theta_T \qquad (5.5)$$

Considering a communication system that receives a pulsed light with a duty cycle D and an extinction ratio r_{ex} in a direct detection method, the instantaneous signal current for bits 1 can be expressed as $i_{PD-1}(\theta, \theta_T, \mathbb{S}) = \gamma i_{PD}(\theta, \theta_T, \mathbb{S})$. Similarly, the instantaneous signal current for bits 0 is given as $i_{PD-0}(\theta, \theta_T, \mathbb{S}) = \gamma r_{ex} i_{PD}(\theta, \theta_T, \mathbb{S})$. Here, $\gamma = \frac{1}{D(1-r_{ex})+r_{ex}}$. The instantaneous noise variances σ_{N-1}^2 (for 1) and σ_{N-0}^2 (for 0) is a function of signal currents, receiver dark current I_d, excess noise factor F_A, and the thermal noise σ_{TH}^2. The noise variances can be expressed as

$$\begin{aligned} \sigma_{N-1}^2(\theta, \theta_T, \mathbb{S}) &= 2qF_A(i_{PD-1}(\theta, \theta_T, \mathbb{S}) + G^2 I_d)\Delta\upsilon + \sigma_{TH}^2 \\ \sigma_{N-0}^2(\theta, \theta_T, \mathbb{S}) &= 2qF_A(i_{PD-0}(\theta, \theta_T, \mathbb{S}) + G^2 I_d)\Delta\upsilon + \sigma_{TH}^2 \end{aligned} \qquad (5.6)$$

Here, q is the elementary charge. Consequently, the instantaneous Gaussian-Q function can be

written as $Q(\theta, \theta_T, \mathbb{S}) = \frac{i_{PD-1}(\theta,\theta_T,\mathbb{S}) - i_{PD-0}(\theta,\theta_T,\mathbb{S})}{\sigma_{N-1}(\theta,\theta_T,\mathbb{S}) + \sigma_{N-0}(\theta,\theta_T,\mathbb{S})}$ [55]. Therefore, for a given θ and $\mathbb{S}$, the instantaneous error probability can be calculated from $Q(\theta, \theta_T, \mathbb{S})$

$$p_e(\theta_T) \approx \frac{1}{2} erfc\left(\frac{Q(\theta, \theta_T, \mathbb{S})}{\sqrt{2}}\right) \tag{5.7}$$

Finally, the system BER can be obtained by averaging the instantaneous Bit Error Probability (BEP) $p_e(\theta_T)$, and can be written as

$$BER = \int_0^\infty p_e(\theta_T) p(\theta_T) d\theta_T \tag{5.8}$$

5.1.2 Model of a Sample Direct Detection Receiver

The general formulation presented in the previous section can be modified according to a specific receiver architecture. As an illustration, here, we present the performance estimation model of a sample direct detection receiver in a small satellite platform as shown in Figure 5.2 (reprinted with permission from [13]© The Optical Society.).

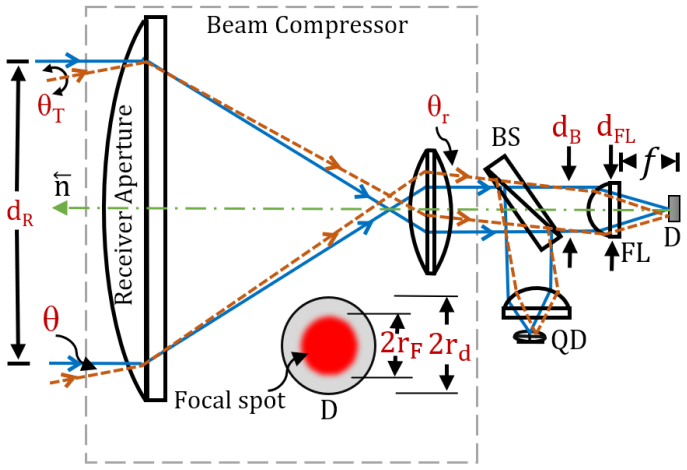

Figure 5.2. Sample direct detection optical receiver.

The sample receiver has a clear aperture diameter of d_R and the telescope beam compressor reduces the beam diameter to d_B. In long-distance communication, one can assume a plane wave

illuminates the entire receiver aperture. Therefore, the beam compression ratio m_T can be defined as $m_T^{-1} = \frac{d_B}{d_R}$ and $\kappa \approx m_T$ in Eq. (5.4). The detector diameter and the focal spot diameter are denoted as $2r_d$ and $2r_F$, respectively. A Beam Sampler (BS) is usually used to sample a fraction beam for the Quadrant Detector (QD) to facilitate the pointing and tracking mechanisms [34]. In Figure 5.2, the on-axis received beam is shown as a solid blue line and the off-axis received beam is shown as a dashed-orange line. All angles are measured w.r.t. the direction normal to the receiver $\vec{n}$. Besides, θ_T is the instantaneous pointing error and θ_r is the instantaneous total angular variation of the compressed beam. θ_r can be expressed as $\theta_r = m_T(\theta + \theta_T)$. Finally, a Focusing Lens (FL) of diameter d_{FL} focuses the beam on the detector (D). To simplify the model, we lump the impact of optical aberration in ξ. Hence, the coupling efficiency is approximated as $\eta_C(\mathbb{A}) = \left(\frac{m_T d_{FL}}{d_R}\right)^2$ if $m_T d_{FL} \leq d_R$, otherwise $\eta_C \approx 1.0$. $\mathbb{A} = \{m_T,\ d_R, d_{FL}\}$. The radial displacement of the center of the focal spot from the center of the detector can be expressed as $\rho(\kappa\theta, \kappa\theta_T) \approx f m_T(\theta + \theta_T)$. Under small-angle approximation, the instantaneous performance degradation factor of the sample receiver architecture $K_s(\theta, \theta_T, \mathbb{S})$ is derived from Eq. (5.4), and is given by [13]

$$
\begin{aligned}
K_s(\theta, \theta_T, \mathbb{S}) \approx{}& \frac{\eta_C(\mathbb{A})}{\pi} \sec^{-1}\left(\frac{2fr_f m_T(\theta+\theta_T)}{-r_d^2+r_f^2+f^2m_T^2(\theta+\theta_T)^2}\right) + \\
& \frac{\eta_C(\mathbb{A})}{\pi}\left(\frac{r_d}{r_f}\right)^2 \sec^{-1}\left(\frac{2fr_d m_T(\theta+\theta_T)}{r_d^2-r_f^2+f^2m_T^2(\theta+\theta_T)^2}\right) - \frac{\theta_r f \eta_C(\mathbb{A})}{\pi r_f^2}\left[r_d^2 - \frac{\left(r_d^2-r_f^2+f^2m_T^2(\theta+\theta_T)^2\right)^2}{4f^2m_T^2(\theta+\theta_T)^2}\right]^{0.5} \\
={}& \eta_C(\mathbb{A}) \text{ if } f m_T(\theta+\theta_T) < r_d - r_f \\
={}& 0 \text{ if } f m_T(\theta+\theta_T) > r_d + r_f
\end{aligned}
\tag{5.9}
$$

Equation (5.9) reveals the effect of receiver design parameters, $\mathbb{S} = \{m_T, r_d, d_R, f, d_{FL}, \xi\}$ on the degradation factor. Depending on the random pointing jitter and the receiver parameters, K_s can vary between 0.0 and 1.0, $0 \leq K_s(\theta, \theta_T, \mathbb{S}) \leq 1$. Once we estimate the received power on the detector, the instantaneous BEP and the BER of the sample receiver can be calculated using Eqs. (5.7)

and (5.8), respectively. Generally, in a receiver design $d_{FL} \geq d_B$ and therefore, we can assume $\eta_C(\mathbb{A}) \approx 1.0$. Additionally, assuming a Gaussian beam with $M^2 \approx 1.0$ and the incorporated FL has an F-number of N, the performance degradation factor expression in Eq. (5.9) can be simplified further and given as [13]

$$
\begin{aligned}
&K_s(\theta_T, r_d, d_R, N, m_T, \xi, \tau) \\
&\quad \approx \frac{1}{\pi}\sec^{-1}\left(\frac{2ABNd_R}{B^2 + A^2N^2d_R^2 - r_d^2}\right) \\
&\quad + \frac{r_d^2}{B^2\pi}\sec^{-1}\left(\frac{2ANd_Rr_d}{-B^2 + A^2N^2d_R^2 + r_d^2}\right) \\
&\quad - \frac{1}{B^2\pi}ANd_R\left[r_d^2 - \frac{\left(-B^2 + A^2N^2d_R^2 + r_d^2\right)^2}{4A^2N^2d_R^2}\right]^{0.5} \\
&\approx 1 \text{ if } N\left(\frac{\tau r_d}{N} + d_R\theta_T\right) < r_d - B \\
&\approx 0 \text{ if } N\left(\frac{\tau r_d}{N} + d_R\theta_T\right) > r_d + B \\
&A = \theta_T + \frac{\tau r_d}{d_R N} \text{ and } B = 0.64N\lambda + \frac{d_R\xi}{2m_TN^2}
\end{aligned}
\tag{5.10}
$$

Here, τ is the ratio of the AOI to the receiver's field of view i.e. $\tau = \frac{\theta}{\phi}$. The beam compression ratio m_T of the sample receiver architecture as shown in Figure 5.2 is limited by the diffraction-limit focus spot size of the aperture lens and the manufacturable optics. The diffraction-limited spot size (airy disc radius) after the aperture lens can be calculated from the focal length of the aperture lens f_R, and can be given as $r_a = \frac{0.64M^2\lambda f_R}{d_R}$. Hence, the realizable compression ratio of the sample telescope can be expressed as $m_T \ll \frac{d_R^2}{1.28M^2\lambda f_R}$.

5.2 Performance Analysis and Simulation Results

The link parameters and the receiver design parameters are summarized in Table 5.1.

Table 5.1 Parameters of the major transceiver components.

Parameters	Symbol	Value
Modulation format		OOK
Communication distance	R	100.0 km
Transmit power	P_T	1.0 W
Wavelength	λ	1550 nm
Transmitter feeder loss	α_T	2.0 dB
Receiver plumbing loss	α_R	2.0 dB
Link pointing loss	L_P	3.0 dB
Communication bandwidth	$\Delta\upsilon$	1.0 GHz
APD gain	G	50
APD responsivity	R_λ	0.8
APD noise equivalent power	NEP	30.0 $pW/\sqrt{Hz}$
Average dark current	I_d	15.0 nA
Excess noise factor	F_A	2.0
Detector size (diameter)	$2r_d$	0.2-0.5 mm
Transmit beam size (diameter)	d_T	15.0 mm
Receiver aperture (diameter)	d_R	15.0 mm
Receiver power (w/o pointing error)	P_{rcv}	-35.77 dBm
BER (w/o pointing error)		$\approx 2 \times 10^{-11}$

The considered values for each parameter in this analysis are typically used in the state-of-the-art systems based on a literature survey and manufacturer specifications[11], [18], [48], [78]. Although the considered design parameters are pertinent to CubeSat omnidirectional optical link [18], [54], all analyses apply to any satellite optical link with the appropriate design and link parameters.

5.2.1 Instantaneous Performance Degradation Analyses

Eq. (5.10) reveals the dependence of the instantaneous performance degradation factor K_S on the detector size r_d, the receiver aperture size d_R, the N of the focusing lens, the beam compression ratio m_T , the ratio of the angle of incidence to the FOV τ, and the aggregated aberration factor ξ of the lens system. To demonstrate the instantaneous performance degradation, an omnidirectional

CubeSat platform [18] is chosen with a 15 mm receiver aperture i.e., $d_R = 15.0$ mm and the instantaneous pointing error, $\theta_T = 0.5\ \mu rad$. As $\theta_T \ll \tau\phi$, the effect of instantaneous θ_T is negligible on K_S. However, the distribution of θ_T significantly affect the average link performance as expected from Eqs. (5.5) and (5.8).

A sample analysis to demonstrate the dependence of K_S on τ and r_d (assuming $\xi = 0.15$) is presented in Figure 5.3(a) and (b) show the performance degradation for $N = 2.0$ and $N = 3.0$, respectively. It can be seen from Figure 5.3 (a) that K_S drops to 0.4 from 0.99 almost linearly within a range of $0 \leq \tau \leq 1$ for $r_d = 0.1\ mm$ and $m_T = 3.0$. On the contrary, for $r_d = 0.5$ mm and $m_T = 3.0$, K_S remains stable (close to 1.0) for $\tau \leq 0.81$. Hence, increasing r_d improves the receiver tolerance to τ for a given m_T, as expected. Further improvement of receivers' tolerance by increasing m_T is evident from Figure 5.3(a). Although the angular variation increases due to the beam compression i.e. $\theta_r \approx m_T\theta_i$, the impact of m_T can be counterbalanced by the focusing lens parameters. The resultant beam walk-off at the detector plane is found to be $\rho = \zeta\theta_i N d_R$ where $\zeta = \frac{d_{FL}}{d_B}$. Besides, in an aberration limited optical receiver, $r_f \propto d_B^3 \propto 1/m_T^3$. Therefore, for a given aperture size, a smaller m_T tends to create a larger focal spot. As a result, the probability of beam clipping at the detector increases due to lateral movement of focal spot that reduces the achievable average SNR in the presence of pointing jitter. For example, if a beam compressor with $m_T = 5.0$ is incorporated then K_S is close to 1.0 for $\tau \leq 0.43$ for $r_d = 0.1$ mm and K_S gradually decreases to 0.25 when τ approaches 1.0 as shown in Figure 5.3(a).

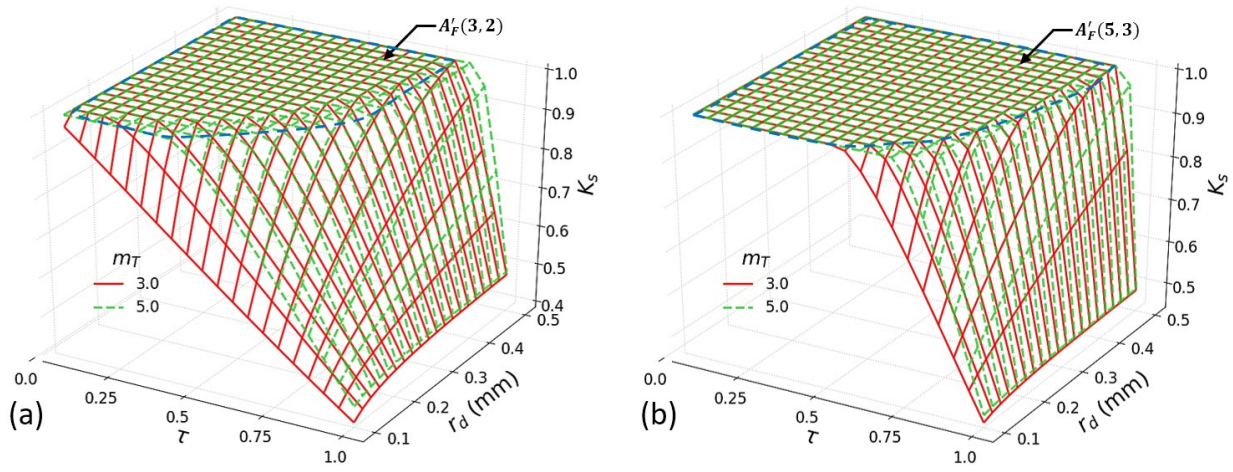

Figure 5.3. Effect of τ and r_d on K_S for m_T ={3, 4}. (a) N=2.0, (b) N=3.0 [13].

A higher N also helps to make the receiver system less sensitive to pointing errors. For instance, it can be seen from Figure 5.3(b) that for $m_T = 3.0$, $N = 3.0$, and $r_d = 0.1\ mm$, K_s remains close to 1.0 for $\tau \leq 0.57$ and then gradually drops to 0.45 when τ gradually approaches to 1.0. Visually, the sensitivity of K_S on the design parameters can be compared based on the area of the quasi-flat region (relatively constant K_S region) A_F' of the plots where $K_S \geq 0.98$. It can be qualitatively realized that $A_F'(3,2) < A_F'(5,2) < A_F'(3,3) < A_F'(5,3)$. Here, $A_F'(m_T, N)$ represents the area of the quasi-flat region of the plots for the given m_T and N as shown in Figure 5.3. A larger A_F' implies higher immunity to incident angle errors. Therefore, we can say that among the considered combination of design parameters, the receiver system with $m_T = 3.0$ and $N = 2.0$ has the lowest immunity to pointing jitters, whereas the system with $m_T = 5.0$ and $N = 3.0$ demonstrates the highest immunity.

The effect of τ and ξ on the instantaneous performance degradation for two different detector radiuses, $r_d = \{0.1mm, 0.25mm\}$ is presented in Figure 5.4. Figure 5.4(a) shows the impact of ξ and τ on K_S for $m_T = 3.0$ and $N = 3.0$. For instance, it can be seen from Figure 5.4(a) that at $\xi = 0.15$ and $r_d = 0.25\ mm$, the factor K_S is close to 1.0 for $\tau \leq 0.95$. In contrast, a 0.1 mm detector shows $K_S \geq 0.98$ for $\tau \leq 0.8$ at the same aberration, $\xi = 0.15$. It is also realizable from Figure 5.4(a) that K_S can vary from 1.0 to 0.4 over the range $0.2 < \tau \leq 1.0$ based on the receiver parameters r_d and ξ.

Evidently, a receiver with larger r_d is more immune to variation of τ and ξ. The instantaneous performance degradation can further be reduced by incorporating a beam compressor with a higher m_T as can be realized from Figure 5.4(b). As applied to Figure 5.3, similar visual analyses of the receivers' tolerance to τ and ξ based on the relatively constant K_S region is also applicable here. For example, it can be seen that $A_F(3,3) < A_F(3,5)$ for all detector sizes. Here, $A_F(N, m_T)$ represents the area of the flat (constant K_S) region. Hence, for a given N a system with a higher m_T demonstrates higher immunity to pointing errors due to vibrations.

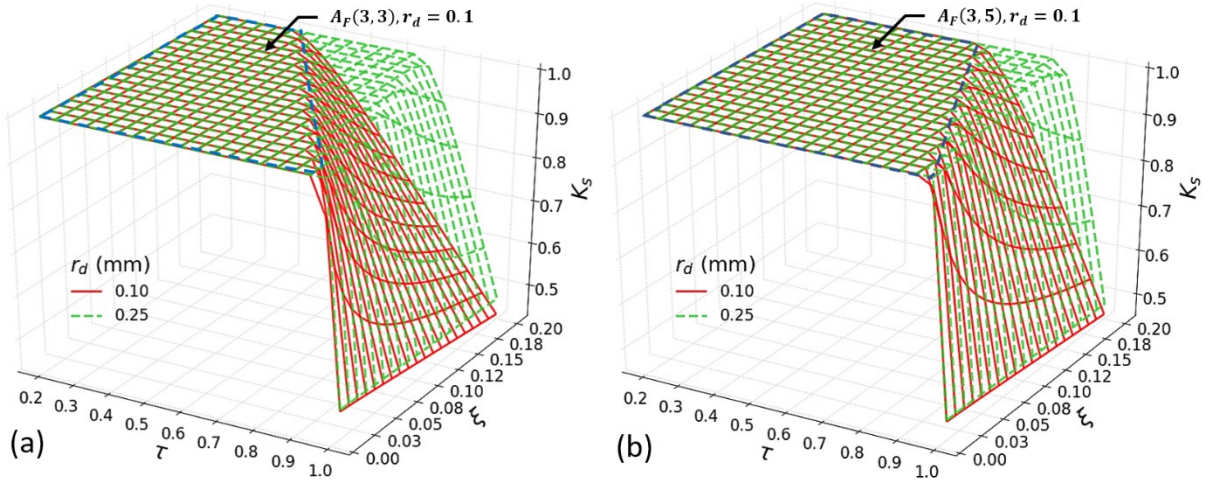

Figure 5.4. Impact of τ and r_d on K_S for $r_d = \{0.1mm, 0.25mm\}$. (a) $N = 3.0, m_T = 3.0$, (b) $N = 3.0, m_T = 5.0$ [13].

.

In this analysis, τ, the ratio between the incident angle and the FOV, is used to compare the performance of different design choices. The receivers' instantaneous FOV (half angle) can be calculated as $\phi \approx \frac{r_d}{N\xi d_R}$. Assuming $\xi = 1.0$, the estimated instantaneous ϕ of the receiver designed with the parameters given in Table 5.1 is given in Table 5.2.

Table 5.2 Receiver's instantaneous FOV (half angle).

$r_d\ (mm)$	N	$\phi\ (^o)$	$r_d\ (mm)$	N	$\phi\ (^o)$
0.1	2	0.2	0.1	3	0.13
0.25	2	0.48	0.25	3	0.32
0.5	2	0.95	0.5	3	0.64

5.2.2 Performance of the communication link

The communication link performance for a given aperture size can be characterized by, a) link limited (LL) performance and b) architecture limited (AL) performance. The LL performance is calculated from the link budget equation that is restrained by communication distance, transmit power, a limited receiver optical aperture, etc. The LL performance assumes an optimum receiver design. We calculate the link limited lowest achievable BER of the given link is to be around 10^{-10} in the absence of pointing jitters that is caused by satellite vibration. However, the performance degrades due to the unavoidable pointing jitters as given in Eqs. (5.5) and (5.8). The performance degradation depends on the architecture of the receiver and therefore, architecture-dependent link performance is achieved. The optical architecture of the receiver must be designed carefully to ensure the required BER for seamless data communication. The sample receiver performance of the satellite link in the presence of pointing jitters for different receiver design parameters is shown in Figure 5.5. As shown in Figure 5.5(a) and (b), considering random angular pointing jitters of $0.25\ \mu rad \leq \sigma_T \leq 0.75\ \mu rad$ and $\xi = 0.2$, the LL BER for the given link BER_{LL} is calculated as $10^{-10.7} \leq BER_{LL} \leq 10^{-8}$.

Figure 5.5 also shows that the achievable AL BER (calculated from (5.8)) varies notably depending on $r_d, m_T, N, and\ \tau$. Figure 5.5(a) presents the impact of pointing jitter on the achievable BER at $\tau = 0.5$. For instance, the achievable BER varies between about $10^{-7.5}\ and\ 10^{-5.6}$ when a 0.1 mm detector, a 5x beam compressor, and a focusing lens of $N = 2.0$ are incorporated in the sample receiver architecture (as shown in Figure 5.2). It can be realized that the AL performance can be

improved by implementing a receiver with a larger r_d, higher m_T, and larger N (limited by the lens design parameters and available volume).

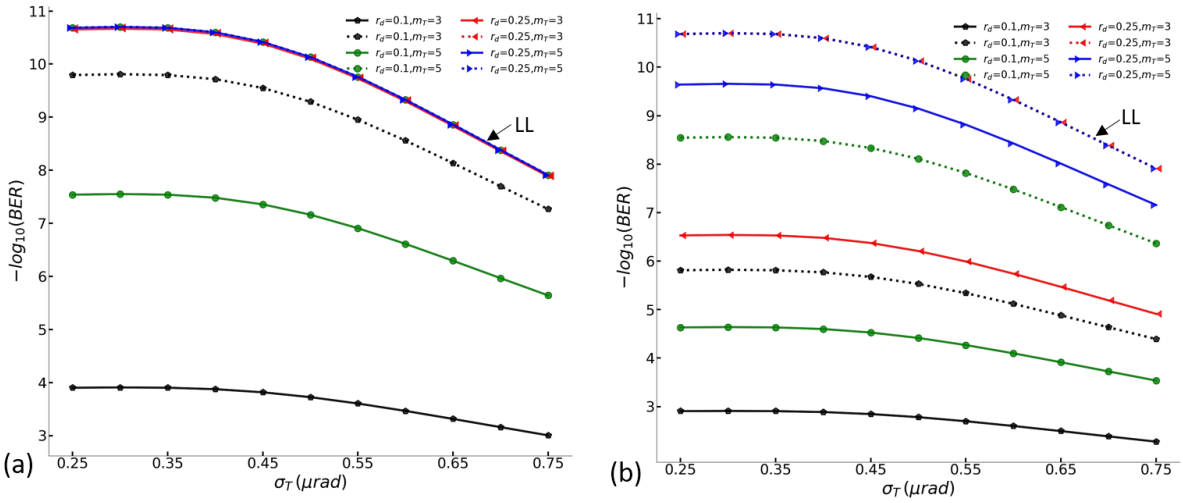

Figure 5.5. BER versus σ_T for different m_T and r_d. Solid curves correspond to N=2.0, whereas dashed curves correspond to N=3.0. a) $\tau = 0.5$, b) $\tau = 0.75$ [13].

The selection of r_d depends on the communication bandwidth, wavelength, and noise equivalent power (NEP). Frequently, these criteria will limit the options. The bandwidth (BW) of the detector is inversely proportional to the detector size, $BW \propto 1/r_d$. Also, in many detectors such as PIN photodiodes, $NEP \propto r_d$ [78], [79]. Even though the NEP of most PIN photodiodes increases with the size of the detectors, many communication detectors show the opposite behavior, especially APDs. For example, two commercially available InGaAs APDs with a diameter of 0.2 mm and 75μm have a NEP of 0.45 $pW/\sqrt{Hz}$ and 1.1 $pW/\sqrt{Hz}$, respectively [80]. Similarly, 1.0 mm, 0.5 mm, and 0.2 mm Si APDs show 2.5 $fW/\sqrt{Hz}$, 0.09 $pW/\sqrt{Hz}$, and 0.15 $pW/\sqrt{Hz}$, NEP respectively. As a result, the performance gap between 0.1 mm and 0.25 mm as shown in Figure 5.5 and Figure 5.6 may decrease or increase slightly based on the detector types and integrated bandwidth. We assume almost constant NEP for both detectors and the integrated receiver's bandwidth is fixed at 1.0 GHz by electrical filters. This allows us to compare different receiver designs effectively based on the pointing error. The LL performance is achievable with certain sets of parameters e.g. $\{r_d = 0.1, m_T =$

$5, N = 3\}$ and$\{r_d = 0.25, m_T = 5, N = 3\}$. The effect of receiver architecture is more prominent for a larger AOI as shown in Figure 5.5(b). For instance, the same receiver architecture ($r_d = 0.1mm, m_T = 5, and\ N = 2$) shows significantly poor BER, $10^{-4.6} \leq BER \leq 10^{-3.5}$ at $\tau = 0.75$. However, the LL performance is still achievable with $\{r_d = 0.25,\ m_T = 3, N = 3\}$ and $\{r_d = 0.25, m_T = 5, N = 3\}$. Consequently, an optimal design parameters set $\{r_d, m_T, N\}$ must be chosen to achieve better link performance over a wide variation of τ in the presence of pointing errors.

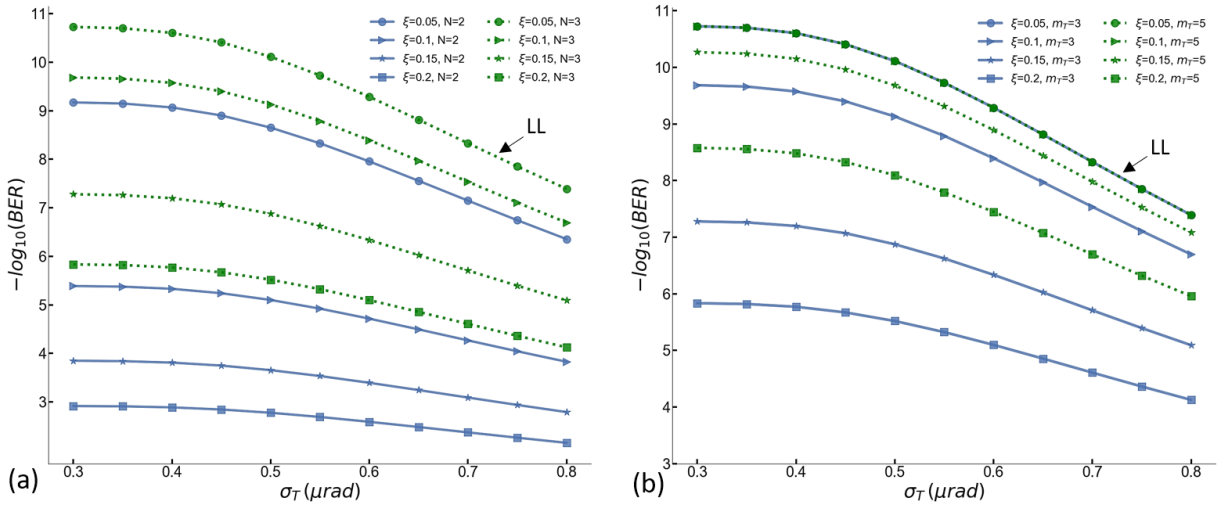

Figure 5.6. Dependence of BER on ξ. a) Effect of different N at $m_T = 3.0$, b) effect of different m_T at $N = 3.0$.

Alongside the parameter selection, an optimum optical design that reduces the optical aberrations is also necessary to improve the performance of the satellite optical links as shown in Figure 5.6. Figure 5.6(a) presents the achievable BER for different aberration factor ξ, $0.05 \leq \xi \leq 0.2$ at $m_T = 3.0$. It can be realized that an optical receiver design with low ξ facilitates stable ISOL even at large τ (e.g. $\tau = 0.75$) in the presence of pointing error. For example, considering the sample receiver architecture as shown in Figure 5.2 that incorporates $m_T = 3.0$ and $N = 2.0$, numerical analysis shows that about 6 orders of magnitude ($\approx 10^6$) BER performance improvement is attainable by lowering ξ from 0.2 to 0.05 at low jitter scenario, $\sigma = 0.3\ \mu rad$. Similarly, in the high pointing jitter scenario, $\sigma = 0.8\ \mu rad$, about 10^4 times BER performance improvement is achievable

by lowering ξ from 0.2 to 0.05 as shown in Figure 5.6(a). Indeed, a low ξ mandates superior optics, complex optical design, higher cost, higher mass, and larger volume. Hence, there is an inevitable trade-offs among size, weight, cost, and performance. The performance can be improved by increasing N of the focusing lens while keeping the beam compression ratio unchanged, $m_T = 3.0$. For example, at $\sigma = 0.8\ \mu rad$ and $\xi = 0.15$, the calculated BER are about 1.6×10^{-3} and 8×10^{-6} for $N = 2.0$ and $N = 3.0$, respectively. Further performance optimization is possible by increasing m_T as shown in Figure 5.6(b). For instance, in the low jitter case ($\sigma = 0.3\ \mu rad$), the achievable BER of a receiver that incorporates $N = 3.0$ and $\xi = 0.2$ can be improved to 2.6×10^{-3} ($\approx 10^{-8.6}$) from 1.5×10^{-6} ($\approx 10^{-5.8}$) by increasing m_T from 3.0 to 5.0. Figure 5.7 presents the performance space of the sample receiver architecture with a given beam compression ratio and F-number of the focusing lens system while assuming a detector radius of 0.1 mm.

The solid curves represent the best-case BER for given m_T and N, whereas the dashed curves present the worst-case performance. Based on the optical design, lens selection, and aberration compensations different BER curves are achievable that depend on jitter amplitude σ. However, the performance will be bounded by the solid and dashed curves as shown in Figure 5.7. One can realize that the receiver's immunity to vibration jitters and angle of incidence by analyzing the performance space. For example, the best case BER of the system that incorporates $m_T = 3.0$ and $N = 2.0$ as shown in Figure 5.7(a) starts rolling off around $\tau = 0.7$ and the worst-case performance fails to establish error-free communication (considering Forward Error Correction, FEC) when $\tau \geq 0.65$. On the contrary, it can be seen from Figure 5.7(d) that if the receiver system is designed with $m_T = 5.0$ and $N = 3.0$, the best case BER and the worst-case BER are immune to the variation of τ and σ up to $\tau \approx 0.9$ and $\tau \approx 0.68$. A similar analysis of the performance roll-off can be done with Figure 5.7(b) and (c). It is evident that $BER_{3-2} < BER_{5-2} < BER_{3-3} < BER_{5-3}$ where BER_{m_T-N} denotes the overall expected communication performance based on BER for given m_T and N in the presence of pointing jitters caused by satellite vibrations. We can notice that a receiver design with a larger N (for a given

m_T) as well as a higher m_T (for a given N) is expected to perform better over a wider AOI in the presence of jitters as can be seen from Figure 5.7. The above-mentioned analyses assume a 100 km communication distance with link parameters given in Table 5.1. An optimum optical receiver can be designed for a given satellite platform and communication requirement by analyzing major design parameters of the architecture as presented in this dissertation.

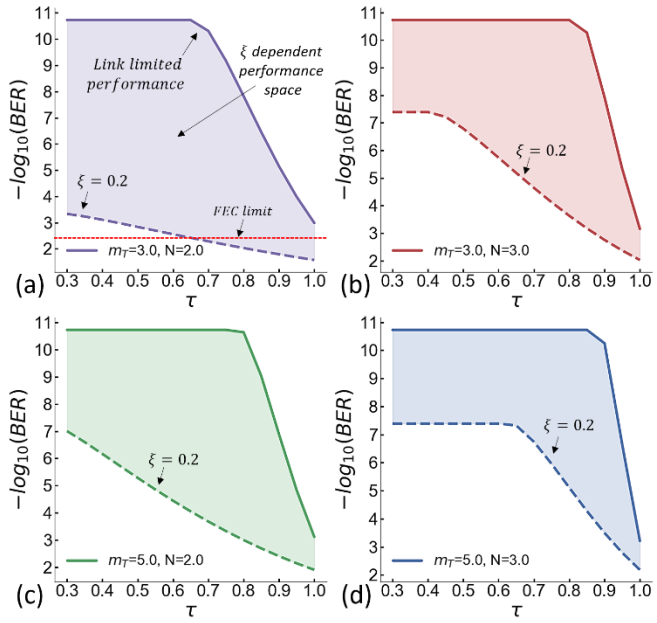

Figure 5.7. Performance limit of the sample receiver architecture with a 0.1 mm detector for given m_T *and* N . a) $m_T =$ 3.0, N=2.0, b) $m_T = 3.0, N = 3.0$, c) $m_T = 5.0, N = 2.0,$ d) $m_T = 5.0, N = 3.0$ [13].

.

In summary, in this chapter, an analytical model to estimate the impact of optical receiver design parameters on the inter-satellite optical link in the presence of angular pointing jitters is presented. As a case study, the effect of receiver design parameters on a direct detection CubeSat receiver is presented here. This study points out that a well-engineered optical receiver can have significant tolerance to random pointing errors that are originated from the satellite vibration and noise in the sensor systems. The analyses carried out here can be the basis for optimum optical receiver design to achieve the best ISOL performance.

Summary and Discussion

In this dissertation, I have addressed the challenges pertinent to inter-satellite communication systems and present a potential omnidirectional communication method. The research focuses on the system level optics integration and design rules to achieve omnidirectional optical communication in the CubeSat platform. In particular, I present transceiver design optimizations for optical communications, collaborative communication strategies between RF and optical for maximum reach, and high-speed CubeSat crosslink implementation based on Wavelength Selective Optical Transceiver (WSOT) design. Besides, I investigate optical design methodologies, housing techniques, component optimizations as well as performance tradeoffs among major COTS optical components (e.g. scanning mirrors, collimators, etc.) to address the optical system design challenges.

In the beginning, a study is presented on the achievable performance of the available wireless technologies (RF, mmWave, and optical) to establish an omnidirectional CubeSat crosslink. Since each technology possesses its distinct advantages and limitations in the CubeSat platform, a comprehensive study of the performance of communication links in terms of design parameters, power consumption, data rate, and modulation formats are studied. This study shows that the incorporation of the required number of large microwave antennas and phased array antennas to achieve omnidirectional communication is tremendously challenging in a resource-limited CubeSat platform. As studied in section 2.3, the current CubeSats are not capable to deliver the required high power to achieve omnidirectionality in static and PAA based microwave systems, the current CubeSats are not capable to deliver the required high power to achieve omnidirectionality in static antenna and PAA based microwave systems. In contrast, the optical communication system demonstrates the potential to achieve omnidirectional multi-Gb/s data communication due to its low total power consumption and the availability of compact (smaller than 15 mm in diameter), high-speed (in the order of kHz) scanning mirrors. Furthermore, the analyses reveal that although the optical communication demonstrates one to two orders of magnitude higher data rate than

microwave system up to a crossover distance, the mmWave point-to-point communication system (e.g. 60 GHz) has the potential to perform better than the optical system (e.g. 194 THz) in considered CubeSat platform. It is shown that there exists a performance crossover between microwave and optical communication links due to the tradeoffs among the system design parameters. The performance crossovers between microwave and optical communication links are analyzed in detail to assess the maximum reach and maximum data rate. The right selection of the communication medium in a CubeSat crosslink depends on the application, the integrable antenna size, the available power, the desired data rate, and the desired communication range.

Then, an omnidirectional CubeSat optical crosslink concept is introduced based on Wavelength Selective Optical Transceiver (WSOT). The WSOT based optical antenna can achieve a 360^o FOR that is capable of one-to-many high-speed data communications. The optical transceiver is designed in Zemax and the performance metrics e.g. receiver sensitivity, transceiver power loss, etc., are experimentally measured in the lab environment. In the worst-case performance scenario, the presented WSOT system possesses better than -65 dB crosstalk and a sensitivity of about - 33 dBm and about -29.5 dBm for 200 MHz and 400 MHz signals, respectively. These metrics indicate that with a 15 mm transceiver aperture size and 1 W peak bit power, the system attains communication distance up to 125 km and 80 km for 400 Mb/s and 800 Mb/s data rates, respectively. Furthermore, through careful optics selection, optical design, and mechanical design, it is ensured that five WSOTs can be assembled inside a 3 U CubeSat to achieve a full field of regard (360^o) to enable omnidirectional high-speed optical communication. Further performance improvements are possible through incorporating advanced amplifiers, error-correction coding, and large aperture optics.

Subsequently, analytical studies related to the scanning mirror-based beam steering system as well as the scanning mirror's smallest step angle requirement to achieve omnidirectional communication is presented in Chapter 4. Besides, I demonstrate the relations and dependencies

among scanning mirror's smallest step angle, laser beam divergence, optics dimensions, communication distance, and scanning area filling efficiency, etc. Moreover, a detailed analysis is presented on the optimization challenges of the transmit laser beam size considering the interplay among beam divergence, beam clipping, and scattering. This chapter also discusses the effect of laser peak power, initial beam size, and communication distance on effective communication beam width to maintain a long-distance (more than 100 km) communication with SNR ≥ 10 dB at a data rate greater than 500 Mb/s. This paper mainly chapter emphasizes transmitter side optimization techniques to enable CubeSat omnidirectional optical crosslink.

Finally, an analytical model to estimate the impact of optical receiver design parameters on the inter-satellite optical link in the presence of angular pointing jitters is presented in Chapter 5. As a case study, the effect of receiver design parameters is studied based on a direct detection CubeSat optical link. The study demonstrates the receiver design techniques that can possess high pointing jitter rejection. Our study points out that a well-engineered optical receiver can have significant tolerance to random pointing errors that are originated from the satellite vibration and noise in the sensor systems.

The analyses carried out in this dissertation can be the basis for optimum optical communication system design to achieve the best omnidirectional ISOL performance. A lot of work needs to be done in the future to exploit the vast possibilities of the CubeSat constellation. Among many open issues, fast seamless LEO to ground optical communicator development, extending the high efficient solid-state lasers development to increase the communication range, faster scanning system development, wide field of view detector design, communication protocol development for optical crosslinks to support a massive number of Cubesats, dynamic formation via intelligent links, etc. are the major areas that need to be investigated. The Cubesat swarm can play a vital role in achieving small, affordable, and transformative approaches to enable remote sensing systems for winds, clouds, topography, photometry, etc. An optical crosslink incorporating small optical

transceivers (e.g. WSOT system) can achieve connectivity among multiple small spacecraft and therefore, enable full-sky coverage without expensive intermediate ground relay stations. CubeSat crosslink enable more automation, constellations could exchange information to maintain precise positions without input from the ground. Seamless data transmission to the ground station is also attainable through relay nodes given that at least one CubeSat is in the field of view of the ground station. A well logically connected small-satellite swarm can perform as an unprecedented massive spaceborne remote sensing system. Small-satellites missions have the potential of delivering substantial science return, at a portion of the cost of larger flagship counterparts. A high-speed omnidirectional optical link will enable data and resource sharing among spacecrafts in the constellation. Furthermore, if smallsats can be configured in clusters or swarms, the technological and science return could equal or eventually surpass the returns of larger ships.

Bibliography

[1] W. J. Blackwell *et al.*, "Overview of the NASA TROPICS CubeSat constellation mission," in *CubeSats and NanoSats for Remote Sensing II*, Sep. 2018, vol. 10769, p. 1076908, doi: 10.1117/12.2320333.

[2] S. Corpino and F. Nichele, "CubeSats to support Mars exploration: Three scenarios for valuable planetary science missions," in *Proceedings of the 12th Reinventing Space Conference*, 2017, pp. 17–32.

[3] J. E. Velazco *et al.*, "Inter-satellite omnidirectional optical communicator for remote sensing," in *CubeSats and NanoSats for Remote Sensing II*, Sep. 2018, vol. 10769, p. 107690L, doi: 10.1117/12.2322367.

[4] J. E. Velazco *et al.*, "High Data Rate Inter-Satellite Omnidirectional Optical Communicator," in *32nd Annual AIAA/USU Conference on Small Satellites*, 2018, pp. SSC18-WKI-02.

[5] S. Bandyopadhyay, R. Foust, G. P. Subramanian, S.-J. Chung, and F. Y. Hadaegh, "Review of Formation Flying and Constellation Missions Using Nanosatellites," *Journal of Spacecraft and Rockets*, vol. 53, no. 3, pp. 567–578, Mar. 2016, doi: 10.2514/1.A33291.

[6] K. Devaraj *et al.*, "Planet High Speed Radio: Crossing Gbps from a 3U CubeSat," *Small Satellite Conference*, Aug. 2019, [Online]. Available: https://digitalcommons.usu.edu/smallsat/2019/all2019/106.

[7] K. Leveque, L. Carleton, J. King, Z. Cuseo, and R. Babb, "Unlocking the Next Generation of Nano-Satellite Missions with 320 Mbps Ka-Band Downlink: On-Orbit Results," *Small Satellite Conference*, Aug. 2019, [Online]. Available: https://digitalcommons.usu.edu/smallsat/2019/all2019/110.

[8] N. Saeed, A. Elzanaty, H. Almorad, H. Dahrouj, T. Y. Al-Naffouri, and M.-S. Alouini, "CubeSat Communications: Recent Advances and Future Challenges," *IEEE Communications Surveys Tutorials*, vol. 22, no. 3, pp. 1839–1862, thirdquarter 2020, doi: 10.1109/COMST.2020.2990499.

[9] K. Devaraj *et al.*, "Dove High Speed Downlink System," p. 9.

[10] Farzana I.Khatri, Bryan S.Robinson, Marilyn D.Semprucci, and Don M.Boroson, "Lunar Laser Communication Demonstration operationsarchitecture," *Acta Astronautica*, vol. 111, pp. 77–83, Jul. 2015.

[11] Ryan W Kingsbury, "Optical communications for small satellites," Massachusetts Institute of Technology, 2015.

[12] Rachel Morgan and Kerri Cahoy, "Nanosatellite Lasercom System," presented at the 31st Annual AIAA/USU Conference on Small Satellites, 2017.

[13] I. U. Zaman and O. Boyraz, "Impact of receiver architecture on small satellite optical link in the presence of pointing jitter," *Appl. Opt., AO*, vol. 59, no. 32, pp. 10177–10184, Nov. 2020, doi: 10.1364/AO.409144.

[14] P. Grenfell, A. Aguilar, K. Cahoy, and M. Long, "Pointing, Acquisition, and Tracking for Small Satellite Laser Communications," p. 7.

[15] C.-C. Chen and C. S. Gardner, "Impact of random pointing and tracking errors on the design of coherent and incoherent optical intersatellite communication links," *IEEE Transactions on Communications*, vol. 37, no. 3, pp. 252–260, Mar. 1989, doi: 10.1109/26.20099.

[16] Blue Canyon Technologies, *Components*. https://www.bluecanyontech.com/components.

[17] J. Chang, C. M. Schieler, K. M. Riesing, J. W. Burnside, K. Aquino, and B. S. Robinson, "Body pointing,

acquisition and tracking for small satellite laser communication," in *Free-Space Laser Communications XXXI*, Mar. 2019, vol. 10910, p. 109100P, doi: 10.1117/12.2511159.

[18] I. U. Zaman, J. E. Velazco, and O. Boyraz, "Omnidirectional Optical Crosslinks for CubeSats: Transmitter Optimization," *IEEE Transactions on Aerospace and Electronic Systems*, pp. 1–1, 2020, doi: 10.1109/TAES.2020.2995320.

[19] J. Ma, X. Li, S. Yu, L. Tan, and Q. Han, "Influence of satellite vibration on optical communication performance for intersatellite laser links," *OPT REV*, vol. 19, no. 1, pp. 25–28, Jan. 2012, doi: 10.1007/s10043-012-0004-z.

[20] M. E. Wittig, L. van Holtz, D. E. L. Tunbridge, and H. C. Vermeulen, "In-orbit measurements of microaccelerations of ESA's communication satellite Olympus," in *Free-Space Laser Communication Technologies II*, Jul. 1990, vol. 1218, pp. 205–214, doi: 10.1117/12.18234.

[21] F. Sansone *et al.*, "LaserCube optical communication terminal for nano and micro satellites," *Acta Astronautica*, vol. 173, pp. 310–319, Aug. 2020, doi: 10.1016/j.actaastro.2020.04.049.

[22] J. D. Barry and G. S. Mecherle, "Beam pointing error as a significant design parameter for satellite-borne, free-space optical communication systems," *OE*, vol. 24, no. 6, p. 241049, Dec. 1985, doi: 10.1117/12.7973628.

[23] S. Arnon, S. R. Rotman, and N. S. Kopeika, "Performance limitations of free-space optical communication satellite networks due to vibrations: direct-detection digital mode," in *10th Meeting on Optical Engineering in Israel*, Sep. 1997, vol. 3110, pp. 357–368, doi: 10.1117/12.281392.

[24] A. Shlomi and N. S. Kopeika, "Performance limitations of free-space optical communication satellite networks due to vibrations-analog case," *OE*, vol. 36, no. 1, pp. 175–182, Jan. 1997, doi: 10.1117/1.601156.

[25] T. Song, Q. Wang, M.-W. Wu, T. Ohtsuki, M. Gurusamy, and P.-Y. Kam, "Impact of Pointing Errors on the Error Performance of Intersatellite Laser Communications," *J. Lightwave Technol., JLT*, vol. 35, no. 14, pp. 3082–3091, Jul. 2017.

[26] D. M. Boroson *et al.*, "Overview and results of the Lunar Laser Communication Demonstration," in *Free-Space Laser Communication and Atmospheric Propagation XXVI*, Mar. 2014, vol. 8971, p. 89710S, doi: 10.1117/12.2045508.

[27] A. Carrasco-Casado *et al.*, "LEO-to-ground optical communications using SOTA (Small Optical TrAnsponder) – Payload verification results and experiments on space quantum communications," *Acta Astronautica*, vol. 139, pp. 377–384, Oct. 2017, doi: 10.1016/j.actaastro.2017.07.030.

[28] C. Fuchs and C. Schmidt, "Update on DLR's OSIRIS program," in *International Conference on Space Optics — ICSO 2018*, Jul. 2019, vol. 11180, p. 111800I, doi: 10.1117/12.2535937.

[29] T. S. Rose *et al.*, "Optical communications downlink from a 1.5U Cubesat: OCSD program," in *International Conference on Space Optics — ICSO 2018*, Jul. 2019, vol. 11180, p. 111800J, doi: 10.1117/12.2535938.

[30] J. E. Kaufmann and V. W. S. Chan, "Coherent optical intersatellite crosslink systems," in *MILCOM 88, 21st Century Military Communications - What's Possible?'. Conference record. Military Communications Conference*, Oct. 1988, pp. 533–540 vol.2, doi: 10.1109/MILCOM.1988.13443.

[31] T. Tanaka, Y. Kawamura, and T. Tanaka, "Development and operations of nano-satellite FITSAT-1 (NIWAKA)," *Acta Astronautica*, vol. 107, pp. 112–129, Feb. 2015, doi: 10.1016/j.actaastro.2014.10.023.

[32] T. S. Rose *et al.*, "Optical communications downlink from a 1.5U Cubesat: OCSD program," in *International Conference on Space Optics — ICSO 2018*, Jul. 2019, vol. 11180, p. 111800J, doi:

10.1117/12.2535938.

[33] Siegfried W Janson, “Cubesat-scale laser communications.”

[34] K. Cahoy *et al.*, “The CubeSat Laser Infrared CrosslinK Mission (CLICK),” in *International Conference on Space Optics — ICSO 2018*, Jul. 2019, vol. 11180, p. 111800Y, doi: 10.1117/12.2535953.

[35] H. T. Friis, “A Note on a Simple Transmission Formula,” *Proceedings of the IRE*, vol. 34, no. 5, pp. 254–256, May 1946, doi: 10.1109/JRPROC.1946.234568.

[36] D. Roddy, *Satellite Communications*, Fourth. McGraw-Hill, 2006.

[37] V. W. S. Chan, “Optical satellite networks,” *Journal of Lightwave Technology*, vol. 21, no. 11, pp. 2811–2827, Nov. 2003, doi: 10.1109/JLT.2003.819534.

[38] H. Kaushal, V. Jain, and S. Kar, “Acquisition, Tracking, and Pointing,” 2017, pp. 119–137.

[39] Y. Kim *et al.*, “Feasibility of Mobile Cellular Communications at Millimeter Wave Frequency,” *IEEE Journal of Selected Topics in Signal Processing*, vol. 10, no. 3, pp. 589–599, Apr. 2016, doi: 10.1109/JSTSP.2016.2520901.

[40] M. Jiang, Z. N. Chen, Y. Zhang, W. Hong, and X. Xuan, “Metamaterial-Based Thin Planar Lens Antenna for Spatial Beamforming and Multibeam Massive MIMO,” *IEEE Transactions on Antennas and Propagation*, vol. 65, no. 2, pp. 464–472, Feb. 2017, doi: 10.1109/TAP.2016.2631589.

[41] J. D. Dunworth *et al.*, “A 28GHz Bulk-CMOS dual-polarization phased-array transceiver with 24 channels for 5G user and basestation equipment,” *2018 IEEE International Solid - State Circuits Conference - (ISSCC)*, pp. 70–72, 2018, doi: 10.1109/isscc.2018.8310188.

[42] B. Sadhu *et al.*, “7.2 A 28GHz 32-element phased-array transceiver IC with concurrent dual polarized beams and 1.4 degree beam-steering resolution for 5G communication,” in *2017 IEEE International Solid-State Circuits Conference (ISSCC)*, Feb. 2017, pp. 128–129, doi: 10.1109/ISSCC.2017.7870294.

[43] Optotune, “Dual axis VCM with position feedback2D Beam Steering.” https://www.optotune.com/contact/49-products/beam-steering.

[44] I. U. Zaman, A. W. Janzen, R. Torun, M. Peng, J. E. Velazco, and O. Boyraz, “Omnidirectional optical transceiver design techniques for multi-frequency full duplex CubeSat data communication,” 10769-42, Aug. 2018.

[45] “eHaWK 27A-84V,” *MMA Design LLC*. https://mmadesignllc.com/product/ehawk-27a-84v/ (accessed Dec. 06, 2020).

[46] B. Yang, Z. Yu, J. Lan, R. Zhang, J. Zhou, and W. Hong, “Digital Beamforming-Based Massive MIMO Transceiver for 5G Millimeter-Wave Communications,” *IEEE Transactions on Microwave Theory and Techniques*, vol. 66, no. 7, pp. 3403–3418, Jul. 2018, doi: 10.1109/TMTT.2018.2829702.

[47] I. U. Zaman, A. W. Janzen, R. Torun, J. E. Velazco, O. Boyraz, and Ozdal Boyraz, “Design Tradeoffs and Challenges of Omnidirectional Optical Antenna for High Speed, Long Range Inter CubeSat Data Communication,” SSC18-WKII-06, Aug. 2018.

[48] M. Toyoshima, “Trends in satellite communications and the role of optical free-space communications [Invited],” *J. Opt. Netw., JON*, vol. 4, no. 6, pp. 300–311, Jun. 2005, doi: 10.1364/JON.4.000300.

[49] S. K. Podilchak *et al.*, “Compact antenna for microsatellite using folded shorted patches and an integrated feeding network,” in *2012 6th European Conference on Antennas and Propagation (EUCAP)*, Mar. 2012, pp. 1819–1823, doi: 10.1109/EuCAP.2012.6206272.

[50] International Telecommunication Union (ITU), “G.975 : Forward error correction for submarine systems.” Oct. 01, 2000.

[51] International Telecommunication Union (ITU), “G.709.2 : OTU4 long-reach interface.” Jul. 22, 2018.

[52] A. Goldsmith, *Wireless Communications*, 1st ed. Cambridge University Press, 2005.

[53] T. Y. Elganimi, “Performance Comparison between OOK, PPM and PAM Modulation Schemes for Free Space Optical (FSO) Communication Systems: Analytical Study,” 2013, doi: 10.5120/13786-1838.

[54] I. U. Zaman, J. E. Velazco, and O. Boyraz, “Realization of Omnidirectional CubeSat Crosslink by Wavelength Selective Optical Transceiver,” *IEEE Journal on Miniaturization for Air and Space Systems*, pp. 1–1, 2020, doi: 10.1109/JMASS.2020.2995316.

[55] Govind P. Agrawal, “Fiber-Optic Communication Systems,” 3rd ed., New York, NY: John Wiley & Sons, Inc, pp. 162–167.

[56] M. Technologies, “Mirrorcle Technologies MEMS Mirrors - Technical Overview,” 2017. https://www.semanticscholar.org/paper/Mirrorcle-Technologies-MEMS-Mirrors-%E2%80%93-Technical/d131a1576787ffa47fbd035881ec3780cf1a09b4.

[57] L. Broman, “Non-Imaging Solar Concentrators With Flat Mirrors,” in *Intl Conf on Nonimaging Concentrators*, Jan. 1984, vol. 0441, pp. 102–110, doi: 10.1117/12.937707.

[58] H. Ries and A. Rabl, “Edge-ray principle of nonimaging optics,” *J. Opt. Soc. Am. A, JOSAA*, vol. 11, no. 10, pp. 2627–2632, Oct. 1994, doi: 10.1364/JOSAA.11.002627.

[59] J. C. Miñano and J. C. González, “New method of design of nonimaging concentrators,” *Appl Opt*, vol. 31, no. 16, pp. 3051–3060, Jun. 1992.

[60] R. W. Kingsbury, “Optical communications for small satellites,” Thesis, Massachusetts Institute of Technology, 2015.

[61] M. Abdelrahman and S.-Y. Park, “Spacecraft attitude control via a combined State-Dependent Riccati Equation and adaptive neuro-fuzzy approach,” *Aerospace Science and Technology*, vol. 26, pp. 16–28, Apr. 2013, doi: 10.1016/j.ast.2012.02.010.

[62] H. Kaushal and G. Kaddoum, “Optical Communication in Space: Challenges and Mitigation Techniques,” *IEEE Communications Surveys Tutorials*, vol. 19, no. 1, pp. 57–96, Firstquarter 2017, doi: 10.1109/COMST.2016.2603518.

[63] Micro Laser System Inc., “Adjustable Fiber Collimators.” http://www.microlaser.com/FiberOptic/FiberCollimators.html.

[64] Thorlabs, “Collimation / Coupling.” https://www.thorlabs.com/navigation.cfm?guide_id=27.

[65] Princetel, “FIBER COMPONENTS: Large-beam fiber collimators.” http://www.princetel.com/fc_clx.asp.

[66] R. W. Kingsbury, “Optical communications for small satellites,” Thesis, Massachusetts Institute of Technology, 2015.

[67] A. S. Mayer, C. R. Phillips, and U. Keller, “Watt-level 10-gigahertz solid-state laser enabled by self-defocusing nonlinearities in an aperiodically poled crystal,” *Nature Communications*, vol. 8, no. 1, pp. 1–8, Nov. 2017, doi: 10.1038/s41467-017-01999-y.

[68] F. R. Ahmad and F. Rana, “Passively Mode-Locked High-Power (210 mW) Semiconductor Lasers at 1.55-µm Wavelength,” *IEEE Photonics Technology Letters*, vol. 20, no. 3, pp. 190–192, Feb. 2008, doi: 10.1109/LPT.2007.913254.

[69] Anthony E. Siegman, in *LASERS*, Sausalito, California: University Science Books, pp. 665–672.

[70] R. D. Guenther, in *Modern Optics*, John Wiley & Sons, Inc, 1990, pp. 335–340.

[71] H. TAKENAKA, “Link budget analysis for small optical transponder onboard small satellites,” *Co61st International Astronautical Congress, Praguemmunication, 2010. Koetzting, Germany, May 16-20*, pp. 1–8, 2011.

[72] V. W. S. Chan, “Optical satellite networks,” *J. Lightwave Technol.*, vol. 21, no. 11, pp. 2811–2827, Nov. 2003, doi: 10.1109/JLT.2003.819534.

[73] Y. Ding, D. I. Nikitichev, I. Krestnikov, D. Livshits, M. A. Cataluna, and E. U. Rafailov, “Quantum-dot external-cavity passively modelocked laser with high peak power and pulse energy,” *Electronics Letters*, vol. 46, no. 22, pp. 1516–1518, Oct. 2010, doi: 10.1049/el.2010.2336.

[74] S. G. Lambert and W. L. Casey, *Laser communications in space*. Boston: Artech House, 1995.

[75] S. Arnon, S. Rotman, and N. S. Kopeika, “Beam width and transmitter power adaptive to tracking system performance for free-space optical communication,” *Appl. Opt., AO*, vol. 36, no. 24, pp. 6095–6101, Aug. 1997, doi: 10.1364/AO.36.006095.

[76] M. Scheinfeild, N. S. Kopeika, and R. Melamed, “Acquisition system for microsatellites laser communication in space,” in *Free-Space Laser Communication Technologies XII*, May 2000, vol. 3932, pp. 166–175, doi: 10.1117/12.384308.

[77] M. Guelman, A. Kogan, A. Kazarian, A. Livne, M. Orenstein, and H. Michalik, “Acquisition and pointing control for inter-satellite laser communications,” *IEEE Transactions on Aerospace and Electronic Systems*, vol. 40, no. 4, pp. 1239–1248, Oct. 2004, doi: 10.1109/TAES.2004.1386877.

[78] HAMAMATSU, “Characteristics and use of infrared detectors.” Nov. 2004, [Online]. Available: https://mmrc.caltech.edu/FTIR/Literature/General/Hamamatus%20IR%20dectors.pdf.

[79] Thorlabs, “Photodiodes,” *Photodiodes*, 2020. https://www.thorlabs.com/newgrouppage9.cfm?objectgroup_id=285 (accessed Oct. 03, 2020).

[80] Thorlabs, “InGaAs Avalanche PhotodetectorsPhotodiodes,” *Photodiodes*, 2020. https://www.thorlabs.com/newgrouppage9.cfm?objectgroup_id=4047 (accessed Oct. 03, 2020).